Lehrstuhl für Elektrische Antriebssysteme und Leistungselektronik
der Technischen Universität München

Sensorless Control of Permanent Magnet Synchronous Machines With Multiple Saliencies

Zhe Chen

Vollständiger Abdruck der von der Fakultät für Elektrotechnik und Informationstechnik der Technischen Universität München zur Erlangung des akademischen Grades eines

Doktor-Ingenieurs

genehmigten Dissertation.

Vorsitzender: Univ.-Prof. Dr.-Ing. Wolfgang Kellerer
Prüfer der Dissertation:
1. Univ.-Prof. Dr.-Ing. Ralph Kennel
2. Prof. Silverio Bolognani
(Universität Padua, Italien)

Die Dissertation wurde am 21.12.2015 bei der Technischen Universität München eingereicht und durch die Fakultät für Elektrotechnik und Informationstechnik am 17.09.2016 angenommen.

Acknowledgment

I would like to thank Prof. Dr.-Ing. Ralph Kennel for accepting me as a PhD candidate at the Institute for Electrical Drive Systems and Power Electronics at Technische Universität München in 2011, otherwise this dissertation would not come true. He gave me the freedom to choose the doctoral topic in the beginning of my study and encouraged me when I faced problems. I really appreciate his support throughout my doctoral period.
Furthermore, I'd like to thank Prof. Silverio Bolognani (University of Padova, Italy) for agreeing to be the co-examiner of my dissertation and his valuable suggestions for improving the quality of my dissertation.
It is my great pleasure to work with the colleagues at EAL. They gave me support in both my academic research and daily life in Germany. First of all, I feel grateful to Dr. Jianbo Gao for his guidance and generous help in the beginning, when I was not sure about my research topic and did not have my own testbench. Without his help, it would have lasted longer to finish this work. I'd like to express my gratitude to Dr.-Ing. Peter Stolze and Dr.-Ing. Esteban Fuentes for their support when I was setting up my testbench. Dr.-Ing. Fengxiang Wang, Mr. Zhenbin Zhang and Dr.-Ing. Zhixun Ma are my cooperative partners and we have published 6 IEEE transaction papers together. Many thanks to Dr.-Ing. Peter Landsmann and Dr.-Ing. Dirk Paulus, they gave me valuable suggestions to improve the creativity of my work. Mr. Darshan Manoharan, Mr. Guangye Si, Mr. Ali EI-Hafni, Mr. Felix Rojas, and Mr. Reza Fotouhi are very good friends of mine, with whom I shared many memorable times. You make my life in Munich amazing.
I appreciate Mr. Dietmar Schuster and Mr. Shubin Ruan for their work that improved my experimental testbench. Many thanks to Mr. Julien Cordier , Mrs. Julia Menz and Mr. Wolfgang Ebert for their coordination help.
Thanks my wife, Yufang Liu, for her understanding and love. In the near future, we will have our first child, which makes me feel wonderful. Thanks to all my family for their support.

Munich, in November 2015
Zhe Chen

Abstract

This work aims to solve the sensorless control problems of PMSM with multiple saliencies e.g., concentrated winding PMSM (cwSPMSM). The main contributions are as follows. The multiple-saliency model of the cwSPMSM is built based on experimental results. The physical reason for causing the secondary saliency signal is explained as well. Three saliency tracking based sensorless control methods i.e., Multi-Signal Injection method, Secondary Saliency Tracking method and Repetitive Control method are proposed for sensorless control of cwSPMSM in the low speed range and at standstill. As a necessary supplement to the saliency tracking based sensorless method, three fundamental model based sensorless control methods, Model Reference Adaptive System, Sliding Mode Observer and Extended Kalman Filter, are comparatively studied for higher speed operation. Any one of them can be combined with one of the saliency tracking based methods to formulate a hybrid scheme. The multi-parameter identification is discussed to demonstrate how to improve the system robustness. Three improvements for the existing test bench, SVPWM design, Resolver demodulation design and C/VHDL code generation, are developed to further enhance the performance of the controller.

Contents

1 Introduction **1**
1.1 Contributions . . . 3
1.2 Related work . . . 4
1.3 Outline . . . 6

2 State of the art **7**
2.1 Introduction . . . 7
2.2 Saliency tracking based sensorless method . . . 7
2.2.1 Carrier-signal based saliency tracking method . . . 8
2.2.1.1 Rotating HF signal injection method . . . 8
2.2.1.2 Zero-sequence voltage or current based method . . . 8
2.2.1.3 Pulsating HF signal injection method . . . 9
2.2.2 PWM switching pattern based method . . . 10
2.2.2.1 INFORM and its related method . . . 10
2.2.2.2 Fundamental PWM-integrated method . . . 12
2.3 Fundamental model based sensorless method . . . 13
2.3.1 Active flux observer . . . 13
2.3.2 Model reference adaptive system . . . 14
2.3.3 State-space based observer . . . 15
2.3.3.1 Luenberger observer . . . 16
2.3.3.2 Extended Kalman filter . . . 16
2.3.3.3 Sliding mode observer . . . 18
2.4 Parameter identification of PMSM . . . 18
2.4.1 HF signal injection based off-line parameter identification . . . 18
2.4.2 Fundamental model based parameter identification . . . 19
2.4.3 Observer based on-line parameter identification . . . 20
2.4.3.1 EKF based parameter identification . . . 21
2.4.3.2 MRAS based parameter identification . . . 21
2.5 Summary . . . 21

3 Machine model and saliency model **23**
3.1 Symbol definition and nomenclature . . . 23
3.1.1 Symbol explanation . . . 23
3.1.2 Reference frame . . . 25
3.1.3 Space vector representation . . . 25
3.2 Machine fundamental model . . . 29
3.2.1 Assistant matrix introduction . . . 29
3.2.2 Machine fundamental model in $\alpha - \beta$ frame . . . 29
3.2.3 Machine fundamental model in $d - q$ frame . . . 31
3.3 Multiple-saliency model . . . 32
3.3.1 Primary saliency model . . . 32
3.3.2 Multiple-saliency model . . . 33
3.3.3 Other considerations . . . 35
3.3.3.1 Resistance impact . . . 36
3.3.3.2 Cross-saturation and secondary saliency impact . . . 36
3.4 Summary . . . 37

4 Testbench and implementation **39**
4.1 Testbench introduction . . . 39
4.2 Space vector PWM implementation . . . 41
4.3 Resolver demodulation . . . 43
4.4 C code generation through Matlab/Simulink . . . 44
4.5 VHDL code generation through Matlab/Simulink . . . 47
4.6 Summary . . . 49

5 Saliency tracking based sensorless method **51**
5.1 Background . . . 51
5.1.1 Sensorless control based on the HF signal injection . . . 51
5.1.2 Saliency behavior of the tested cwSPMSM . . . 52
5.1.3 Challenges of strong multiple saliencies . . . 53
5.1.4 The analysis of multiple saliencies . . . 54
5.1.4.1 Stator background . . . 54
5.1.4.2 Zigzag leakage flux . . . 55
5.1.4.3 Impact of slot/pole combination . . . 56
5.2 Multi-signal injection method . . . 57
5.2.1 Derivation of the proposed MSI method . . . 57
5.2.1.1 Precise multiple saliencies model . . . 57
5.2.1.2 Principle of MSI method . . . 58
5.2.1.3 Remarks of MSI method . . . 59
5.2.1.4 Other related issues . . . 60
5.2.2 Behavior of the frequency-dependent saliencies . . . 61
5.2.3 Application of MSI Method . . . 62
5.2.4 Implementation and experiment results . . . 62
5.2.4.1 Combination parameters . . . 62
5.2.4.2 Flux angle estimation . . . 63

5.2.4.3 Sensorless experimental results . . . 64
5.2.5 Conclusion . . . 68
5.3 Secondary saliency tracking method . . . 69
5.3.1 Secondary saliency tracking method . . . 69
5.3.1.1 Selection principle of saliency signals . . . 69
5.3.1.2 Secondary saliency tracking . . . 70
5.3.1.3 Band pass filter design . . . 71
5.3.1.4 Initial position estimation . . . 71
5.3.2 Experimental results . . . 72
5.3.3 Conclusion . . . 77
5.4 Repetitive control method . . . 78
5.4.1 Repetitive control in time domain . . . 78
5.4.2 The design of RC in angle domain . . . 79
5.4.3 Implementation and experimental results . . . 82
5.4.3.1 Application of the proposed RC . . . 82
5.4.3.2 Experimental results . . . 83
5.4.4 Conclusion . . . 84
5.5 Summary . . . 84

6 Fundamental model based sensorless method 85
6.1 Model reference adaptive system . . . 85
6.2 Sliding mode observer . . . 87
6.3 Extended Kalman filter . . . 88
6.4 Theoretical comparison of MRAS, SMO and EKF . . . 90
6.5 Experimental comparison . . . 90
6.5.1 Estimation accuracy and limitation . . . 90
6.5.2 Parameter dependence and comparison overview . . . 93
6.6 Hybrid sensorless control . . . 93
6.7 Summary . . . 94

7 Multi-parameter identification 95
7.1 Introduction . . . 95
7.2 System description . . . 97
7.3 Parameter estimation . . . 97
7.3.1 Identifiability . . . 98
7.3.2 Parameter estimation based on MRAS . . . 99
7.3.3 Parameter estimation based on EKF . . . 100
7.3.3.1 Resistance and inductance estimation . . . 100
7.3.3.2 Resistance and PM flux estimation . . . 101
7.3.3.3 Inductance and PM flux estimation . . . 101
7.3.4 Theoretical comparison of MRAS and EKF . . . 101
7.4 Inverter nonlinearity . . . 102
7.5 Experimental results . . . 104
7.5.1 Sensorless control with resistance and PM flux estimation . . . 104
7.5.2 Sensorless control with inductance and PM flux estimation . . . 107

7.5.3 Experimental comparison of MRAS and EKF 107
7.6 Summary 108

8 Conclusion **111**

A List of publications **113**
A.1 Journal papers 113
A.2 Conference papers 113

B Abbreviations **115**

C Testbench data **117**

D Derivation of the MSI method and filter design **121**
D.1 Mathematical derivation 121
D.2 Filter Design 122

List of Figures **123**

List of Tables **127**

Bibliography **129**

CHAPTER 1

Introduction

Nowadays, electrical machines that transfer energy bidirectionally between electrical power domain and mechanical power domain are playing an important role in our daily life. They exist everywhere around us e.g., in air-condition, computer, automotive, locomotive etc.. Moreover, they are especially important in industry and power generation.

In terms of the operation mechanism, electrical machines can be classified into two categories: Direct Current (DC) machines and Alternating Current (AC) machines, which includes Induction Machines (IM) and Synchronous Machines (SM). To be more specific, SM, which has more promising application prospect compared to IM from the power density and efficiency point of view, can be further divided into several subcategories: Permanent Magnet Synchronous Machines (PMSM), Synchronous Reluctance Machines (SynRM), Switched Reluctance Machines (SRM), and Brushless DC Machines (BLDCM). Among these SMs, PMSM has been widely applied in electrical drive systems because of its high performance, which can be explained in three aspects. Firstly, permanent magnet material can establish a high density and stable permanent flux, which is the unique intermediary of energy transmission between the stator and rotor of a PMSM. The PMSM, therefore, has a smaller size but a higher power-to-volume(weight)-ratio compared to its counterpart, the AM. Secondly, different rotor design techniques result in Surface-mounted-type (SPMSM) and Interior-type (IPMSM), which are fit for low-power higher-precision servo applications and wider constant-power-region/ weakening-flux-capability drive applications, respectively. The flexibility of its structure makes the PMSM able to fulfill requirements of different application areas. Thirdly, thanks to advanced control schemes like Field Oriented Control (FOC), Direct Torque Control (DTC), and Predictive Torque Control (PTC), they allow PMSMs to have more smooth torque performance in both dynamic and steady state than other SMs.

Among SPMSMs, the concentrated windings PMSMs (cwSPMSM) are gaining more and more attention owing to their lower production cost, higher feasibility and more compact designs when compared to machines with distributed windings. For example, in electric and hybrid vehicles, concentrated windings are adopted to realize shorter motor length and higher

efficiency. It is therefore foreseen that this machine type will find more and more applications in the future. The cwSPMSM is the research object of this dissertation.

A high performance control method like FOC can not only improve the adaptation of PMSMs for various applications but also increase the system efficiency by adopting additional control constrains (e.g., Maximum Torque Per Ampere (MTPA)). In an FOC system, the rotor position needs to be measured by an encoder or a resolver mounted with the rotor shaft, because it is required by the Park Transformation that is the kernel of FOC. The encoder or resolver, therefore, is important for the system and its stability and fault-tolerance should be taken into consideration by the designer. It is obvious that there are three weaknesses for the encoder/resolver-based control system:

1) The encoder/resolver and its accessories (cables and decoder circuit) cost extra money.

2) Additional space is needed for the encoder installation. Sometimes, the concern for space and weight is of higher priority in such applications like aerospace and aviation.

3) The reliability problem of the encoder/resolver stimulates a chain reaction and deteriorates the performance of the whole control system.

Fortunately, a drive system without an encoder/resolver has been extensively investigated for almost 25 years. This concept has different expressions in literature such as encoderless, sensorless, or self-sensing. In this work, sensorless is adopted as the terminology for a drive system without the position/speed sensor despite of its ambiguous definition.

Obviously, sensorless control can make the PMSM drive system more competitive. So far, we can find two categories for implementing sensorless control of PMSM in literature: the fundamental model based method and the saliency tracking based method (In most cases, High Frequency (HF) signal injection is required). In general, both methods are equally applicable to other AC machines as well. At low speed ranges (below 0.05p.u.) and standstill, the estimations of position and speed of any PMSM can only be done by saliency tracking based methods, while all model based sensorless methods are invalid due to the disappearance back-Electromotive Force (EMF) signal or poor Signal-to-Noise-Ratio (SNR). The reason is that the saliency is the asymmetrical distribution of rotor flux, which is the physical characteristic of a machine itself and insensitive to the machine model. When a PMSM runs at medium or rated speed, the saliency tracking based method, however, results in an inaccurate estimation, because the back-EMF is no longer negligible in this case. On the contrary, the higher the speed goes, the better the fundamental model based method works, because this method is exactly back EMF dependent. The combination of these two methods or so-called hybrid sensorless control is necessary for the whole speed range operation of the PMSM.

Although comprehensive research topics involved in sensorless controlled PMSM drives have been studied so far, the extensive applications of sensorless controlled cwSPMSM drives in industry have not come true. This is because the cwSPMSM has two significant characteristics that bring great challenges to the researchers of sensorless control. Firstly, because of the homogeneous distribution of its rotor permanent magnet flux, the machine has very weak inductive saliency, on which most sensorless control technologies are based, especially for low and zero speed operation. Secondly, evoked by their special winding structures, the machine shows strong multiple saliencies, which causes strong torque ripples if traditional sensorless control

technologies are still used. Due to these problems, especially the latter one, sensorless control has not been successfully realized yet in practical applications for commercial cwSPMSM. To be more specific, the difficulties impeding the application of sensorless control for such machine types are summarized as below

1) The saliency has different harmonics that arise from the machine design principle or change of operation points. These harmonics are usually decoupled or removed from estimation loop, which is effective when their magnitudes are weak. The stronger the harmonic magnitudes are, the more difficult it is to decouple them.

2) Initial position information is required for starting a PMSM at standstill but its estimation still faces challenges due to the multiple saliencies.

3) In higher speed range applications, the fundamental model based method is preferred. It has several types and their evaluation and in-depth comparison need to be addressed.

4) Most fundamental model based methods are machine parameters-dependent. Thus, on-line or off-line parameter identification become necessary.

1.1 Contributions

This dissertation deals with the analysis and development of sensorless control methods for PMSM with strong multiple saliencies (cwSPMSM). In order to simplify the explanation of different saliencies in advance, they are classified into two types in terms of their physical origin periods: primary saliency and secondary saliency. To be more specific, the asymmetrical rotor permanent magnet flux distribution (saliency between rotor d and q axis), whose period is half of an electrical period, is called the primary saliency. The higher order harmonics of rotor flux distribution are all called secondary saliencies.

In this work, firstly, the multiple-saliency model of cwSPMSM is built based on existing research conclusions from literature as well as massive experiments in the lab. The saliency model is the foundation of a saliency tacking based sensorless control method and its accuracy affects overall performance of the whole system. Then, the physical origin of cwSPMSM's secondary saliency and its relation to frequency of injected voltage signals are theoretically and experimentally analyzed, which gives deep insight into sensorless-capability and machine design principle.

Secondly, three saliency tracking based sensorless methods are proposed from different perspectives to solve the low speed and standstill sensorless control problems of cwSPMSM. A multi-signal injection method, which is developed on the basis of a combination of different saliencies, is proposed. In this method, two separate HF signals with different magnitudes and frequencies are injected into the cwSPMSM at the same time. Their HF current responses, which contain the same rotor position information but different content of saliencies, are demodulated and then combined together to get a clear primary saliency signal. This synthesized signal is then utilized to identify the rotor position afterward. On the contrary to the multi-signal injection method, a secondary saliency tracking method based on primary saliency signal decoupling is proposed as well. Instead of processing the primary saliency signal in most cases, secondary saliency signal that has a better signal to noise ratio and more precise resolution is

processed by a specially designed band pass filter and an adaptive notch filter for speed and rotor position estimation. As a supplementary to the decoupling method, a repetitive control method in an angle domain is adopted. This repetitive control originating from traditional internal mode theory can periodically update its memory and effectively decouple the unwanted saliency signal.

Thirdly, to implement sensorless control of the cwSPMSM at medium and high speeds, three revised fundamental model based methods, Model Reference Adaptive System, Sliding Mode Observer and Extended Kalman Filter, are comparatively investigated and applied. Their advantages as well as disadvantages are summarized. These fundamental model based methods, however, are machine parameters-dependent (e.g., permanent magnet flux, stator resistance and inductance). Hence, the parameter identification is expected to further improve the system robustness. Among the selected sensorless model based methods, Model Reference Adaptive System and Extended Kalman Filter are capable of not only the rotor position and speed estimation but also the on-line machine parameter estimation by means of different selections of state-space variables. The corresponding problems regarding parameter estimation such as parameter identifiability and inverter non-linearity are studied as well.

The experiments of all sensorless methods are performed on a self-made testbench, which consists of a CPU (Core 2 Duo) and an FPGA (Cyclone 3). Although the main hardware of the system and basic software for machine control have already been developed by other colleagues, three aspects have been further improved for the existing system. A resolver demodulation circuit and its control software in the FPGA based on VHDL are developed to decode the position and speed signal measured by a resolver. Then, a space vector Pulse-Width-Modulator (PWM) technique is implemented inside the FPGA, which releases the calculation burden of the CPU and shows the advantage of the FPGA's parallel operation. At last, a C code and a VHDL code generation on the basis of Matlab®/Simulink® are investigated to achieve a seamless and reliable transition between the simulation model and the execution code. The simulation-model based design will become more popular in a complex algorithm development in the future and there are some other similar types like Matlab-FPGA, Matlab-DSP. They can tremendously accelerate the development progress and shorten the research period.

1.2 Related work

Sensorless control of AC machine with multiple saliencies has been studied in publications since 1998. They focused on sensorless controlled IM and PMSM with decoupling of saturation induced or cross-saturation induced secondary saliencies. To be more specific, the saturation-induced secondary saliency results from the fundamental excitation or permanent magnet flux harmonics, while the cross-saturation induced secondary saliency arises from a load-dependent rotor flux displacement.

In 1998, the characteristics of multiple saliencies in AMs have been reported in [1]. In this study, the sensorless control was realized for an IM using the decoupling method, where higher orders of the saliency were decoupled from the primary saliency. In a later publication [2], the saturation induced as well as cross-saturation induced saliencies of an IM and their effects on HF signal injection based sensorless IM drives were discussed. These studies showed that the rotor flux information of an IM exists also in the magnetizing flux- and stator leakage flux-

induced secondary saliencies except in the primary saliency. Nevertheless, the rotor position of AMs which has a slip difference from the rotor flux position can be estimated only if there exists a manually created rotor-structure saliency. As a consequence, the estimations of these two positions need to be clarified clearly for an AM. On the contrary, the rotor position and permanent magnet flux position of a PMSM are exactly the same. Thus, the rotor position information exists in the multiple saliencies but it has little relation to the stator leakage.

Another attempt using the decoupling method was researched in 2008 with an IPMSM [3], where the higher order saliencies were only present in loaded condition which is not true for cwSPMSM. A neural network based decoupling method was developed in this paper but it was of complex structure and needed a longer time training process. In 2010, a comprehensive comparison of two general used sensorless methods, the rotating HF signal injection and the pulsating HF signal injection method, were published in [4] taking also the characteristic of multiple saliencies into consideration. From the mathematical expression point of view, both saturation induced or cross-saturation induced secondary saliencies have the same form. The respective errors introduced by these two kinds of secondary saliencies were analyzed in this paper as well. But, no concrete solution was presented and it was only valid for an IPMSM with distributed windings, which is different from a cwSPMSM.

A very interesting work was published in 2011 to study the principle of multiple saliencies phenomena in a PMSM [5]. This work proved that the higher order saliencies were evoked by the zigzag leakage of the rotor flux in the stator teeth. And this effect is more significant in machines with concentrated windings than with distributed windings. The author designed a cwSPMSM with a reversed saliency, $L_d > L_q$. The design can not only mitigate the load-dependent cross-saturation but also make the saliency ratio $\Delta L/\Sigma L$ independent of load condition. As a matter of fact, it is impractical to design such a special machine for general purposes and a common sensorless control method is expected. Other similar works are also seen in dealing with multiple saliencies for sensorless control, not only for SMs [6], but also for AMs [7–9].

In 2013, an arbitrary injection method was applied to the cwSPMSM in [10] and the author claimed that two original decoupling methods failed when the magnitude of the secondary saliency signal is higher than that of the primary saliency signal. The essence of this method was to build a multiple-saliency model, which demanded mass commissioning testes. However, no full-load test and standstill test were presented. In fact, it is still a challenge for position estimation at standstill with existence of strong secondary saliencies. The full-load test can reflect the rejection ability of the sensorless method to cross-saturation-induced rotor flux displacement and is therefore mandatory for evaluating a sensorless controlled PMSM drive system.

Summarizing the available literature, it can be seen that most of these studies were focused on the decoupling idea, where the higher order saliencies were compensated or removed from the control loop. This concept is effective if the higher order saliencies are weak compared to the primary saliency. Unfortunately, only few publications cope with sensorless control of cwSPMSM that shows strong multiple saliencies, which means the magnitude of secondary saliency signal is greater than half of primary saliency magnitude regardless of load condition and fundamental excitation. In this case, eliminating these secondary saliency signals means loss of information. In addition, the cwSPMSM under test also shows significantly different properties as the machines reported in the literature, which will be described in the Chapter (Ch.) 5. Therefore, the objective of this work is to investigate the detailed properties of cwSPMSM and to realize a feasible saliency tracking based sensorless control at standstill and

low speed range and eventually a full-speed range hybrid sensorless control system combining both saliency tracking based and fundamental model based method.

1.3 Outline

Following this introduction, Ch. 2 gives an overview of the state of the art of sensorless control. The two sensorless control categories are systematically introduced and analyzed. Meanwhile, the advantages and disadvantages of both types are summarized. In order to clearly explain the proposed methods, Ch. 3 introduces mathematical models of both PMSM and multiple saliencies. The symbols and notations for describing the system are defined as well in this chapter and utilized uniformly in the dissertation. The first 3 chapters provide required basic knowledge and lead to the solution of the multiple-saliency problem. Some hardware and software implementations are described in Ch. 4

In Ch. 5, three saliency tracking based sensorless control methods are proposed for the low speed range and standstill operation. Firstly, a Multi-Signal Injection (MSI) method is proposed in the manner of combining all saliency signals together with injections of two HF signals into the cwSPMSM. Secondly, a Secondary Saliency Tracking (SST) is designed based on the primary saliency decoupling. It utilizes the rotation difference of the primary and secondary saliency signal. Thirdly, a Repetitive Control (RC) method that decouples the secondary saliency signal is developed as a second decoupling attempt. Ch. 6 shifts the attention from saliency tracking based methods to fundamental model based methods for higher speed operation. There are also three types, Model Reference Adaptive System (MRAS), Sliding Mode Observer (SMO) and Extended Kalman Filter (EKF). Their operation mechanism and stability analysis are presented. Comparisons in terms of parameter-sensitivity and dynamic performance are carried out as well. In order to improve the system-robustness and self-adaptation, a multi-parameter identification of PMSM is studied in Ch. 7 on the basis of MRAS and EKF. Moreover, parameter identification related issues like identifiability and consideration of inverter non-linearity are investigated. Finally, this work is concluded in Ch. 8.

CHAPTER 2

State of the art

2.1 Introduction

Sensorless control of AC machine has been studied for a long time and there is a lot of literature dealing with different methods for different machines. This work focuses only on the sensorless control of PMSM drive system especially PMSMs with strong multiple saliencies.

As introduced in Ch. 1, there are two categories for the sensorless control of PMSM, the saliency tracking based method and fundamental model based method. The former one derives from the machine's saliency, which is actually a phenomenon of asymmetrical distribution of machine rotor flux due to the physical structure or saturation. Therefore, the differences between all saliency tracking based methods are the excitation signal, which excites or exaggerates the existing saliency in a PMSM, and the corresponding demodulation method. The latter one is built based on the mathematical model of a PMSM. However, the PMSM model has different expressions such as transfer function, state-space equations and simultaneous equations according to different requirements. Each of them has its own advantages as well as disadvantages. But, they have one thing in common: the parameters of the PMSM in the model change with the operation point and they should be on-line or off-line adaptively estimated. In this chapter, these sensorless method related issues and the state of the art will be addressed.

2.2 Saliency tracking based sensorless method

The saliency of a PMSM is the characteristic of a machine itself and has a close relation to the saturation property of permanent magnet material and especially machine design technique e.g., stator winding distribution, slotting and installation of permanent magnet [11–13]. For instance, the IPMSM has normally a higher saliency ratio than the SPMSM due to its asymmetrical installation of rotor magnets [14]. Obviously, the sensorless control of SPMSM is more difficult because of its weak geometrical saliency. Normally, the saturation-induced saliency of SPMSM

is utilized to estimate the rotor position. With the help of a Finite Element Analysis (FEA) tool provided by simulation software, the exact inductive or resistive saliency can be calculated and the simulation results are in high accordance with experiment measurements [15]. Thus, the sensorless-capability of a PMSM can be evaluated in case of knowing the exact machine design parameters. In reality, however, it is always impossible to get the detailed data of a commercial PMSM.

Saliency tacking (geometrical or saturation-induced saliency) based methods are usually adopted to estimate the rotor position at standstill and in low speed range. In these methods, additional HF signals are required to inject into the PMSM and excite or exaggerate the saliency signal. In terms of the injection signal pattern, saliency tracking based methods can be classified into two main groups: carrier-signal based and Pulse Width Modulation (PWM) switching pattern based. The carrier-signal based method means that the HF signals are superimposed on the fundamental signals and then the combined signals are fed as references to a PWM modulator. As a consequence, the carrier-signal based method is of simple structure and do not need to modify the existing hardware. But, the resolution of the PWM frequency has a significant impact on restoring the HF signal. Moreover, The inverter's non-linearity deteriorates further the problem. On the contrary to the carrier-signal based method, the PWM switching pattern based method focuses on either using the existing fundamental PWM excitation or modifying the switch-on and off times without introducing interference with the fundamental signals. In other words, this method pays attention to the modulator but not the reference. However, in most cases, the PWM switching pattern based method requires either oversampling of phase currents or additional hardware, e.g., current derivative sensors, midpoint wire of star-connected machine and inverter DC link voltage.

2.2.1 Carrier-signal based saliency tracking method

2.2.1.1 Rotating HF signal injection method

The rotating HF signal injection method was first proposed by Prof. Lorenz in [16] for an IM and later in [4] for a PMSM. The method treats the machine itself as a resolver and the same excitation and demodulation techniques employed by a resolver-to-digital converter are applied to estimate the position and speed of the machine.

The principle of the rotating HF signal injection method is depicted in Fig. 2.1. The outer blue line and inner red dotted-line represent the trajectory of the injected HF voltage signal $\boldsymbol{u}_c$ and its induced HF current signal $\boldsymbol{i}_c$, respectively. The excitation voltage signal rotates at a speed of $\boldsymbol{\omega}_c$ periodically in the Stationary Reference Frame (SRF) i.e., $\alpha - \beta$ frame which is the origin of its name "rotating". At the presence of a single saliency, the trajectory of $\boldsymbol{i}_c$ becomes an ellipse whose major axis is always aligned with the d axis. It is obvious that the rotor position information is hidden in the ellipse and a special demodulation technique is required to decode the rotor position e.g., Phase Locked Loop (PLL), phasor transformation and observer. More details can be found in Ch. 3.

2.2.1.2 Zero-sequence voltage or current based method

For the rotating HF signal injection method, the HF Negative-Sequence Current (NSC) contains the rotor position information. If the neutral point of a star-connected IM or PMSM is available,

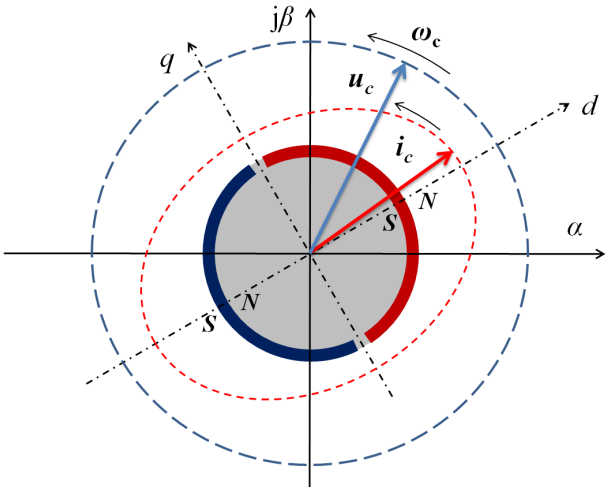

Figure 2.1: Rotating HF signal injection method in $\alpha - \beta$ frame.

the Zero-Sequence Voltage (ZSV), which can be measured by three phase-to-neutral point voltages or other auxiliary hardware connections [17], contains also the rotor position information like the NSC. Similar demodulation techniques and estimation methods from the NSC based method can be applied to the ZSV based method.

The corresponding Zero-Sequence Current (ZSC) based sensorless method was proposed in [18] for a delta-connected machine. This method requires access to the machine phase windings and an additional current sensor. Another ZSC based sensorless method can be found in [19]. It adopted test voltage injection and a current derivative sensor was required, which increases the cost of the whole system. A comparison between NSC, ZSV and PWM-induced ZSV were performed in [20] and their performance was similar because all of them share the same physical principle.

There are two obvious drawbacks for ZSV based sensorless methods compared to the NSC based method. Firstly, rare commercial PMSMs provide neutral-point access and thus a modification of machine winding is needed in advance. Secondly, the additional voltage or current sensors and their accessories result in additional cost.

2.2.1.3 Pulsating HF signal injection method

The Pulsating (or alternating) HF signal injection method was first seen in [21] for a PMSM. The method injected a sinusoidal HF voltage signal into the $\hat{q}$ axis and a corresponding demodulation technique utilizing i_{cd} was presented as well. The name “pulsating" means a HF pulsating signal is injected in the estimated $\hat{d} - \hat{q}$ frame. Nonetheless, the $\hat{q}$ axis injection scheme introduces noises and torque ripples to the system even if the estimated position converged to the real one. Thus, the estimated d axis HF signal injection method was proposed later in [22–26]. By contrast, it can avoid the disadvantages of its counterpart but maintain the same advantages. Therefore, the latter one was adopted widely in industry applications [27] and its detailed principle is explained in Fig. 2.2.

The outer blue solid-line represents the amplitude profile of the injected HF voltage signal $\boldsymbol{u}_c$ which pulsates along the estimated d axis and rotates together with the rotor at the same

time. The red double-arrow-line denotes the induced HF current signal $\boldsymbol{i}_c$, which is decomposed further by $\boldsymbol{i}_{cd}$ and $\boldsymbol{i}_{cq}$ in $\hat{d}-\hat{q}$ frame, respectively. If the $\hat{d}$ axis coincides with the d axis, the estimated position $\hat{\theta}$ and speed $\hat{\omega}$ converge to real values and $\boldsymbol{i}_{cd} = \boldsymbol{i}_c$ $\boldsymbol{i}_{cq} = 0$ in the ideal case. Hence, the value of $\boldsymbol{i}_{cq}$ can indirectly reflect the misalignment of the $d-q$ frame and the $\hat{d}-\hat{q}$ frame and is proportional to the estimated position error $\tilde{\theta} = \hat{\theta} - \theta$. All pulsating HF signal injection methods rely on the estimation error either $\boldsymbol{i}_{cd}$ or $\boldsymbol{i}_{cq}$ in accordance with $\hat{q}$ or $\hat{d}$ injection. The demodulation of estimation error, however, has different forms such as [22–24, 28] in accordance with different purposes. In addition, in terms of the shape of injected HF voltage, there are two popular types: sinusoidal form and square-wave form [25, 29]. The latter one shows better dynamic performance than the former one but it requires special demodulation technique.

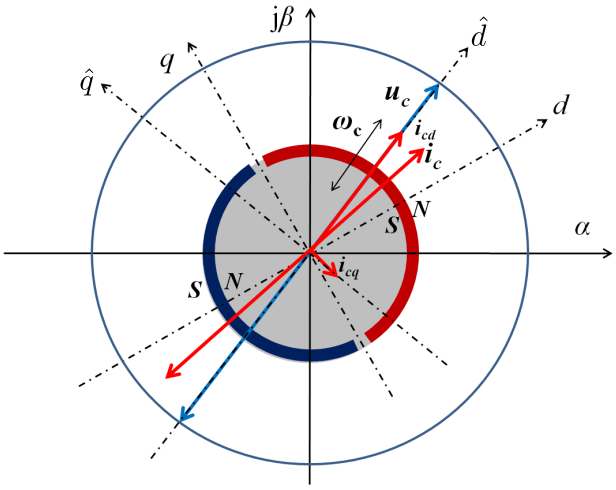

Figure 2.2: Pulsating HF signal injection method in $\hat{d}-\hat{q}$ frame.

A particular pulsating HF signal injection method performed in the $\alpha-\beta$ frame was proposed recently, including both the sinusoidal-wave type [26] and the square-wave type [30]. The visual description of this method can be found in Fig. 2.3, where the definitions of symbols are the same with Fig. 2.2. The difference is that the $\boldsymbol{i}_{c\alpha}$ and $\boldsymbol{i}_{c\beta}$ in $\alpha-\beta$ frame instead of $\boldsymbol{i}_{cd}$ or $\boldsymbol{i}_{cq}$ are amplitude-modulated by the rotor position and need to be demodulated.

2.2.2 PWM switching pattern based method

2.2.2.1 INFORM and its related method

The name INFORM stands for “Indirect Flux detection by On-line Reactance Measurement". It was proposed by Prof. Schroedl in 1988 and applied to different types of AC machines e.g, AM, PMSM, RM in [31]. The INFORM method was further improved in [32] so as to minimize the induced noise and losses by test voltages. Interruption of the fundamental PWM pattern for a specific period of time is required by the INFORM method to inject a manually designed sequence of test voltages, which are the basic six active vectors i.e.,$\boldsymbol{v}_1 - \boldsymbol{v}_6$ and two zero vectors i.e.,$\boldsymbol{v}_0, \boldsymbol{v}_7$ as shown in Fig. 2.4. As a result, the INFORM method is fundamental PWM pattern

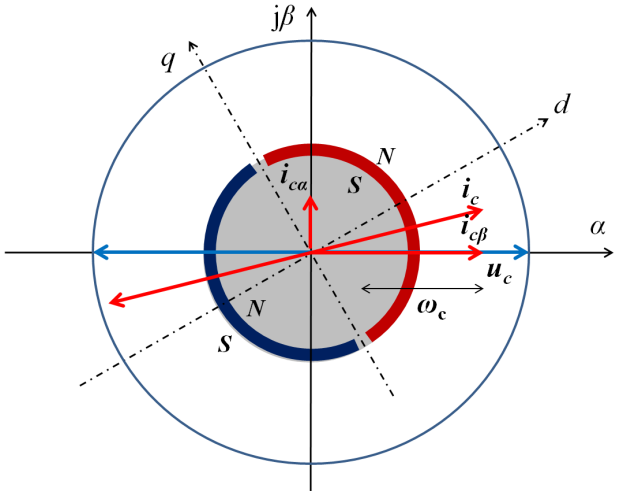

Figure 2.3: Pulsating HF signal injection method in $\alpha - \beta$ frame.

independent and the duration time and magnitude of the test voltages can be flexibly chosen by the designer according to different operation points or different machine types.

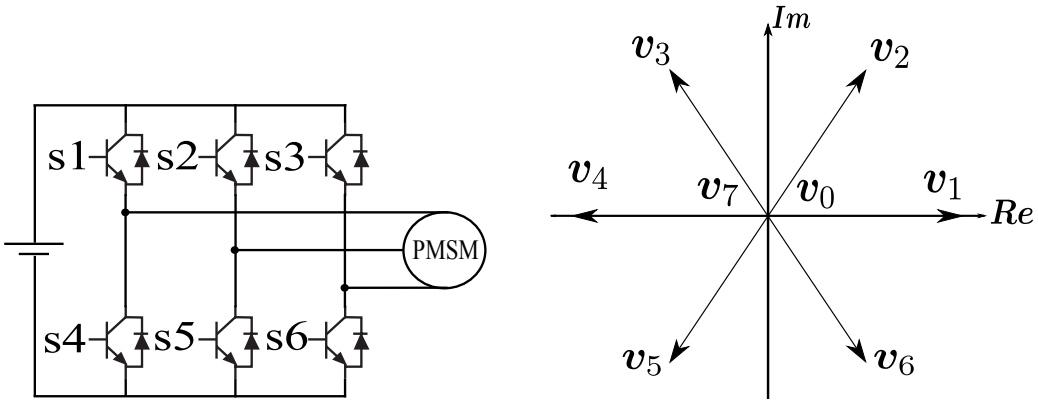

(a) Three-phase two-level inverter (b) Definition of voltage vectors

Figure 2.4: Inverter and voltage vectors.

The INFORM reactance $\boldsymbol{x}_{\text{INFORM}}$ and stator voltage model of a PMSM are presented in (2.1) and (2.2) respectively.

$$\boldsymbol{x}_{\text{INFORM}} = \frac{\boldsymbol{u}_s}{d\boldsymbol{i}_s/d\tau}, \tag{2.1}$$

$$\boldsymbol{u}_s = R_s\boldsymbol{i}_s + \underbrace{\frac{d\boldsymbol{\psi}_s}{d\tau} := \boldsymbol{L}_s\frac{d\boldsymbol{i}_s}{d\tau} + \boldsymbol{e}_s}_{\boldsymbol{\psi}_s = \boldsymbol{L}_s(\theta_e)\boldsymbol{i}_s + \boldsymbol{\psi}_{\text{PM}}}, \tag{2.2}$$

$$\boldsymbol{\psi}_{\text{PM}} = \psi_{\text{PM}} e^{j\theta_e} \tag{2.3}$$

$$\boldsymbol{e}_s = \frac{d\psi_{\text{PM}} e^{j\theta_e}}{d\tau} = j\omega_e\boldsymbol{\psi}_{\text{PM}}, \tag{2.4}$$

where $\boldsymbol{u}_s$, $\boldsymbol{i}_s$ and $\boldsymbol{e}_s$ are the stator voltage vector, stator current vector and back EMF, respectively. R_s is the stator resistance, $\boldsymbol{L}_s$ is the stator inductance matrix. $\boldsymbol{\psi}_s$ is the stator flux vector, $\boldsymbol{\psi}_{\text{PM}}$ and ψ_{PM} are vector representation and scalar magnitude of the permanent magnet flux of the PMSM, respectively.

Almost all saliency tracking based methods including INFORM treat the machine as a pure inductance load while the voltage drop $R_s\boldsymbol{i}_s$ and back EMF $\boldsymbol{e}_s$ are neglected when the machine runs at low speed range. $\boldsymbol{x}_{\text{INFORM}}$, therefore, is actually the inductance matrix $\boldsymbol{L}_s$ in the stator voltage model. The saliency orientation position can be observed by the variation of $\boldsymbol{x}_{\text{INFORM}}$, which is the basic idea of the INFORM method. A space phasor $\Delta\boldsymbol{i}_s$ combining the changes of the three phase currents during the duration interval of the test voltage is derived as in (2.5) to demodulate the rotor position that is included in the space angle of the phasor (2.6)

$$\boldsymbol{f}(\Delta\boldsymbol{i}_s) = \Delta\boldsymbol{i}_a + \Delta\boldsymbol{i}_b e^{\frac{4\pi}{3}} + \Delta\boldsymbol{i}_c e^{\frac{2\pi}{3}}, \tag{2.5}$$

$$\arg\boldsymbol{f}(\Delta\boldsymbol{i}_s) = 2\theta_e + \pi, \tag{2.6}$$

where $\Delta\boldsymbol{i}_a$, $\Delta\boldsymbol{i}_a$, $\Delta\boldsymbol{i}_a$ are the changes of three phase currents during the duration time interval Δt of active voltage vector $\boldsymbol{v}_1$, $\boldsymbol{v}_3$, $\boldsymbol{v}_5$, respectively.

As introduced before, the fundamental PWM pattern is not consecutive during test voltage injection and the duration time selection of these active test vectors should be a tradeoff between the interference with fundamental PWM and the SNR of the current derivative signals.

Another similar attempt, where a slight modification of the inherent fundamental PWM pattern was necessary, can be found in [33]. Within this method, the transient ZSV of the stator winding was measured through three phase currents in response to specific modified PWM transients. In terms of implementation, this method is similar to the INFORM method but the modification of the PWM pattern and its related rotor position demodulation are different.

2.2.2.2 Fundamental PWM-integrated method

On the contrary to the INFORM method, the Fundamental PWM-Integrated (FPWMI) method [7, 10, 34–36] relies only on the inherent fundamental PWM-induced effects. As a result, the interruption of the PWM and HF signal injection are not necessary. Most of these FPWMI methods utilize a SVPWM technique in which the switch sequences are symmetrical and flexible to adapt changes of duration time without introducing interference to the fundamental components.

In [34], a classical FPWMI method was introduced and it showed higher dynamic response than the INFORM method. The basic principle is that the phase inductance is rotor position modulated. Hence, the derivative of phase current during the excitation of active vectors reflects the variation of inductance, and indirectly implies the rotor position information. As mentioned in [34], a space phasor whose angle is the rotor position was skillfully formulated based on three phase current derivatives. Obviously, the measurement accuracy of current derivative affects the overall estimation performance. In addition, the required current derivative sensor itself dose not exist in a normal industrial control platform and thus the implementation of this method still faces several obstacles in practice.

During recent years, an arbitrary injection scheme based sensorless control has been proposed in [10, 35, 36] for the whole speed range operation of a PMSM. Its essence is to build an ideal

isotropic model of a PMSM which has actually an anisotropic characteristic i.e., saliency. Thus, the rotor position information of a PMSM exists in the difference between the isotropic model and the anisotropic model (real machine model). At lower speed range without load, the inherent SVPWM modulator is dominated by zero space vector i.e.,$\boldsymbol{v}_0$ and $\boldsymbol{v}_7$. The duration time of the six active vectors, in this case, is not long enough to excite observable current ripples, on which the arbitrary injection method highly relies. A slight modification of the PWM pattern, therefore, is required to extend the duration time of active vectors, whereas the modification is unnecessary in the high speed range or at loaded-condition due to enough excited current ripples. The arbitrary injection method depends also highly on the accuracy of measurements of the current derivative. Moreover, the precise sampling of current signal during specific switching instance is still a challenge for an off-the-shelf industrial control platform. It needs to be further improved to adapt to practical applications where the sampling frequency and precision of the current sensors are limited.

2.3 Fundamental model based sensorless method

In the previous section, the first category of sensorless control methods has been comprehensively introduced. It can be seen that most of the saliency based methods except FPWMI neglect the back EMF term in the machine model (2.2) in order to simplify the machine model as a pure inductive load, which is a reasonable approximation in the lower speed range. But, the assumption does not hold true when the speed goes higher especially near its rated speed and the back EMF term dominates $\boldsymbol{e}_s$ in the right hand side of (2.2). As a result, saliency based sensorless method, in this case, would have a higher estimation error of position and should be replaced by a fundamental model based method. The hybrid sensorless control becomes more popular and is regarded as a complete solution for the whole speed range sensorless control [27, 37]. $\boldsymbol{e}_s$ can be further expressed in $\alpha - \beta$ frame as follow

$$\boldsymbol{e}_s = -\omega_r \psi_{\text{PM}} sin\theta_e + j\omega_r \psi_{\text{PM}} cos\theta_e = e_\alpha + e_\beta. \tag{2.7}$$

It is obvious that the rotor position can be calculated as

$$\theta_e = arctan\frac{-e_\alpha}{e_\beta}. \tag{2.8}$$

This is the theory basis of several fundamental model based methods and it is straightforward to realize. However, other fundamental model based methods utilize the adaptive estimation mechanism [38] based on the observer design theory. In the following subsections, some important branches of the fundamental model based method are introduced briefly.

2.3.1 Active flux observer

The Active Flux Observer (AFO) originates form the machine voltage model and was summarized in [39] as a general sensorless method for almost all AC machines. The concept of AFO refers to the torque-producing flux in the electromagnetic torque formulas of AC machines. In

this work, only PMSM is considered and thus its equation derivation is performed as an example. However, the AFO can be applicable to other types of AC machines as well [39]. The active flux is $\boldsymbol{\psi}_{\text{PM}}$ in a PMSM and it can be calculated as

$$\boldsymbol{\psi}_{\text{PM}} = \int (\boldsymbol{u}_s - R_s \boldsymbol{i}_s + \boldsymbol{u}_{\text{comp}}) d\tau - \boldsymbol{L}_s \boldsymbol{i}_s. \tag{2.9}$$

where $\boldsymbol{u}_{\text{comp}}$ is a compensation component and it accounts for the inverter non-linearity and other effects e.g., dead time, integration dc-offset and stator resistance variation. The $\boldsymbol{u}_{\text{comp}}$ is considered in (2.9) for practical issues in order to solve the drift problem resulting from a pure integrator.

The block diagram of AFO is shown in Fig. 2.5 where the rotor position is estimated through a PLL ②. The PLL can be replaced by an $arctan$ calculation ① as well. The structure of the AFO is simple and straightforward. As a consequence, it has been adopted by [8,38,40,41] with different compensation calculation. However, machine parameters e.g., $\boldsymbol{L}_s$, R_s and $\boldsymbol{\psi}_{\text{PM}}$ affect the overall performance of the AFO and need to be adaptively estimated by other observers. The combination of AFO with parameter observer has been implemented and detailed procedures and results can be found in Ch. 7.

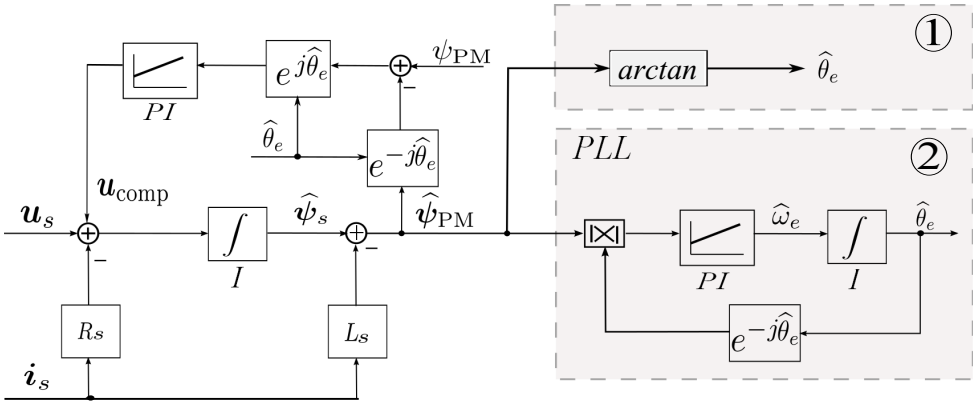

Figure 2.5: Active flux observer with PLL.

2.3.2 Model reference adaptive system

The basic structure of a Model Reference Adaptive System (MRAS) is shown in Fig. 2.6 where a reference model and an adjustable model are adopted. All parameters in the reference model are assumed to be known in advance from either the nameplate or measurements. Whereas, an unknown parameter or parameter vector $\widehat{\boldsymbol{y}}$ exists in the adjustable model depending on the machine model. In this work, $\widehat{\boldsymbol{y}}$ is $\widehat{\theta}_e$ or $\widehat{\omega}_e$. They can be estimated through an adaptive controller that is designed based on Popov's stability theory. The outputs of these two models are $\boldsymbol{x}$ and $\hat{\boldsymbol{x}}$ that represent the same physical quantity. The output can be any specific signal e.g., current [42, 43], stator or rotor flux $\boldsymbol{\psi}_s$ $\boldsymbol{\psi}_r$ [44] and reactive power [45] for PMSM. An error signal ε is produced by comparing $\boldsymbol{y}$ and $\hat{\boldsymbol{y}}$ and then fed to the adaptive controller.

Normally, a Proportional-Integral (PI) controller is adopted as the adaptive controller, which simplifies the implementation of MRAS in a digital signal processor. The feasibility of choosing

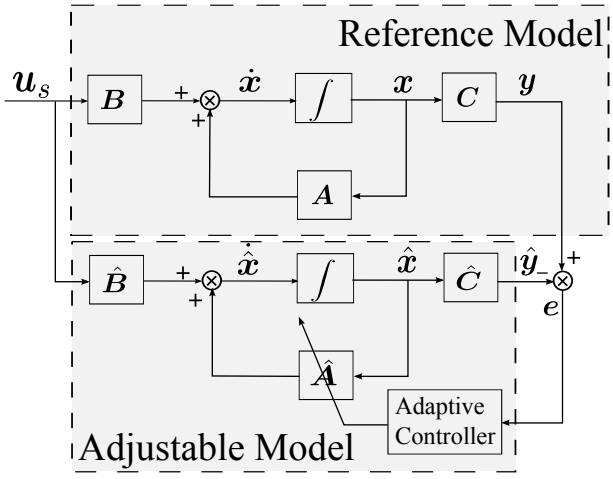

Figure 2.6: Model reference adaptive system.

the adjustable model makes it more competitive than other fundamental model based methods. However, MRAS has the same drawback as AFO. It is machine parameters-dependent i.e.,R_s, L_s, ψ_{PM}. As a result, the on-line parameters identification is also necessary for obtaining a high-dynamic and operation-point independent control performance.

2.3.3 State-space based observer

The state-space equation describes the PMSM model in matrix form which enables a concise and effective analysis of system performance e.g., stability, observability, dynamic improvement through pole placements. In general, an arbitrary system can be written as

$$\begin{aligned} \dot{\boldsymbol{x}} &= \boldsymbol{A}\boldsymbol{x} + \boldsymbol{B}\boldsymbol{u} \\ \boldsymbol{y} &= \boldsymbol{C}\boldsymbol{x} \end{aligned} \tag{2.10}$$

where $\boldsymbol{A}$, $\boldsymbol{B}$ and $\boldsymbol{C}$ are matrices with different dimensions in accordance with the system order, $\boldsymbol{x}$ and $\boldsymbol{y}$ are referred to as state variables and outputs, $\boldsymbol{u}$ is the system input. The basic principle of a state observer is to construct an estimated model having a similar structure as (2.10). It can be described as

$$\begin{aligned} \dot{\hat{\boldsymbol{x}}} &= \hat{\boldsymbol{A}}\hat{\boldsymbol{x}} + \hat{\boldsymbol{B}}\boldsymbol{u} + \boldsymbol{K}\boldsymbol{f}(\hat{\boldsymbol{y}} - \boldsymbol{y}) \\ \hat{\boldsymbol{y}} &= \hat{\boldsymbol{C}}\hat{\boldsymbol{x}} \end{aligned} \tag{2.11}$$

where $\hat{}$ represents the estimated quantity of a parameter in accordance with (2.10). The only difference between (2.10) and (2.11) is the additional adjustable item $\boldsymbol{K}\boldsymbol{f}(\hat{\boldsymbol{y}} - \boldsymbol{y})$. $\boldsymbol{K}$ is a gain matrix and it forces the estimated parameters in $\hat{\boldsymbol{A}}, \hat{\boldsymbol{B}}$ and $\hat{\boldsymbol{C}}$ to converge to their real values. And then, the stability of the whole observer can be guaranteed. The selection criteria of $\boldsymbol{K}$ relies on stability theories of different observers, and thus, is a symbol to differentiate the type of observer as well. Meanwhile, the $\boldsymbol{f}(.)$ indicates a linear e.g., $\boldsymbol{f}(z) = z$ or nonlinear e.g., $\boldsymbol{f}(z) = \boldsymbol{sign}(z)$ function, which is another symbol for distinguishing different observers. The possible combination of $\boldsymbol{K}$ and $\boldsymbol{f}(.)$ are summarized as follows. Note that, the state variable vector $\boldsymbol{x}$ in each observer is changeable and not always the same. They can be performed even in different frames.

2.3.3.1 Luenberger observer

- $\boldsymbol{K}$ = Constant or Speed-dependent, $\boldsymbol{f}(z) = z$

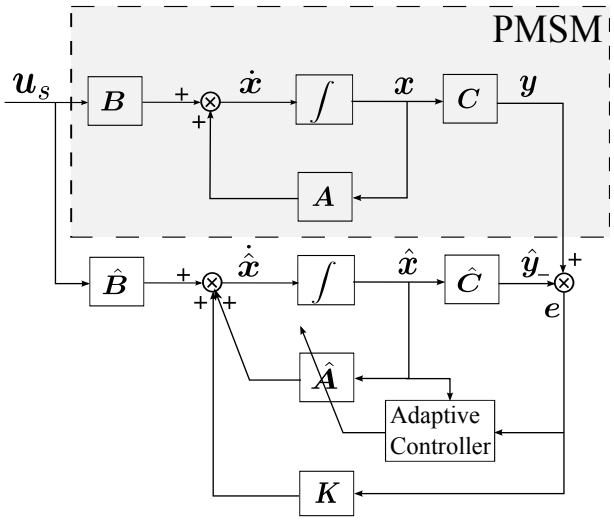

Figure 2.7: Luenberger observer.

The Luenberger Observer (LO) as shown in Fig. 2.7 is deterministic and applicable to a linear and nonlinear system (Extended Luenberger Observer (ELO) is required). The stability of the error dynamics of the LO and also other observers mentioned in the next subsections can be guaranteed by Popov's hyper-stability theorem or Lyapunov's stability theorem. The corresponding procedures of stability proof can be found in [38].

The feedback gain matrix $\boldsymbol{K}$ has constant or speed-dependent values, depending on the eigenvalues chosen for $\boldsymbol{A} - \boldsymbol{KC}$ in a way that the system is stable and the transient of the designed observer is faster than the PMSM model. The feedback error $\hat{\boldsymbol{y}} - \boldsymbol{y}$ is the difference between the measured and estimated state variables or outputs of interest. In order to apply the LO or ELO for sensorless control of PMSM, the speed or position of the PMSM that exist only in the system matrix $\hat{\boldsymbol{A}}$ should be estimated. The adaptation mechanism of estimating speed or position is deduced from stability analysis, which follows the similar way as MRAS. The convergence rate of LO is $\boldsymbol{K}$ times faster than that of MRAS. However, $\boldsymbol{K}$ can not be chosen too high because the environment and measurement noise are magnified as well. A compromise for choosing $\boldsymbol{K}$ should be made such as making it speed-dependent. The drawback of LO or ELO is the low robustness to parameters variation and noise interference.

2.3.3.2 Extended Kalman filter

- $\boldsymbol{K}$ = Time-Variable, $\boldsymbol{f}(z) = z$

The Kalman Filter (KF) shown in Fig. 2.8 belongs to the class of stochastic observers and it takes the system noise and measurement noise, which are normally neglected by other observers, into consideration. The gain matrix $\boldsymbol{K}$ of the KF is updated adaptively at each calculation step with the goal of minimizing the state or output errors $\hat{\boldsymbol{y}} - \boldsymbol{y}$, and therefore, it is

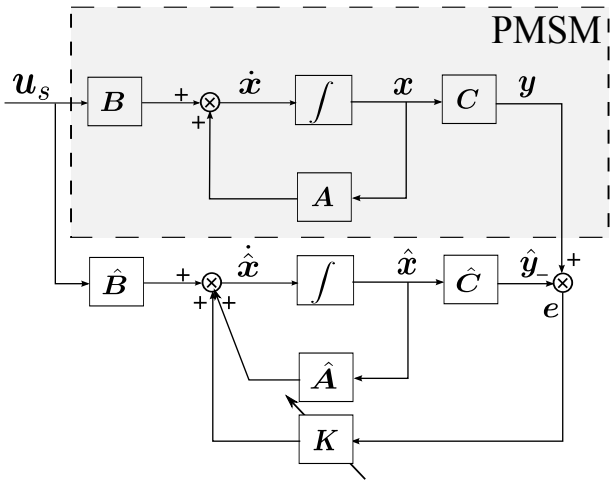

Figure 2.8: Extended Kalman filter.

time-variant. The traditional KF can be extended to a nonlinear system as well and it is called the Extended KF (EKF), which is popular in high-performance servo systems because of its accurate estimation in a wide speed range and even in noisy environment.

The EKF is proposed based on the minimization theory of the mean square error. Each calculation step, it can predict the most probable states i.e., the optimum outputs in the next step, which are utilized together with the noise matrix for updating the gain matrix $\boldsymbol{K}$. Detailed information of implementing an EKF in sensorless control of PMSM can be found in Ch. 6. Owing to the complex calculation involved in EKF, the execution of EKF in a digital controller occupies more resources than other observers.

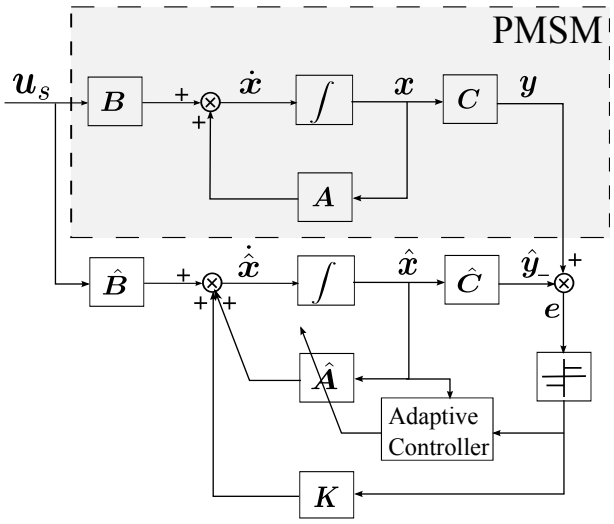

Figure 2.9: Sliding mode observer.

2.3.3.3 Sliding mode observer

- $\boldsymbol{K}$ = Constant or Speed-dependent, $\boldsymbol{f}(z) = \boldsymbol{sign}(z)$

The Sliding Mode Observer (SMO) as shown in Fig. 2.9 is described and analyzed on a superplane of system states, where a sliding motion is guaranteed by Lyapunov's stability theorem. The value of the gain matrix $\boldsymbol{K}$ is constant or speed-dependent and should be high enough to ensure the convergence of the SMO. In comparison with the previously introduced EKF and LO, the remarkable difference of the SMO is its feedback error expression $\boldsymbol{f}(z) = \boldsymbol{sign}(z)$, which always leads to a high feedback gain even if the error is small. High feedback gain enhances system robustness to parameter variation. The chattering problem resulting from the $\boldsymbol{sig}$ function is the main obstacle that impedes the wide application of SMO.

2.4 Parameter identification of PMSM

In the observers mentioned in the previous section, $\hat{\boldsymbol{A}}$, $\hat{\boldsymbol{B}}$ and $\hat{\boldsymbol{C}}$ contain not only speed ω_e or position θ_e but also other machine electrical parameters e.g., ψ_r, ψ_{PM}, R_s and L_s, which are treated normally as constant values for every operation point. In reality, however, they change with the load, temperature and saturation. As a result, the on-line or off-line parameter identification becomes necessary so as to make the system itself adaptive to parameter variation, or detect faults to avoid further damage of the control system. For example, in certain high-performance controllers or control strategies e.g., Dead-Beat (DB) control, MTPA control and copper/iron loss minimization control, the electrical parameters are required inside the controller for achieving different purposes adaptively. Moreover, fault prediction/detection or system health monitoring become more and more important in the application of PMSMs like aerospace or remote control. The machine parameters behave actually as monitors that give feedback to the system controller for justifying if there is a fault. As a consequence, the parameter identification is important for strengthening the system robustness. In this section, three categories of parameter identification method will be introduced.

2.4.1 HF signal injection based off-line parameter identification

In general, saliency tracking based sensorless methods are independent of machine parameters. In several cases, however, the inductance e.g., L_d, L_q, L_{dq}-incremental inductance (l_d, l_q, l_{dq}-apparent inductance) or flux linkage e.g., $\psi_d, \psi_q, \psi_{dq}$ are required by saliency based algorithms [26, 46, 47]. Fortunately, the HF signal injection method and its related demodulation technique can be applied also to identify machine parameters in the entire $i_d - i_q$ plane. The identification is usually performed with the help of an encoder or resolver integrated with the PMSM. The results, in most cases, are calculated off-line and then stored as a Look-Up Table (LUT) in memory. In practice, other parts of the controller that need these measured parameters pick up data from the LUTs in accordance with the operation point.

For example, the HF pulsating signal and rotating signal injection methods were adopted in [26, 47, 48], respectively. In [26] and [48], the HF signal $u_c = V_c cos(\omega_c t)$ was injected into the $d-$ axis to obtain the relevant $dq-$ axis HF currents i.e. i_{dc1} and i_{qc1}, and then applied to

$q-$ axis to get i_{dc2} and i_{qc2}. These voltages and currents are applied to the HF machine model which is assumed as a pure inductance load, as shown in the following equation

$$\begin{bmatrix} u_c & 0 \\ 0 & u_c \end{bmatrix} = \begin{bmatrix} L_d & L_{dq} \\ L_{qd} & L_q \end{bmatrix} \frac{d}{dt} \begin{bmatrix} i_{dc1} & i_{dc2} \\ i_{qc1} & i_{qc2} \end{bmatrix}. \tag{2.12}$$

Both sides of (2.12) are multiplied by a $2cos(\omega_c t)$ and then applied to a Low Pass Filter (LPF) to give

$$\begin{bmatrix} V_c & 0 \\ 0 & V_c \end{bmatrix} = \omega_c \begin{bmatrix} L_d & L_{dq} \\ L_{qd} & L_q \end{bmatrix} \begin{bmatrix} I_{dc1} & I_{dc2} \\ I_{qc1} & I_{qc2} \end{bmatrix} \tag{2.13}$$

where $I_{dc1}, I_{dc2}, I_{qc1}, I_{qc2}$ are amplitudes of the corresponding HF currents. Then the inductance matrix is obtained by solving (2.13) as

$$\begin{bmatrix} L_d & L_{dq} \\ L_{qd} & L_q \end{bmatrix} = \frac{1}{\omega_c} \begin{bmatrix} u_c & 0 \\ 0 & u_c \end{bmatrix} \begin{bmatrix} I_{dc1} & I_{dc2} \\ I_{qc1} & I_{qc2} \end{bmatrix}^{-1}. \tag{2.14}$$

In [47], the L_d, L_q and L_{dq} were measured through the HFI method and an off-line curve fitting. The data was finally stored in a LUT. Then, a Recursive Least Square (RLS) was applied to further estimate the R_s and ψ_{PM} based on the existing LUT. Detailed procedures are described as follows. A pulsating HF voltage signal $u_c = V_c sin(\omega_c t)$ is injected into the stationary reference frame and its excited HF current vector is expressed as

$$i^s_{dqc} = I_{cp} e^{j(\omega_c t - \pi/2)} + I_{cn} e^{j(-\omega_c t + 2\theta_e + \varphi - \pi/2)} \tag{2.15}$$

$$\begin{aligned} L_d &= \frac{V_c(I_{cp} - I_{cn}\sqrt{\frac{1}{\tan(2\theta_{err})^2+1}})}{\omega_c(I_{cp}^2 - I_{cn}^2)} \\ L_q &= \frac{V_c(I_{cp} + I_{cn}\sqrt{\frac{1}{\tan(2\theta_{err})^2+1}})}{\omega_c(I_{cp}^2 - I_{cn}^2)} \\ L_{dq} &= \frac{V_c I_{cn} \tan(2\theta_{err})\sqrt{\frac{1}{\tan(2\theta_{err})^2+1}}}{\omega_c(I_{cp}^2 - I_{cn}^2)} \end{aligned} \tag{2.16}$$

The HFI based parameter measurement is insensitive to operation point and accurate in practice. Moreover, there is no divergence problem in comparison with observer based parameter identification method. However, the noise and loss resulting form the injected HF signal and the phase shift introduced by filters in the demodulation part should be considered.

2.4.2 Fundamental model based parameter identification

As explained already, the fundamental model of a PMSM contains machine parameters. As a consequence, if some of the parameters are measured during experiments, the other unknown

parameters can be calculated. The method follows the linear algebra theory. For example, the voltage equations in the synchronous $d-q$ coordinate frame are

$$\begin{aligned} v_d &= i_d R_s + \frac{d\psi_d}{dt} - \omega_e \psi_q = i_d R_s + L_d \frac{di_d}{dt} + L_{dq} \frac{di_q}{dt} - \omega_e \psi_q \\ v_q &= i_q R_s + \frac{d\psi_q}{dt} + \omega_e \psi_d = i_q R_s + L_q \frac{di_q}{dt} + L_{dq} \frac{di_d}{dt} + \omega_e \psi_d \end{aligned} \tag{2.17}$$

where ω_e is the sychronous speed, R_s is the phase resistance, and ψ_d and ψ_q are the $d-$ and $q-$ axes flux linkages. At steady state operation i.e.,constant speed with constant load, considering only fundamental components in (2.17), the derivation of (2.17) can be substituted by

$$\begin{aligned} v_d &= i_d R_s - \omega_e \psi_q \\ v_q &= i_q R_s + \omega_e \psi_d. \end{aligned} \tag{2.18}$$

From (2.18) and using the measured values of the v_d, v_q and i_d, i_q, the ψ_d and ψ_q can be calculated [49]. Assuming the ψ_{PM} is constant and the cross-coupling inductance $L_{dq} = L_{qd} = 0$, the apparent l_d and l_q can be obtained by

$$\begin{aligned} l_d(i_d, i_q) &= \frac{\psi_d - \psi_{\text{PM}}}{i_d} \\ l_q(i_d, i_q) &= \frac{\psi_q}{i_q}. \end{aligned} \tag{2.19}$$

And the transient inductance can be acquired from the slope of the flux linkage curves and shown as

$$\begin{aligned} L_d(i_d, i_q) &= \frac{\partial \psi_d}{\partial i_d} \quad L_{dq}(i_d, i_q) = \frac{\partial \psi_d}{\partial i_q} \\ L_q(i_d, i_q) &= \frac{\partial \psi_q}{\partial i_d} \quad L_{qq}(i_d, i_q) = \frac{\partial \psi_q}{\partial i_q}. \end{aligned} \tag{2.20}$$

Another fundamental model based parameter identification method can be found in [50, 51]. In [50], a position offset-based method was proposed to measure the ψ_{PM} and R_s. The conventional quantum genetic algorithm was adopted in the method. In [51], two Recursive Least Square (RLS) algorithms were utilized to estimate L_d, L_q, R_s and θ_e on-line.

These methods listed in this subsection are straightforward and simple to realize in practice. Nevertheless, several issues e.g., magnet heating, core loss need to be taken into account for getting more accurate results.

2.4.3 Observer based on-line parameter identification

In addition to the two previously mentioned categories, there are other observer based parameter estimation methods e.g., EKF and MRAS, which can be applied to estimate machine electrical parameters as well. Moreover, the stability analysis of observers for machine electrical parameter is the same as the previously introduced sensorless observers. However, not all the electrical parameters can be estimated simultaneously [52]. In addition, several requirements should be satisfied in advance to guarantee the identifiability of the PMSM electrical parameters.

On the contrary to the HF injection based parameter identification, the observer based parameter identification is performed on-line and the results can be adopted by any other parts of the controller immediately without any delay.

2.4.3.1 EKF based parameter identification

The structure of the EKF observer has been demonstrated in Fig. 2.8 where it is used to estimate ω_e and θ_e. The same principle of EKF observer design can be extended to estimate other machine electrical parameters [42, 52–54]. Especially in [54], two kinds of EKF i.e., current based or stator flux based were analyzed and summarized in a table, which gave a comprehensive introduction about the application of EKF in parameter identification of PMSMs.

The virtues of EKF based parameter identification is that the estimation performance is robust to noisy environments since the system noise and measurement noise are considered in the derivation of the optimum gain matrix. Moreover, the gain matrix $\boldsymbol{K}$ is updated each step according to the minimization of the state's mean square error. As a result, it is an adaptive observer that is robust to operation points in comparison with other observers with fixed gain matrix $\boldsymbol{K}$ e.g., LO, MRAS.

2.4.3.2 MRAS based parameter identification

As introduced in Fig. 2.6, the MRAS observer can be extended to estimate other machine electrical parameters as well. The examples can be found in [52, 55, 56], where different adaptive controllers were adopted taking advantage of the flexibility of the MRAS design principle.

Particularly in [55], a hybrid sensorless method combining MRAS and alternating HFI method was proposed for PMSM. MRAS was adopted to estimate ω_e and θ_e based on the $d-$ axis current error i.e. $\tilde{i_d} = i_d - \hat{i_d}$. The estimation error signal ϵ generated by the alternating HFI method was brought into the adaptive controller of MRAS as an auxiliary correction factor when the speed of PMSM was low. Meanwhile, the R_s was estimated based on ϵ as well through a second order tracking observer (cascade PI and an Integral). On the contrary, when the speed was higher, ϵ was removed from the MRAS loop. Instead of estimating R_s, the ψ_{PM} was estimated on the basis of $q-$ axis current error $\tilde{i_q}$. The method introduced in [55] was proven by stability analysis and then validated by simulation and experimental results. It showed the flexibility of MRAS that can be easily combined with any other schemes. In [56], a similar parameter estimation scheme for a PMSM was proposed.

The MRAS based parameter identification has merits of precise estimation and low computation-burden for a digital controller. The flexibility of combining it with other schemes is a superiority as well. It, however, has lower robustness to environment noise i.e., it is sensitive to the accuracy of the measured current and voltage signals.

2.5 Summary

This chapter gives a comprehensive literature review of sensorless control methods for PMSM drives. The saliency tracking based method, fundamental model based method and parameter identification are introduced.

In general, the saliency tracking based sensorless method is machine parameter-independent, because the saliency that results from asymmetrical geometry or saturation is an intrinsic characteristic of the machine itself. As a consequence, this method is normally adopted for the low speed range and even at standstill. On the contrary, the fundamental model based method works better in the middle and high speed range because of the high back EMF and high SNR.

It results in a more accurate estimation of the position compared to the saliency tracking based method, where the back EMF is neglected and noise and losses are produced. However, the drawback of the fundamental model based method is machine electrical parameter-dependent. Therefore, parameter identification is necessary to enhance the robustness of the control system.

It can be concluded from this chapter that a hybrid sensorless control system, which adopts the saliency tracking based method in the low speed range and at standstill and the fundamental model based method together with parameter identification in the higher speed range, provides a complete solution.

CHAPTER 3

Machine model and saliency model

The control theory and the parameter estimation theory rely highly on the accurate model of the machine, which is normally represented by a set of mathematical equations or matrices. In order to clearly demonstrate the relation between different models, the symbol definition and nomenclature inside these equations or matrices are introduced firstly in this chapter. Then, the machine models of the PMSM in different reference frames are derived. They are the foundation knowledge of various observers mentioned in the Ch. 2. Finally, the saliency and multiple-saliency model of the PMSM are presented so as to ease the understanding of HFI based sensorless methods. Meanwhile, the multiple-saliency model is utilized by different demodulation techniques to estimate the rotor position and speed.

3.1 Symbol definition and nomenclature

The analysis of machine model and control theory is performed by mathematical equations in which various symbols are utilized to distinguish different physical or visual quantities. Without a uniform definition, the understanding of any theory becomes impossible. Therefore, the symbol definition and nomenclature are introduced before the introduction of the machine model and saliency model which contain more sophisticated expressions.

3.1.1 Symbol explanation

The symbol which represents both a variable or constant adopted in this work is demonstrated as

$$\dot{x}_i^j, \tag{3.1}$$

where x, j and i represent the variable name, reference frame and types of quantity, respectively. In addition, the top-script $\dot{}$ represents a math operation or the origin of the variable e.g.,

estimated or measured quantity. In the following tables, each part of the general symbol is introduced in detail and they are represented in the standard international unit.

Symbol	***Description***
u,ψ	voltage and flux linkage
i,e	current and back EMF
j	imaginary axis or imaginary part of a complex quantity
f	fundamental electrical frequency
p	pole pairs of PMSM
R, L, l	resistance, incremental inductance and apparent inductance
T, ω, θ	torque,speed and angle
J, F	inertia and friction coefficient
x, X	arbitrary quantity for general introduction

Table 3.1: List of symbol representations

The symbol refers to a scalar time-variant quantity (lower-case) or a scalar constant (upper-case). In order to simplify the expression with a set of individual equations, a matrix expression, in which vectors and matrices are adopted, is used in some cases. As a result, in addition to the scalar symbol, the default $n \times 1$-dimension column vector and $n \times m$-dimension matrix are represented by a bold lower-case symbol e.g., $\boldsymbol{i}_r^r$ and a bold upper-case symbol e.g., $\boldsymbol{L}_s^s$, respectively.

Subscript	***Description***
s	stator quantity
r	rotor quantity
e	fundamental or electrical component
m	mechanical component
c	HF component
ref	reference instruction quantity
err	error signal
cp, cn	HF positive and negative component
a, b, c	stator phase winding
α, β	stator fixed Cartesian axes
d, q	real rotor fixed Cartesian axes or any rotation Cartesian axes e.g., i_{dqc}^{cn} means the HF current vector in negative sequence current frame
$\hat{d}, \hat{q}$	estimated rotor fixed Cartesian axes
x, y	arbitrary Cartesian axes
Σ, Δ	average and difference
PM	abbreviation of permanent magnet

Table 3.2: List of subscripts

The subscript and superscript identify the reference frame and the type of each quantity, respectively, e.g., i_d^r means the $d-$ axis current in the rotor fixed frame. For simplicity, because both superscript and subscript can refer to different frames, if one of them exists already, the other one can be omitted e.g, $i_d^r = i_d$ and $\boldsymbol{i}_{dq}^r = \boldsymbol{i}^r = \boldsymbol{i}_{dq}$.

Superscript	***Description***
s	stator fixed frame
r	rotor fixed frame
$\hat{r}$	estimated rotor fixed frame
cn	HF negative sequence fixed frame
T	transposition matrix
-1	inverse matrix or reciprocal of a quantity

Table 3.3: List of superscripts

Top-script	***Description***
$\dot{x}$	differential operation
$\hat{x}$	estimated quantities
$\tilde{x} = x - \hat{x}$	error between measured and estimated quantity

Table 3.4: List of top-scripts

The different types of top-scripts can be combined e.g.,$\dot{\tilde{\boldsymbol{i}}}_r = \dot{\boldsymbol{i}}_r - \dot{\hat{\boldsymbol{i}}}_r$ which means the transient dynamic difference of the current and is useful for concise stability analysis of an observer.

3.1.2 Reference frame

The most used AC machine is constructed with three phase symmetrical windings located 120° electrical away from each other. The analysis on the basis of three phase winding equations is theoretically feasible but mathematically complex. As a consequence, the transformation of the machine parameters from the three phase frame to the two phase frame (e.g., stator fixed or rotor fixed frame) is necessary. The conversion principle is that the magnetomotive force stays the same in all frames. The relation between the four commonly used frames is shown in Fig. 3.1. The four frames comprise the following: stator three phase winding axis fixed frame $a-b-c$, stator two phase equivalent winding fixed frame $\alpha-\beta$, rotor flux fixed frame $d-q$ and estimated rotor flux fixed frame $\hat{d}-\hat{q}$. The one-pole pair structure of a permanent magnet rotor is illustrated in Fig. 3.1 so that the North (N) and South (S) poles and their relation with the $d-q$ frame is clearly demonstrated. From Fig. 3.1, it is also clear that the α axis is aligned with a axis. In addition, the rotor position θ_e is defined as the position difference between d axis and a axis. The anticlockwise is the increase direction of position quantity. These artificial definitions can simplify greatly the transformation matrix, and therefore, are adopted in most control theory of AC machine.

3.1.3 Space vector representation

In order to further simplify the analysis of any symmetrical three phase machine and perform transformation between different frames, a general space vector is defined as

$$\boldsymbol{x} = \frac{2}{3}(x_a + x_b\boldsymbol{a} + x_c\boldsymbol{a}^2), \tag{3.2}$$

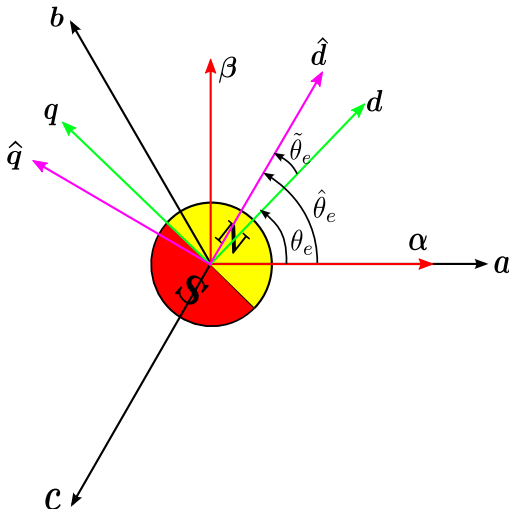

Figure 3.1: Orientation of reference frames.

where $\boldsymbol{x}$ is a defined space vector in $a-b-c$ frame and x_a, x_b and x_c are transient three phase components in a, b and c axis, respectively. The rotation factors are $\boldsymbol{a} = e^{j2\pi/3}$, $\boldsymbol{a}^2 = e^{j4\pi/3}$ and they are actually the spatial locations of the b and c axis. Assuming three phase symmetrical quantities exist in the windings, they can be represented by

$$\begin{aligned} x_a &= X_a \cos(\omega t), \\ x_b &= X_b \cos(\omega t - 2\pi/3), \\ x_c &= X_c \cos(\omega t - 4\pi/3), \\ 0 &= x_a + x_b + x_c, \end{aligned} \tag{3.3}$$

where X_a, X_b and X_c are the magnitudes of each component and they are equal, ω is the angular velocity of each axis component in rad/s and $\omega t = \theta$ is the space angle of the defined space vector. The scale sum of the symmetrical three components is 0, which means they have only two degrees of freedom. Then, $\boldsymbol{x} = 2/3(x_a + x_b a + x_c a^2) = (2/3)(3/2)X_a e^{j\omega t} = X_a e^{j\theta} = X e^{j\theta}$. Thus, the magnitude of $\boldsymbol{x}$, X, is equal to the magnitude of each axis component such that the scale factor $\frac{2}{3}$ is adopted. For example, when an arbitrary space angle θ is considered, the resultant vector of the defined space vector is shown in Fig. 3.2 where the red, green, purple and blue line represent the x_a, x_b, x_c and $\boldsymbol{x}$, respectively.

As described in the previous subsection, the space vector resulting from components in $a-b-c$ frame can be expressed in $\alpha-\beta$ frame as well. Its Cartesian form ($\alpha-\beta$ frame) is

$$\boldsymbol{x} = \frac{2}{3}(x_a + x_b \boldsymbol{a} + x_c \boldsymbol{a}^2) = X e^{j\theta} = x_\alpha + j x_\beta = \boldsymbol{x}_{\alpha\beta}, \tag{3.4}$$

where x_α and x_β are respective components in the $\alpha-$ axis and $\beta-$ axis, which can be observed in Fig. 3.2. If $\boldsymbol{a} = e^{j2\pi/3} = \cos(2\pi/3) + \sin(2\pi/3)j = -1/2 + \sqrt{3}/2\text{j}$ and $\boldsymbol{a}^2 = e^{j4\pi/3} = \cos(4\pi/3) + \sin(4\pi/3)j = -1/2 - \sqrt{3}/2j$ are substituted into (3.4), the general transformation

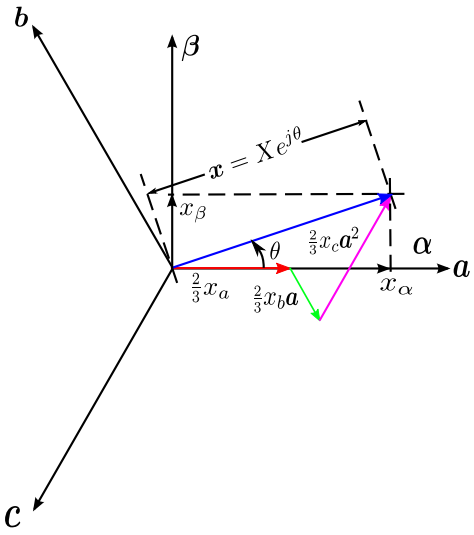

Figure 3.2: Space vector definition.

from $a-b-c$ frame to $\alpha-\beta$ frame can be derived as

$$\begin{aligned} x_\alpha &= \frac{2}{3}(x_a - \frac{1}{2}x_b - \frac{1}{2}x_c), \\ x_\beta &= \frac{2}{3}(0x_a + \frac{\sqrt{3}}{2}x_b - \frac{\sqrt{3}}{2}x_c). \end{aligned} \tag{3.5}$$

Its matrix form is

$$\underbrace{\begin{bmatrix} x_\alpha \\ x_\beta \end{bmatrix}}_{\boldsymbol{x}_{\alpha\beta}} = \underbrace{\frac{2}{3}\begin{bmatrix} 1 & -\frac{1}{2} & -\frac{1}{2} \\ 0 & \frac{\sqrt{3}}{2} & -\frac{\sqrt{3}}{2} \end{bmatrix}}_{\boldsymbol{C}} \underbrace{\begin{bmatrix} x_a \\ x_b \\ x_c \end{bmatrix}}_{\boldsymbol{x}_{abc}}. \tag{3.6}$$

And, the inverse transformation is

$$\begin{bmatrix} x_a \\ x_b \\ x_c \end{bmatrix} = \underbrace{\begin{bmatrix} 1 & 0 \\ -\frac{1}{2} & \frac{\sqrt{3}}{2} \\ -\frac{1}{2} & -\frac{\sqrt{3}}{2} \end{bmatrix}}_{\boldsymbol{C}^{-1}} \begin{bmatrix} x_\alpha \\ x_\beta \end{bmatrix}. \tag{3.7}$$

The aforementioned coordinate transformation theory is called the Clark/inverse Clark transformation. Based on the matrix representation, Clark and inverse Clark transformations can be represented in matrix form by

$$\boldsymbol{x}_{\alpha\beta} = \boldsymbol{C}\boldsymbol{x}_{abc}, \tag{3.8}$$

$$\boldsymbol{x}_{abc} = \boldsymbol{C}^{-1}\boldsymbol{x}_{\alpha\beta}. \tag{3.9}$$

The analyzed transformation is applicable to voltage, current or flux linkage (x can be substituted by u, i and ψ). Note that, the matrix $\boldsymbol{C}^{-1}$ is only a symbol and it does not represent

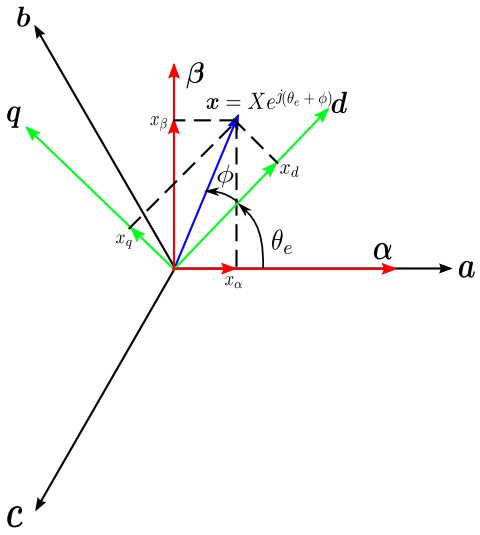

Figure 3.3: Vector transformation from $\alpha - \beta$ to $d - q$ frame.

the inverse matrix of $\boldsymbol{C}$ due to the fact that they are not square matrices. Next, the space vector will be further transformed to $d - q$ frame as indicated in Fig. 3.3 where the space vector is $\boldsymbol{x} = Xe^{j(\theta_e+\phi)}$. Its projections on the $\alpha-\beta$ frame and $d-q$ frame are $\boldsymbol{x}_{\alpha\beta}$ and $\boldsymbol{x}_{dq}$, respectively. According to the trigonometric function theory, they are

$$\begin{aligned} x_\alpha &= X\cos(\theta_e+\phi) = X\cos(\phi)\cos(\theta_e) - X\sin(\phi)\sin(\theta_e) = x_d\cos(\theta_e) - x_q\sin(\theta_e), \\ x_\beta &= X\sin(\theta_e+\phi) = X\sin(\phi)\cos(\theta_e) + X\cos(\phi)\sin(\theta_e) = x_q\cos(\theta_e) + x_d\sin(\theta_e). \end{aligned} \tag{3.10}$$

and in matrix form

$$\begin{bmatrix} x_\alpha \\ x_\beta \end{bmatrix} = \underbrace{\begin{bmatrix} \cos(\theta_e) & \text{-}\sin(\theta_e) \\ \sin(\theta_e) & \cos(\theta_e) \end{bmatrix}}_{\boldsymbol{P} \Rightarrow e^{j\theta_e}} \begin{bmatrix} x_d \\ x_q \end{bmatrix}. \tag{3.11}$$

The inverse transformation is

$$\begin{bmatrix} x_d \\ x_q \end{bmatrix} = \underbrace{\begin{bmatrix} \cos(\theta_e) & \sin(\theta_e) \\ \text{-}\sin(\theta_e) & \cos(\theta_e) \end{bmatrix}}_{\boldsymbol{P^{-1}=P^T} \Rightarrow e^{-j\theta_e}} \begin{bmatrix} x_\alpha \\ x_\beta \end{bmatrix}. \tag{3.12}$$

The transformation from the $\alpha - \beta$ frame to the rotor fixed $d - q$ frame is called Park transformation and is applicable to voltage, current or flux linkage as well. It is clear from (3.11) and (3.12) that the transformation matrix $\boldsymbol{P}$ is an orthogonal matrix, which guarantees a constant power conversion between the two frames. The default angle adopted in $\boldsymbol{P}$ is the rotor electrical angle θ_e, i.e. $\boldsymbol{P} = \boldsymbol{P}(\theta_e)$ without specific definition. Note that, the matrix $\boldsymbol{P}$ behaves equivalently as a rotation factor $e^{j\theta_e}$ in $\alpha - \beta$ Cartesian frame where $\boldsymbol{x}_{\alpha\beta}$ can be expressed as $x_\alpha + jx_\beta$ as well, and therefore, Park and inverse Park transformations can be represented in matrix form by

$$\boldsymbol{x}_{\alpha\beta} = \boldsymbol{P}\boldsymbol{x}_{dq} \Rightarrow x_\alpha + jx_\beta = \boldsymbol{x}_{dq}e^{j\theta_e} = e^{j\theta_e}\boldsymbol{x}_{dq}, \tag{3.13}$$

$$\boldsymbol{x}_{dq} = \boldsymbol{P^{-1}}\boldsymbol{x}_{\alpha\beta} \Rightarrow x_\alpha + jx_\beta = \boldsymbol{x}_{\alpha\beta}e^{-j\theta_e} = e^{-j\theta_e}\boldsymbol{x}_{\alpha\beta}, \tag{3.14}$$

as well. The multiplication sequence of $\boldsymbol{P}/\boldsymbol{P}^{-1}$ and $\boldsymbol{x}_{dq}/\boldsymbol{x}_{\alpha\beta}$ is fixed due to the matrix calculation theory. But in vector form considering $e^{-j\theta}$, the sequence does not matter.

Actually, the Park transformation is applicable to transform an arbitrary quantity from an $\alpha-\beta$ frame to an arbitrary two-axis $x-y$ frame, whose $x-$ axis (like $d-$ axis) has an angle difference equal to θ with the $\alpha-$ axis. As a consequence, the general Park transformation can be realized by

$$\boldsymbol{x}_{\alpha\beta} = \boldsymbol{P}(\theta)\boldsymbol{x}_{xy} \Rightarrow x_\alpha + jx_\beta = \boldsymbol{x}_{xy}e^{j\theta} = e^{j\theta}\boldsymbol{x}_{xy}, \tag{3.15}$$

$$\boldsymbol{x}_{xy} = \boldsymbol{P}^{-1}(\theta)\boldsymbol{x}_{\alpha\beta} \Rightarrow x_\alpha + jx_\beta = \boldsymbol{x}_{\alpha\beta}e^{-j\theta} = e^{-j\theta}\boldsymbol{x}_{\alpha\beta}. \tag{3.16}$$

For instance, if $\theta = \hat{\theta}_e$, the transformation from the $\alpha-\beta$ frame to the estimated $\hat{d}-\hat{q}$ frame is realized. In the following section, a negative sequence frame, in which $\theta = \hat{\theta}_c$, will be introduced. The transformation theory and implementation method are the same as these defined in this subsection.

3.2 Machine fundamental model

3.2.1 Assistant matrix introduction

In order to concisely describe the electrical machine model, vector/matrix equation are adopted in this section. Several assistant matrices are defined in advance to ease the derivation and make the expression uniform.

$$\boldsymbol{I} = \begin{bmatrix} 1 & 0 \\ 0 & 1 \end{bmatrix} \tag{3.17}$$

$$\boldsymbol{J} = \boldsymbol{P}(\theta_e = \frac{\pi}{2}) \begin{bmatrix} 0 & -1 \\ 1 & 0 \end{bmatrix} \tag{3.18}$$

$$\boldsymbol{Q} = \begin{bmatrix} 1 & 0 \\ 0 & -1 \end{bmatrix}. \tag{3.19}$$

$\boldsymbol{I}$ is a identity matrix and does not influence a vector. $\boldsymbol{J}$ is referred to as an orthogonal rotation operator which helps to simplify the derivative of $\boldsymbol{P}$

$$\begin{aligned} \frac{d\boldsymbol{P}}{dt} &= \frac{\partial \boldsymbol{P}}{\partial \theta}\frac{d\theta}{dt} = \boldsymbol{J}\omega\boldsymbol{P} = \omega\boldsymbol{P}\boldsymbol{J}, \\ \frac{d\boldsymbol{P}^{-1}}{dt} &= \frac{\partial \boldsymbol{P}^{-1}}{\partial \theta}\frac{d\theta}{dt} = -\boldsymbol{J}\omega\boldsymbol{P}^{-1} = -\omega\boldsymbol{P}^{-1}\boldsymbol{J}, \end{aligned} \tag{3.20}$$

where $\boldsymbol{P}/\boldsymbol{P}^{-1}$ and $\boldsymbol{J}$ can switch their positions. $\boldsymbol{Q}$ performs a complex conjugation operation and it flips the second component of a vector.

3.2.2 Machine fundamental model in $\alpha-\beta$ frame

According to Kirchhoff's Voltage Law and Faraday's Law of Induction, the stator voltage equation in the $\alpha-\beta$ frame consists of two parts: a resistive voltage drop and a derivative of the

stator flux linkage. It is

$$\boldsymbol{u}_s^s = R_s \boldsymbol{i}_s^s + \frac{d\boldsymbol{\psi}_s^s}{dt}, \tag{3.21}$$

where $\boldsymbol{u}_s^s = [u_\alpha \quad u_\beta]^T$, $\boldsymbol{i}_s^s = [i_\alpha \quad i_\beta]^T$ and $\boldsymbol{\psi}_s^s = [\psi_\alpha \quad \psi_\beta]^T$ are the stator voltage, current and flux in $\alpha - \beta$ frame, respectively. R_s is the stator phase resistance.

The stator flux linkage can be further represented by

$$\boldsymbol{\psi}_s^s = \boldsymbol{L}_s^s \boldsymbol{i}_s^s + \boldsymbol{\psi}_{\text{PM}}^s, \tag{3.22}$$

where

$$\boldsymbol{L}_s^s = \begin{bmatrix} L_\alpha & L_{\alpha\beta} \\ L_{\alpha\beta} & L_\beta \end{bmatrix}, \tag{3.23}$$

$$\boldsymbol{\psi}_{\text{PM}}^s = \boldsymbol{P}\boldsymbol{\psi}_{\text{PM}}^r = \begin{bmatrix} \cos(\theta_e) & \text{-sin}(\theta_e) \\ \sin(\theta_e) & \cos(\theta_e) \end{bmatrix} \begin{bmatrix} \psi_{\text{PM}} \\ 0 \end{bmatrix}. \tag{3.24}$$

To get the inductance relation between $\boldsymbol{L}_s^r$, which is defined in (3.25), and $\boldsymbol{L}_s^s$, (3.22) can be rewritten as (3.26). Both sides of (3.26) are multiplied by $\boldsymbol{P^{-1}}$ to get (3.27)-(3.28).

$$\boldsymbol{L}_s^r = \begin{bmatrix} L_d & 0 \\ 0 & L_q \end{bmatrix}, \tag{3.25}$$

$$\underbrace{\boldsymbol{P}\boldsymbol{\psi}_r^r}_{\boldsymbol{\psi}_s^s} = \boldsymbol{L}_s^s \underbrace{\boldsymbol{P}\boldsymbol{i}_r^r}_{\boldsymbol{i}_s^s} + \underbrace{\boldsymbol{P}\boldsymbol{\psi}_{\text{PM}}^r}_{\boldsymbol{\psi}_{\text{PM}}^s}, \tag{3.26}$$

$$\boldsymbol{\psi}_r^r = \boldsymbol{P^{-1}}\boldsymbol{L}_s^s\boldsymbol{P}\boldsymbol{i}_r^r + \boldsymbol{\psi}_{\text{PM}}^r = \boldsymbol{L}_s^r\boldsymbol{i}_r^r + \boldsymbol{\psi}_{\text{PM}}^r, \tag{3.27}$$

$$\boldsymbol{L}_s^r = \boldsymbol{P^{-1}}\boldsymbol{L}_s^s\boldsymbol{P} \quad \text{or} \quad \boldsymbol{L}_s^s = \boldsymbol{P}\boldsymbol{L}_s^r\boldsymbol{P^{-1}}. \tag{3.28}$$

Based on (3.28) and (3.23), the relation between $\boldsymbol{L}_s^r$ and $\boldsymbol{L}_s^s$ can be further demonstrated in

$$\begin{aligned} L_\alpha &= L_d\cos^2(\theta_e) + L_q\sin^2(\theta_e), \\ L_{\alpha\beta} &= (L_d - L_q)\sin(\theta_e)\cos(\theta_e) = L_{\beta\alpha}, \\ L_\beta &= L_d\sin^2(\theta_e) + L_q\cos^2(\theta_e). \end{aligned} \tag{3.29}$$

If the trigonometric simplification and $L_\Sigma = (L_d + L_q)/2, L_\Delta = (L_d - L_q)/2$ are applied to (3.29), it becomes

$$\begin{aligned} L_\alpha &= L_\Sigma + L_\Delta\cos(2\theta_e), \\ L_{\alpha\beta} &= L_\Delta\sin(2\theta_e) = L_{\beta\alpha}, \\ L_\beta &= L_\Sigma - L_\Delta\cos(2\theta_e). \end{aligned} \tag{3.30}$$

So far, the basic quantities in the $\alpha - \beta$ frame and the inductance relation $\boldsymbol{L}_s^s$ and $\boldsymbol{L}_s^r$ of the machine model have been explained. If $\boldsymbol{L}_s^r$ and ψ_{PM} are assumed to be constants, a linear model

is obtained. Then, the stator voltage equation (3.21) can be further demonstrated as

$$\begin{aligned}\boldsymbol{u}_s^s &= R_s\boldsymbol{i}_s^s + \frac{d\boldsymbol{\psi}_s^s}{dt}\\ &= R_s\boldsymbol{i}_s^s + \frac{d\boldsymbol{L}_s^s\boldsymbol{i}_s^s}{dt} + \frac{d\boldsymbol{\psi}_{\text{PM}}^s}{dt}\\ &= R_s\boldsymbol{i}_s^s + \boldsymbol{L}_s^s\frac{d\boldsymbol{i}_s^s}{dt} + \frac{d\boldsymbol{P}\boldsymbol{\psi}_{\text{PM}}^r}{dt}\\ &= R_s\boldsymbol{i}_s^s + \boldsymbol{L}_s^s\frac{d\boldsymbol{i}_s^s}{dt} + \omega\boldsymbol{J}\boldsymbol{\psi}_{\text{PM}}^s.\end{aligned} \tag{3.31}$$

The electromotive torque produced by the PMSM is the result of the vector product of the stator current $\boldsymbol{i}_s^s$ and the stator flux linkage $\boldsymbol{\psi}_s^s$ in $\alpha-\beta$ frame, and written as

$$T_e = \frac{3}{2}p\boldsymbol{i}_s^{sT}\boldsymbol{J}\boldsymbol{\psi}_s^s = \frac{3}{2}p(\psi_\alpha i_\beta - \psi_\beta i_\alpha), \tag{3.32}$$

where p is the machine pole pairs as defined in Table. 3.1. Note that, the scalar $3/2$ in (3.32) results from the definition of space vector in (3.2) that adopts the $2/3$ as a factor. It must be taken into consideration if energy, power or torque need to be calculated.

The system dynamic behavior including mechanical conditions is described as

$$J_m\frac{d\omega_m}{dt} = T_e - T_m - F_m\omega_m, \tag{3.33}$$

$$\frac{d\theta_m}{dt} = \omega_m, \tag{3.34}$$

where J_m, T_m, F_m, ω_m and θ_m represent the rotor inertia, mechanical load, load torque, mechanical friction coefficient, mechanical rotor speed in rad/s and mechanical rotor position in rad, respectively. The relation between ω_m/θ_m and ω_e/θ_e is $\omega_e = p\omega_m$ or $\theta_e = p\theta_m$.

3.2.3 Machine fundamental model in $d-q$ frame

In analogy to the derivation of the machine model in $\alpha-\beta$ frame, the machine model in the $d-q$ frame can be obtained from (3.21) and shown as in (3.35)

$$\boldsymbol{P}\boldsymbol{u}_s^r = R_s\boldsymbol{P}\boldsymbol{i}_s^r + \frac{d\boldsymbol{P}\boldsymbol{\psi}_s^r}{dt}. \tag{3.35}$$

$$\boldsymbol{u}_s^r = R_s\boldsymbol{i}_s^r + \omega\boldsymbol{J}\boldsymbol{\psi}_s^r + \frac{d\boldsymbol{\psi}_s^r}{dt}, \tag{3.36}$$

$$\boldsymbol{u}_s^r = R_s\boldsymbol{i}_s^r + \omega\boldsymbol{J}\boldsymbol{\psi}_s^r + \boldsymbol{L}_s^r\frac{d\boldsymbol{i}_s^r}{dt}. \tag{3.37}$$

With further derivation, (3.36) and (3.37) can be acquired.

The electromotive torque equation in the $d-q$ frame is derived from (3.32) as well. It can

be rewritten as

$$\begin{aligned} T_e &= \frac{3}{2}p(\boldsymbol{P}\boldsymbol{i}_s^r)^T\boldsymbol{J}\boldsymbol{P}\boldsymbol{\psi}_s^r \\ &= \frac{3}{2}p\boldsymbol{i}_s^{rT}\boldsymbol{J}\boldsymbol{\psi}_s^r \\ &= \frac{3}{2}p(\psi_d i_q - \psi_q i_d) \\ &= \frac{3}{2}p((L_d - L_q)i_d i_q + \psi_{\text{PM}} i_q), \end{aligned} \tag{3.38}$$

where $\psi_d = L_d i_d + \psi_{\text{PM}}$ and $\psi_q = L_q i_q$.

3.3 Multiple-saliency model

In 3.2, the machine fundamental models in both $\alpha - \beta$ frame and $d - q$ frame are introduced. In this section, the HF machine model considering the injection of a rotating HF signal into a PMSM is firstly introduced. And then, the single saliency and multiple- saliency models are derived based on the spacial inductance harmonics. Finally, the demodulation of the rotor position and speed together with the multiple saliencies decoupling method is presented.

3.3.1 Primary saliency model

The notable difference between the fundamental model and the HF model of the PMSM is the dominant component in the machine impedance, which is denoted as $Z = R + j2\pi f_c L$. It is obvious that, when the frequency f_c of the HF signal is higher, $j2\pi f_c L$, the inductive component of the machine impedance, becomes dominant and the input voltage applies mainly to the inductance.

As a result, the HF model of the PMSM can be described as a pure inductive load in equations (3.39-3.40), which is performed in the $\alpha - \beta$ frame, [4] under the following assumptions:

1) The frequency of the HF signal is much higher than the frequency of the fundamental signal, $f_c >> f_e$;

2) The back electromotive force (EMF) and the resistive voltage drop can be neglected compared to the inductance-induced voltage drop in low speed ranges.

$$\boldsymbol{u}_c^s = V_c e^{j\omega_c t} = \boldsymbol{L}_s^s \frac{d\boldsymbol{i}_c^s}{dt}, \tag{3.39}$$

$$\boldsymbol{L}_s^s = \begin{bmatrix} L_\Sigma + L_\Delta\cos(2\theta_e) - L_{dq}\sin(2\theta_e) & L_\Delta\sin(2\theta_e) + L_{dq}\cos(2\theta_e) \\ L_\Delta\sin(2\theta_e) + L_{dq}\cos(2\theta_e) & L_\Sigma - L_\Delta\cos(2\theta_e) + L_{dq}\sin(2\theta_e) \end{bmatrix}, \tag{3.40}$$

$$= L_\Sigma \begin{bmatrix} 1 & 0 \\ 0 & 1 \end{bmatrix} + L_\Delta \underbrace{\begin{bmatrix} \cos(2\theta_e) & \sin(2\theta_e) \\ \sin(2\theta_e) & -\cos(2\theta_e) \end{bmatrix}}_{\text{Primary saliency}} + L_{dq} \underbrace{\begin{bmatrix} -\sin(2\theta_e) & \cos(2\theta_e) \\ \cos(2\theta_e) & \sin(2\theta_e) \end{bmatrix}}_{\text{Cross-saturation}} \tag{3.41}$$

where $\boldsymbol{u}_c^s$ is the HF rotating voltage vector, V_c is the magnitude and ω_c is the rotating speed in rad/s.

Solving equations (3.39-3.40) and considering that there is no cross-saturation ($L_{dq} = 0$), the HF current vector in the stationary reference frame is [4]

$$\boldsymbol{i}_c^s = I_{cp} e^{j(\omega_c t - \pi/2)} + I_{cn} e^{j(-\omega_c t + 2\theta_e - \pi/2)} \tag{3.42}$$

where

$I_{cp} = V_c/\omega_c(L_\Sigma/(L_\Sigma^2 - L_\Delta^2))$, is the magnitude of the Positive-Sequence Current (PSC) depending on the mean transient inductance;

$I_{cn} = V_c/\omega_c(L_\Delta/(L_\Sigma^2 - L_\Delta^2))$, is the magnitude of the Negative-Sequence Current (NSC) depending on the differential transient inductance. The term containing $2\theta_e$ is the primary saliency in the NSC;

$\omega_c = 2\pi f_c = (d\theta_c/dt)$ carrier-signal frequency.

From (3.42), it is seen that the rotor flux angle θ_e is only contained in the NSC component of the excited HF current signal. One successful method to estimate the flux angle from the NSC is to use a demodulator and a PLL estimator [57] as shown in Fig. 3.4.

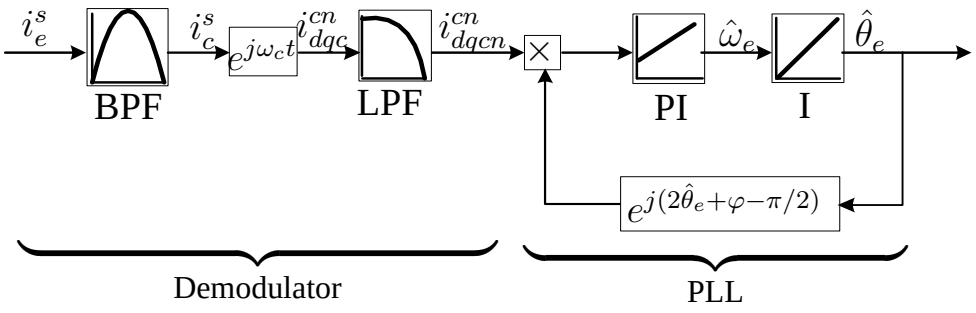

Figure 3.4: Demodulation and PLL.

Firstly, the HF signal is extracted from the measured motor current using a Band Pass Filter (BPF). Then, the NSC is obtained through a LPF after a coordinate transformation. After the demodulator, it is

$$\boldsymbol{i}_{dqcn}^{cn} = I_{cn} e^{j(2\theta_e - \pi/2)} \tag{3.43}$$

Finally, the pure NSC (normally for $2\theta_e$) is used to estimate the rotor flux position and the velocity with the PLL.

3.3.2 Multiple-saliency model

As a matter of fact, the inductance matrix (3.40) contains only the main flux saturation induced primary saliency L_Δ. If machine structure-induced or cross-coupling-induced secondary salien-

cies are considered as well, the inductance matrix (3.40) becomes more complicated (See (13) in [4]) and the resultant HF current can be expressed as

$$\boldsymbol{i}_c^s = I_{cp} e^{j(\omega_c t - \pi/2)} + \sum_h I_{cnh} e^{j(-\omega_c t + h(\theta_e + \varphi_h) - \pi/2)} \tag{3.44}$$

I_{cnh} is the magnitude of h-th component of the NSC;

h is the harmonic number of the saliency causing the h-th component. It is not consecutive and more information can be found in [58] and in the following part;

φ_h is the phase shift of the h-th component relative to the $h\theta_e$ reference frame.

The general inductance model and the HF response current for the rotating HF voltage injection are derived and classified as below for different values of h. For simplicity, $\theta_{eh} = \theta_e + \varphi_h$ is considered.

1) for $h = 1, 4, 7, ...$

$$\boldsymbol{L}_s^s = L_\Sigma \begin{bmatrix} 1 & 0 \\ 0 & 1 \end{bmatrix} + L_{\Delta h} \underbrace{\begin{bmatrix} \cos(h\theta_{eh}) & -\sin(h\theta_{eh}) \\ -\sin(h\theta_{eh}) & -\cos(h\theta_{eh}) \end{bmatrix}}_{\text{Secondary saliency}} \tag{3.45}$$

$$\boldsymbol{i}_c^s = I_{cp} e^{j(\omega_c t - \pi/2)} + I_{cn} e^{j(-\omega_c t - h\theta_{eh} - \pi/2)} \tag{3.46}$$

2) for $h = 2, 5, 8, ...$

$$\boldsymbol{L}_s^s = L_\Sigma \begin{bmatrix} 1 & 0 \\ 0 & 1 \end{bmatrix} + L_{\Delta h} \underbrace{\begin{bmatrix} \cos(h\theta_{eh}) & \sin(h\theta_{eh}) \\ \sin(h\theta_{eh}) & -\cos(h\theta_{eh}) \end{bmatrix}}_{\text{Secondary saliency}} \tag{3.47}$$

$$\boldsymbol{i}_c^s = I_{cp} e^{j(\omega_c t - \pi/2)} + I_{cn} e^{j(-\omega_c t + h\theta_{eh} - \pi/2)} \tag{3.48}$$

3) for $h = 3, 6, 9, ...$

$$\boldsymbol{L}_s^s = L_\Sigma \begin{bmatrix} 1 & 0 \\ 0 & 1 \end{bmatrix} + L_{\Delta h} \cos(h\theta_{eh}) \begin{bmatrix} 1 & 0 \\ 0 & 1 \end{bmatrix} \tag{3.49}$$

$$\boldsymbol{i}_c^s = \frac{V_c}{\omega_c \left(L_\Sigma + L_{\Delta h} \cos(h\theta_{eh})\right)} e^{j(\omega_c t - \pi/2)} \tag{3.50}$$

where

$$L_\Sigma = \frac{\sum_h (L_{dh} + L_{qh})}{2h},$$
$$L_{\Delta h} = \frac{L_{dh} - L_{dh}}{2},$$
$$I_{cp} = \frac{V_c L_\Sigma}{\omega_c \left(L_\Sigma^2 - L_{\Delta h}^2\right)},$$
$$I_{cn} = \frac{V_c L_{\Delta h}}{\omega_c \left(L_\Sigma^2 - L_{\Delta h}^2\right)}.$$

L_{dh}, L_{qh} are the h^{th} spatial inductance harmonics. It is clear that the harmonic order $h = 1, 4, 7, ...$ and $h = 2, 5, 8, ...$ result in NSC signals rotating in the negative direction and positive direction, respectively. In addition, they all contain rotor position information and thus can be utilized to track the rotor position. On the contrary to these two categories, the harmonic orders $h = 3, 6, 9, ...$ do not contribute to any NSC components. Therefore, they can not be relied on to estimate the rotor position.

In the presence of the multiple saliencies, for example, considering two harmonics $h = 2$ and $h = 4$, the HF current is expressed by using (3.46) and (3.48) in

$$\boldsymbol{i}_c^s = I_{cp} e^{j(\omega_c t - \pi/2)} + \boldsymbol{i}_{cn}^s, \tag{3.51}$$

where

$$\boldsymbol{i}_{cn}^s = I_{cn2} e^{j(-\omega_c t + 2\theta_{e2} - \pi/2)} + I_{cn4} e^{j(-\omega_c t - 4\theta_{e4} - \pi/2)}$$
$$I_{cp} = \frac{V_c L_\Sigma}{\omega_c \left(L_\Sigma^2 - L_{\Delta 2}^2 - L_{\Delta 4}^2 - 2L_{\Delta 2} L_{\Delta 4} \cos(6\theta_e + \Delta\varphi)\right)}$$
$$I_{cn2} = \frac{V_c L_{s2}/2}{\omega_c \left(L_\Sigma^2 - L_{\Delta 2}^2 - L_{\Delta 4}^2 - 2L_{\Delta 2} L_{\Delta 4} \cos(6\theta_e + \Delta\varphi)\right)}$$
$$I_{cn4} = \frac{V_c L_{s4}/2}{\omega_c \left(L_\Sigma^2 - L_{\Delta 2}^2 - L_{\Delta 4}^2 - 2L_{\Delta 2} L_{\Delta 4} \cos(6\theta_e + \Delta\varphi)\right)}$$
$$\Delta\varphi = 4\varphi_4 + 2\varphi_2$$

From (3.51), the NSC is composed of a primary saliency signal,I_{cn2}, and a secondary saliency signal, I_{cn4}. Both of them contain rotor position information, which can be decoded by using a PLL or an observer based on either the primary saliency or the secondary saliency. However, the other saliency signal that is not used for estimation will cause estimation error. Thus, problems of how to choose the saliency signal for rotor position estimation and how to decouple or compensate the other saliency signals arise.

3.3.3 Other considerations

The aforementioned derivation of the saliency model neglects the impacts of stator resistance and cross-saturation. In this subsection, their impacts on the position estimation error of the rotating HFI method are analyzed and the relative compensation methods are introduced [4].

3.3.3.1 Resistance impact

If the stator resistance is incorporated in (3.39), it becomes

$$\boldsymbol{u}_c^s = V_c e^{j\omega_c t} = R_s \boldsymbol{i}_c^s + \boldsymbol{L}_s^s \frac{d\boldsymbol{i}_c^s}{dt}. \tag{3.52}$$

Thus, the resulting HF current, considering no cross-saturation, becomes

$$\boldsymbol{i}_c^s = I_{cp} e^{j(\omega_c t + \varphi_{Rp})} + I_{cn} e^{j(-\omega_c t + 2\theta_e + \varphi_{Rn})} \tag{3.53}$$

where

$$\begin{aligned}
\varphi_{Rp} &= \text{atan}((-\omega_c L_d + L_q)/R_s) - \text{atan}(\omega_c L_d/R_s) - \text{atan}(\omega_c L_q/R_s), \\
\varphi_{Rn} &= \pi/2 - \text{atan}(\omega_c L_d/R_s) - \text{atan}(\omega_c L_q/R_s).
\end{aligned}$$

If the PLL is adopted to extract the rotor position, the estimation error is

$$\begin{aligned}
\epsilon &= \boldsymbol{i}_{cn}^{cn} \otimes e^{j(2\hat{\theta}_e - \pi/2)} \\
&\approx I_{cn}(2(\theta_e - \hat{\theta}_e) + \varphi_{Rn} - \pi/2) \approx 0,
\end{aligned} \tag{3.54}$$

and the resistance-induced estimation error is

$$\theta_e - \hat{\theta}_e = -1/2(\varphi_{Rn} - \pi/2) = 1/2(\text{atan}(\omega_c L_d/R_s) + \text{atan}(\omega_c L_q/R_s)). \tag{3.55}$$

It is clear from (3.55) that neglecting the stator resistance brings an additional constant estimation error to the PLL based tracking scheme. The error can be compensated for by adding a constant value to the estimated position with the assumption that the parameters L_d, L_q and R_s remain constants. In order to further compensate the error adaptively, a Look-up Table (LUT) should be built to include the variation of parameters with the operation point.

3.3.3.2 Cross-saturation and secondary saliency impact

The cross-saturation results from a load-dependent rotor flux displacement and can be expressed as L_{dq} in (3.41). Comparing the cross-saturation term in (3.41) with the secondary saliency term in (3.45), it can be deduced that the cross-saturation actually behaves as a special case of a secondary saliency. For instance, if L_{dq} and $2\theta_e$ in cross-saturation are replaced by $L_{\Delta h}$ and $h\theta_{eh}(\varphi_h = -\pi/2)$, respectively, the cross-saturation term in (3.41) becomes the secondary saliency term in (3.45).

As a consequence, the impact of the secondary saliency on the estimation error is similar to that of the cross-saturation. Assuming the PLL is adopted to extract the rotor position as well, the estimation error is

$$\begin{aligned}
\epsilon &= \boldsymbol{i}_{cn}^{cn} \otimes e^{j(2\hat{\theta}_e - \pi/2)} \\
&= (I_{cn2} e^{j(2\theta_e - \pi/2)} + I_{cnh} e^{j(h\theta_e - \pi/2 + \Delta\varphi)}) \otimes e^{j}(2\hat{\theta}_e - \pi/2) \\
&= I_{cn}\text{sin}(2(\theta_e - \hat{\theta}_e)) + I_{cnh}\text{sin}(h\theta_e - 2\hat{\theta}_e + \Delta\varphi)) \approx 0,
\end{aligned} \tag{3.56}$$

and then, the cross-saturation and secondary saliency-induced estimation error is

$$\theta_e - \hat{\theta}_e = -\frac{1}{2}\text{arcsin}(\frac{I_{cnh}}{I_{cn2}}\text{sin}(h\theta_e - 2\hat{\theta}_e + \Delta\varphi)). \tag{3.57}$$

Similar to the compensation of the resistance-induced rotor position estimation error, the cross-saturation and secondary saliency-induced rotor position estimation errors can be compensated by deriving the model of the secondary saliency, which can be obtained through commissioning tests. In another way, the cross-saturation and secondary saliency can be decoupled before they are fed to the PLL, which will be discussed in detail in Ch. 5.

3.4 Summary

In this chapter, the basic symbol definition, machine fundamental model and saliency model are introduced in detail, which is the mathematical basis of the whole work. Moreover, the impacts of resistance and cross-saturation on position estimation error are considered as well to give a comprehensive overview of the saliency based rotating HF signal injection method.

CHAPTER 4

Testbench and implementation

In this chapter, the used testbench, on which all the experiments are performed, and its related software and hardware design are introduced.

In general, there are two popular controllers in motion control systems: Field Programmable Gate Array (FPGA) and Digital Signal Processor (DSP). The FPGA-based controller has the advantages of parallel calculation and fast sampling ability. However, it utilizes the fixed-point data and Very High Speed Integrated Circuit Hardware Description Language (VHDL) for programming, which are more difficult to manually realize in practice compared with the DSP-based controller using floating point C language. The DSP-based controller has the limit of sampling frequency, and thus, it can not be applied to such application where fast switching frequency (e.g.,$>$100kHz) is required.

In the used testbench, both FPGA and Central Processing Unit (CPU), which is the core processor of a normal computer and behaves like a DSP, are adopted as controllers. They cooperate with each other to implement complex algorithms. This framework maintains the advantages of both controllers while avoiding their disadvantages at the same time. Several key modules inside the FPGA and software implementations for both controllers are presented in this chapter.

4.1 Testbench introduction

The real time system consists of a CPU (Core 2 Duo), an FPGA (Cyclone 3) and a Complex Programmable Logic Device (CPLD), which is shown in Fig. 4.1.

The CPU is in charge of the configuration of the FPGA and the implementation of key algorithms on account of its fast execution of floating-point data operations. In comparison with the core-processor CPU, the FPGA is the coprocessor and responsible for the sampling and preprocessing of input signals and the shaping and verifying of output signals. For example, the configuration and control of the peripheral devices (e.g., A/D, D/A, Resolver etc.) are han-

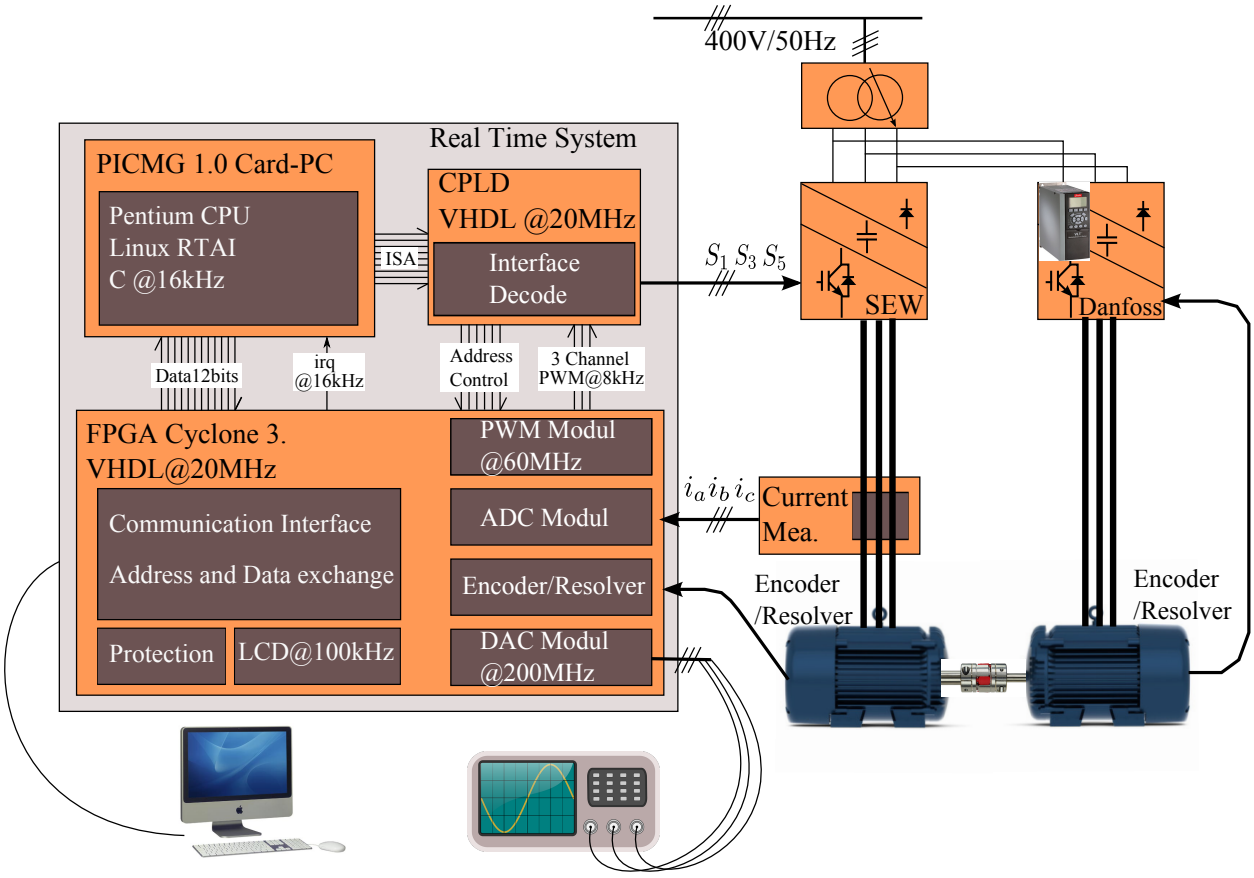

Figure 4.1: Hardware setup.

dled by the FPGA. The FPGA has not only the advantage of parallel calculation but also the flexibility of executing modules with different excitation clocks. A 16kHz interrupt signal (irq) is generated by the FPGA and fed to the CPU. The CPLD is a medium device between the CPU and the FPGA. It decodes the control signals sent by the CPU and makes an interface for the path of the PWM signals. These are the default configurations for the real time system but they can be flexibly changed according to different application requirements. For instance, the FPGA alone can replace the CPU and work as the core-processor as well. Whether the FPGA or CPU is used as the core-processor to execute complex calculation depends highly on the application.

It can be seen from Fig. 4.1 that there are 7 modules inside the FPGA but they run with 4 different clocks (default clock is 20MHz), which is helpful for the compatibility of devices requiring different excitations. The 4 clocks are generated by the Phase-Locked-loop module of FPGA itself and connected to individual module in the main function. The communication module runs at 20MHz and it can synchronize all modules to guarantee the effective data exchange between the CPU and the FPGA. The other modules and their functions are listed in Table. 4.1 where the abbreviations of SVPWM, SPWM, DSC and LVDS denote Space Vector PWM, Sinusoidal PWM, Direct Switch Control (for DTC and PTC method) and Low Voltage Differential Signaling, respectively.

Module	*Clock*	*Input*	*Output*	*Remark*
PWM module	60MHz	Reference $u^*_{a,b,c}$	PWM$_{a,b,c}$	SVPWM,SPWM,DSC
ADC module	20MHz	LVDS $i_{a,b,c}$	Digital $i_{a,b,c}$	12Bits,unsigned
Encoder/Resolver	20MHz	Pulse/Analog signals	Digital θ_e, ω_e	12Bits,unsigned
DAC module	200MHz	Digital X	Analog X	Range:+-10V
LCD module	100kHz	Digital Info.	LCD Info.	System condition display
Protection	20MHz	Digital $i_{a,b,c}$	Enable/Disable PWM	Over-current protection
Communication.	20MHz	From CPU or FPGA	To FPGA or CPU	Data exchange

Table 4.1: Functions of the modules inside the FPGA.

In spite the fact that most of the hardware and software has already been developed by other colleagues, improvements in two aspects are still expected. Firstly, a resolver demodulation and an SVPWM sub-module are developed to further enhance the system flexibility. The necessity and internal structure are presented in the following sections. Secondly, although the implementation of the algorithm is done in the CPU as a default setting, it is also flexible to move the core-algorithm calculation into the FPGA. Consequently, the Matlab/Simulink based C code and VHDL code generation will be introduced to relieve the programming effort in both situations.

4.2 Space vector PWM implementation

PWM technology is widely adopted in machine control systems based on Voltage Source Inverters (VSI). Among these PWM technologies, there are two popular types: Sinusoidal PWM and Space Vector PWM.

SPWM is a popular technology, which utilizes the comparison of a sinusoidal modulation signal and a triangle carrier signal to generate the PWM signals. Its algorithm is simple and thus easy to realize. Nevertheless, it only uses 78.55% capacity of the DC link voltage and needs some compensation methods to improve this ratio. Compared to SPWM, SVPWM is a promising alternative. It can reach 90.7% efficiency of the DC link voltage and meanwhile reduce voltage and current harmonics obviously by using a symmetrical waveform of the PWM. However, the implementation of SVPWM is complex in comparison with SPWM.

The existing PWM top-module in the FPGA contains an SPWM generator and a DSC generator which is invented exclusively for the DTC or PTC methods. Certainly, the implementation of SVPWM in the CPU is possible and the merit is the super capability of the CPU in handling complex algorithm calculations. But, the sampling frequency of the CPU is limited and it processes data sequentially, which leads to a slower cycling period of the PWM signal. On the contrary, the FPGA that deals with parallel data calculation can adopt a much more higher sampling frequency than the CPU. As a result, the development of an SVPWM generator based on an FPGA is necessary to further improve the performance and flexibility of the used real time system. On the one hand, if the CPU is the core processor, the design relieves the calculation burden for the CPU. On the other hand, the design makes the FPGA totally independent from the CPU and the FPGA can work as the core processor. In this case, all control algorithms including input and output signals are handled by the single FPGA.

However, compared to SPWM that needs only a simple comparison calculation to generate

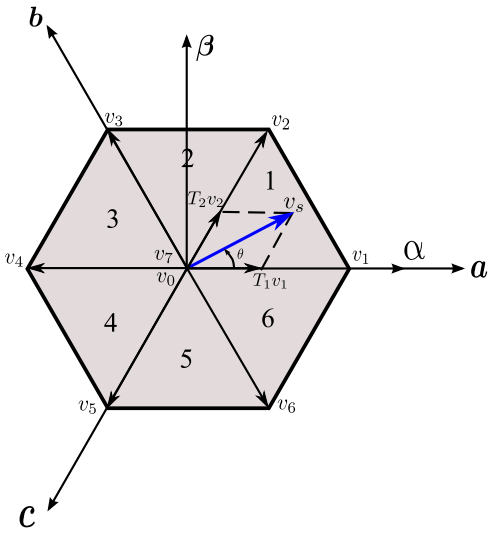

Figure 4.2: SVPWM implementation.

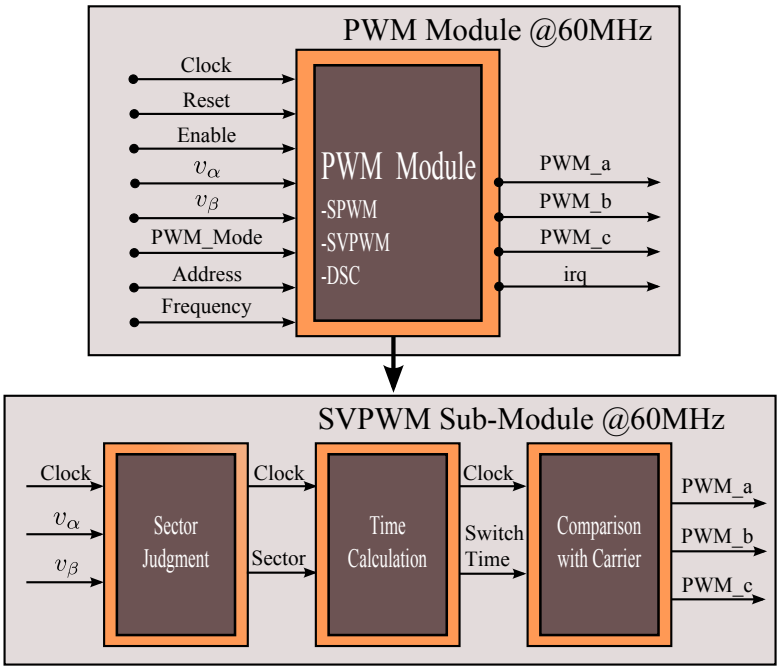

Figure 4.3: PWM module and SVPWM sub-module in FPGA.

PWM signals, the SVPWM generator requires more computation effort, for instance, the duration time for applied adjacent vectors to synthesize the reference vector ($T_1v_1 + T_2v_2 = v_sT_s$) as shown in Fig. 4.2. In addition, the judgment of the sector location of the reference vector is needed. Hence, the obvious difficulties of SVPWM implementation in the FPGA are the data processing including math calculation and logic execution.

The overview of the PWM top-module and its SVPWM sub-module are described in Fig. 4.3. Among the input signals, the v_α v_β are the references generated by the CPU or other modules of the FPGA. The “PWM_Mode” is an option switch for choosing SPWM, SVPWM or DSC .

The “Frequency” is an option to set the PWM frequency. The rest signals of the inputs are other configurations for synchronization the PWM module with other parallel modules. The output signals of the PWM module are three PWM signals and an interrupt ‘irq’ for the CPU, which is fed back to the CPU as a sampling clock and guarantees the synchronization between the CPU and the FPGA at the same time.

4.3 Resolver demodulation

In most electrical drive systems, the rotor position/speed is measured by an encoder or a resolver. The encoder is a simple coding device and it outputs pulse signals according to the rotor position/speed without any excitation signals except a single power supply. It is cheaper and has lower accuracy in comparison with a resolver. The resolver, however, needs sine/cosine excitation signals (specific voltage and frequency range) and it outputs sine/cosine signals as well which require a special device or program to decode. After decoding, the digital rotor position/speed signal can be obtained and used by a digital controller.

In our existing real time system, only an encoder demodulation module is developed inside the FPGA. It is not enough to decode position/speed signals from a resolver which is usually a default device equipped together with a high-performance servo-motor. As a consequence, the corresponding resolver demodulation module in the FPGA and its related decode circuit are developed considering the system compatibility, which is necessary to enhance the system flexibility. A decode device AD2S1210 is chosen because of its flexibility of output format, configuration range and interface standard. It has also the ability of fault diagnosis and selection of precision level of decoded position and speed signals. In addition, it can emulate the encoder signals for the adaptation of different controller interfaces.

The resolver decode schematic diagram and PCB are demonstrated in Fig. 4.4 and Fig. 4.5, respectively. The overview of the main function of AD2S1210 and its implementation are illustrated in these figures. The decode circuit is located between the resolver module of the FPGA and the position sensor integrated with the tested machine, which is not shown in Fig. 4.1. The configuration and control of the AD2S1210 are done by the resolver module inside the FPGA, and meanwhile, the serial digital signals of speed/position and the corresponding diagnosis signals are fed back to the resolver module of the FPGA for formatting and ratio adaptation. After processing, the converted 12 bit parallel unsigned speed/position signals are transferred from the FPGA to the CPU for the implementation of control algorithms, which is the default way for data communication.

Obviously, the converted speed/position signals can be handled by the FPGA itself as well when it is chosen as the core-processor. In this case, the CPU runs as a coprocessor and only monitors the system conditions and gives reference instructions. Naturally, the data transfer of speed/position as well as three phase sampled currents from the FPGA to the CPU become unnecessary. This kind of development of control systems will be discussed later.

The AD2S1210 has different operation modes and interface options for both inputs and outputs so as to adapt different speed/position resolvers (excitation frequency range from 2kHz to 20kHz) and different data formats (parallel or serial, 10-16bit). The settings of these modes and interfaces are set through register configurations of the AD2S1210, which can be conveniently done by the FPGA at the initialization procedure.

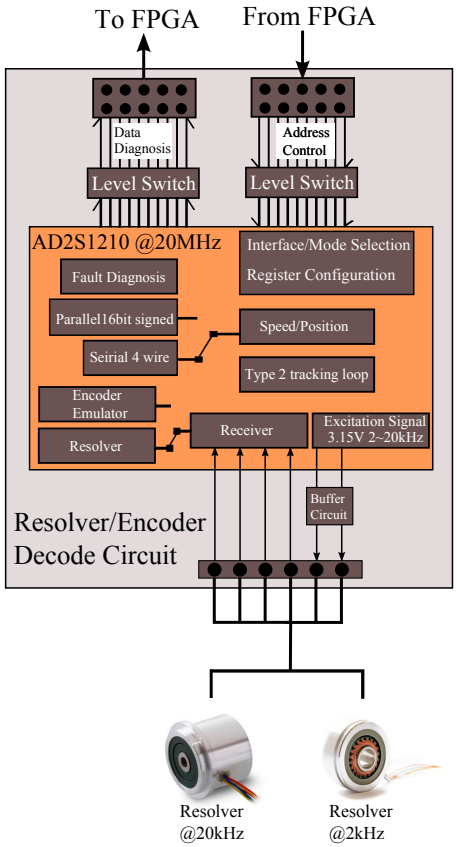

Figure 4.4: Resolver decode schematic diagram.

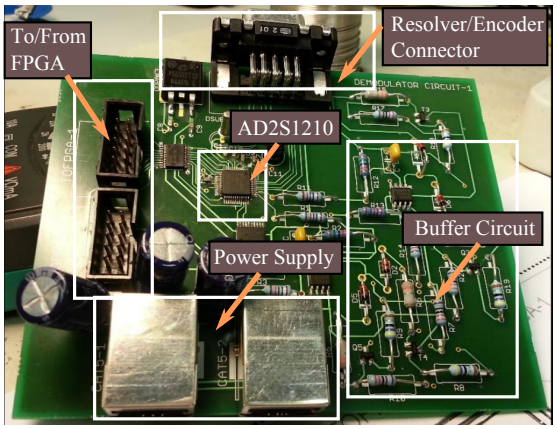

Figure 4.5: Resolver decode circuit PCB.

4.4 C code generation through Matlab/Simulink

The executable code in the CPU or other types of DSP is a standard C code. Normally, it is required to program the C code manually, which is a time-consuming work and the debugging work may last even longer than the programming work. In recent years, the software Matlab®/Simulink® was promoting a model based C code generation tool. It is powerful and

becoming more and more popular in the development of complex algorithms for industrial applications. dSPACE® product is a successful example based on Matlab®/Simulink®. It provides a seamless connection between the Matlab/Simulink model and executable codes both for the DSP and the FPGA. It is convenient to design and test any control algorithm based on Hardware-In the Loop (HIL) of dSPACE®. Nevertheless, the cost of a dSPACE® product is much higher than the used real time system. The concept of C code generation through Matlab®/Simulink®, fortunately, is still applicable to our real time system. The corresponding toolbox in Matlab®/Simulink® is called *Matlab Coder*, which is utilized in this section.

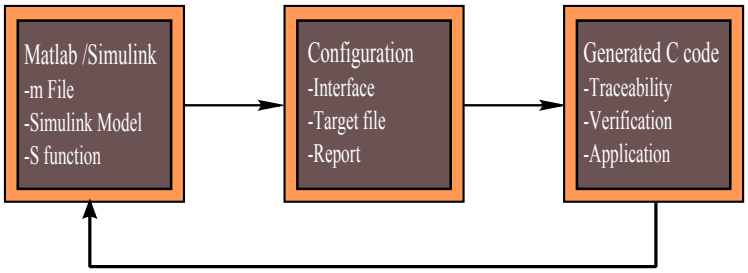

Figure 4.6: C code generation procedures.

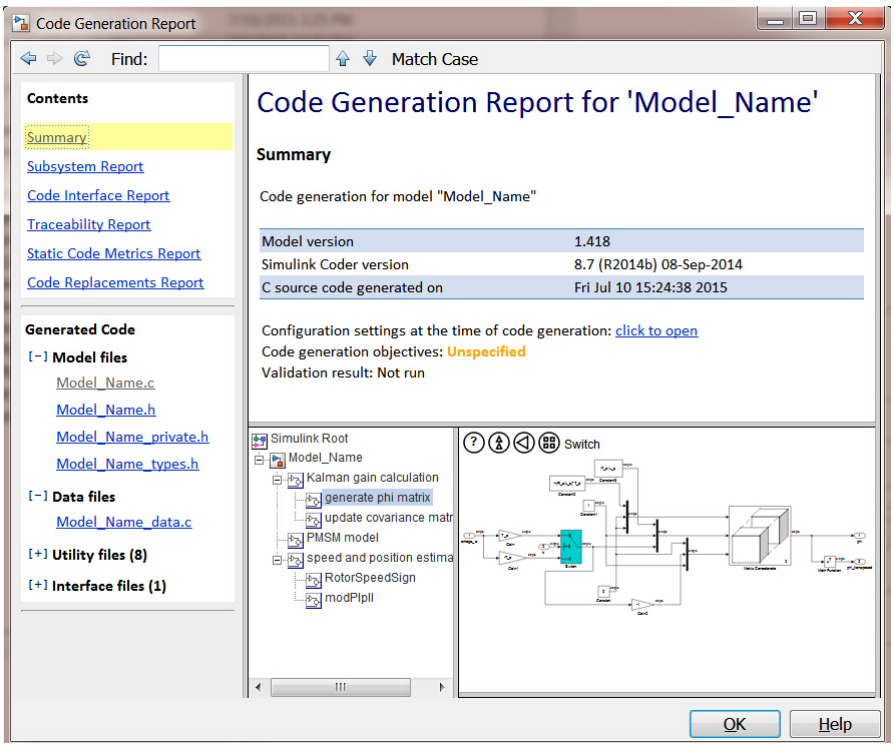

Figure 4.7: Generation report.

The development procedures for C code generation are illustrated in Fig. 4.6. There are 3 steps: modeling, configuration and generation of C code. Firstly, the Matlab model containing the *m file, s-function or Simulink model* should be completed and simulated off-line successfully. The model is the objective that we want to translate to C code. Secondly, corresponding general

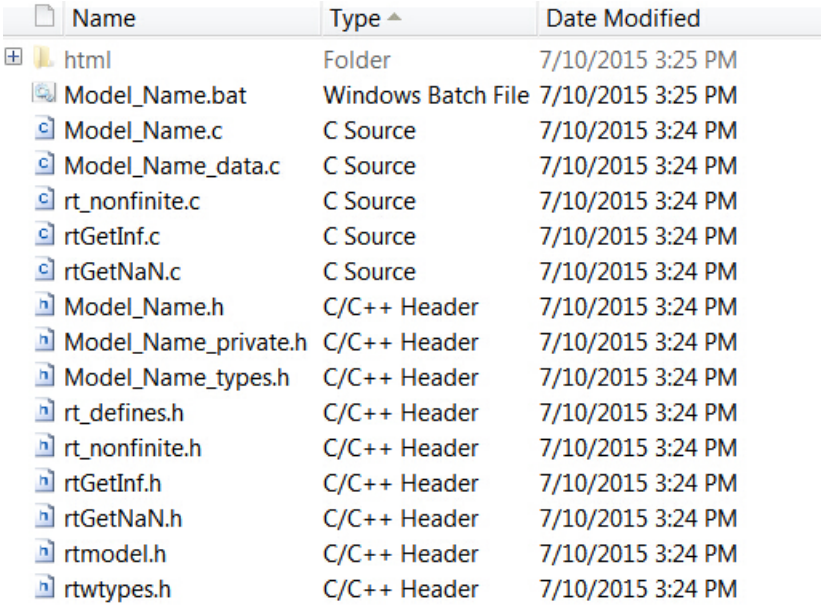

Name	Type	Date Modified
html	Folder	7/10/2015 3:25 PM
Model_Name.bat	Windows Batch File	7/10/2015 3:25 PM
Model_Name.c	C Source	7/10/2015 3:24 PM
Model_Name_data.c	C Source	7/10/2015 3:24 PM
rt_nonfinite.c	C Source	7/10/2015 3:24 PM
rtGetInf.c	C Source	7/10/2015 3:24 PM
rtGetNaN.c	C Source	7/10/2015 3:24 PM
Model_Name.h	C/C++ Header	7/10/2015 3:24 PM
Model_Name_private.h	C/C++ Header	7/10/2015 3:24 PM
Model_Name_types.h	C/C++ Header	7/10/2015 3:24 PM
rt_defines.h	C/C++ Header	7/10/2015 3:24 PM
rt_nonfinite.h	C/C++ Header	7/10/2015 3:24 PM
rtGetInf.h	C/C++ Header	7/10/2015 3:24 PM
rtGetNaN.h	C/C++ Header	7/10/2015 3:24 PM
rtmodel.h	C/C++ Header	7/10/2015 3:24 PM
rtwtypes.h	C/C++ Header	7/10/2015 3:24 PM

Figure 4.8: Generated file list.

and specific settings should be made through the configuration window of the *Matlab Coder*. For example, the objective language, C or C++, the symbol definition rules, input and output signal settings are configured in this procedure. Note that, the report option should be chosen so as to have the bi-directional traceability (between the model and the C code). In addition, the comment option is recommended on account of that it can ease the understanding of the generated C code. Finally, the anticipated C code of the appointed model is generated in a specific path (*Model_Name_ert_rtw*) after clicking the generation button.

When the C code generation procedure has finished, a window called "Code Generation Report" pops up as expected, which is demonstrated in Fig. 4.7. It gives an overview of the generated code including a subsystem report, code interface report, traceability report etc.. It is convenient to find all useful information here and helps to understand the structure of the generated files.

The generated C code files are shown in Fig. 4.8, in which there are 9 header files (*.h*) and 5 source files (*.c*). The most important files are explained below.

The source file *Model_Name.c* is the main file and it refers to the objective model in Matlab®/Simulink®. Inside the *Model_Name.c*, there are two main functions: *Model_Name_step* and *Model_Name_initialize*. If it is needed, other functions like trigonometric functions would be included in *Model_Name.c* as well and they can be called by the *Model_Name_step*. The *Model_Name_step* function is called once each sampling period by the controller and all algorithms are executed in it. More detailed information of its implementation can be acquired through the traceability function. *Model_Name_initialize* contains the definitions of variables and default action when there is an error.

The source file *Model_Name_data.c* includes all adjustable parameters used in *Model_Name_step* e.g., PI parameters, delay time constant, saturation value, initial value of some matrix and etc.. Other .c files and corresponding .h files are generated by system default and they handle the errors.

The header file *Model_Name_private.h* includes the definitions of input and output signals. They need to be modified according to the existing C project, in which you want to merge the generated C code. Another header file *Model_Name_types.h* gives definitions of all variable types. The rest two .h files *rtwtypes.h* and *rtmodel.h* are system files and can be ignored.

The functions of several important generated files are explained. Next, it is convenient to merge the generated files into any existing C project. In practice, several fundamental model based sensorless observers for PMSM have been developed successfully by using the C code generation.

4.5 VHDL code generation through Matlab/Simulink

As introduced before, there are two kinds of controllers which are popular in drive control system: DSP based and FPGA based. The former one adopts C or C++ as a programming language. In the case of the FPGA based controller, programming in VHDL or Verilog is necessary. Fortunately, the VHDL or Verilog code generation toolbox and its related verification toolbox were already released by Matlab®/Simulink® as well (*HDL coder* and *HDL verifier*). Consequently, the programming burden of VHDL or Verilog can be lightened greatly. In this section, several key points for *HDL coder* and *HDL verifier* are introduced and explained.

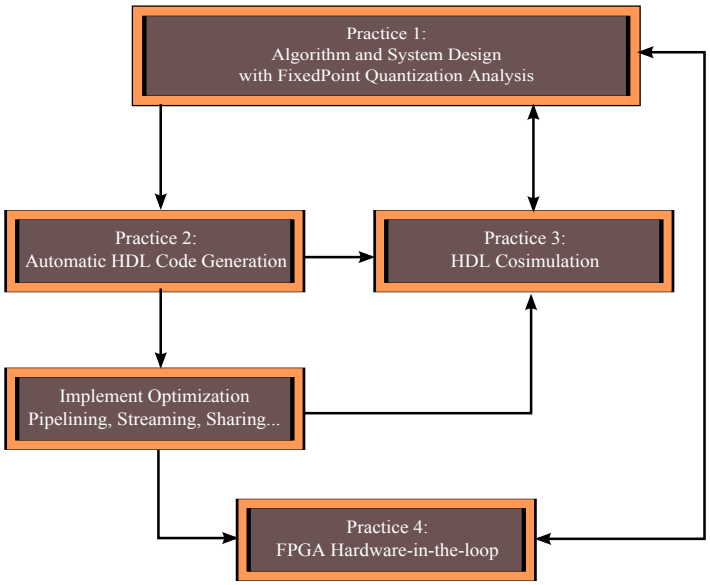

Figure 4.9: VHDL code generation procedures.

The development procedures of VHDL code generation are illustrated in Fig. 4.9. The first step is modeling and simulation according to the requirements of any controller based on floating point data. And then, a toolbox named *Fixed Point Tool* shown in Fig. 4.10 is utilized to convert the floating point model to an optimized fixed point model. The second step is generating a readable, traceable VHDL or Verilog code for the FPGA. The generation report is shown in Fig. 4.11 that is similar with the one for C code generation. It is helpful for users to understand the generated VHDL code by means of the function of bi-directional traceability. Note that, there is a *High-Level Resource Report* in the pop-window and it gives the resource

utilization including multipliers, adders, registers and multiplexers. According to the utilization and the FPGA capacity, the optimization should be performed (e.g., pipe-lining, streaming, sharing etc.). After the appropriate optimization, a Matlab-Modelsim®/Questa®/Cadence® co-simulation can be generated in the third step. A general overview of this function can be found in Fig. 4.12. The co-simulation is an effective verification tool to validate if the function of generated VHDL code is exactly the same as the original Matlab model. Finally, the FPGA hardware-in-the-loop simulation shown in Fig. 4.13 can further verify the effectivenss of the generated VHDL code. If the VHDL code passes these tests, it is ready for use.

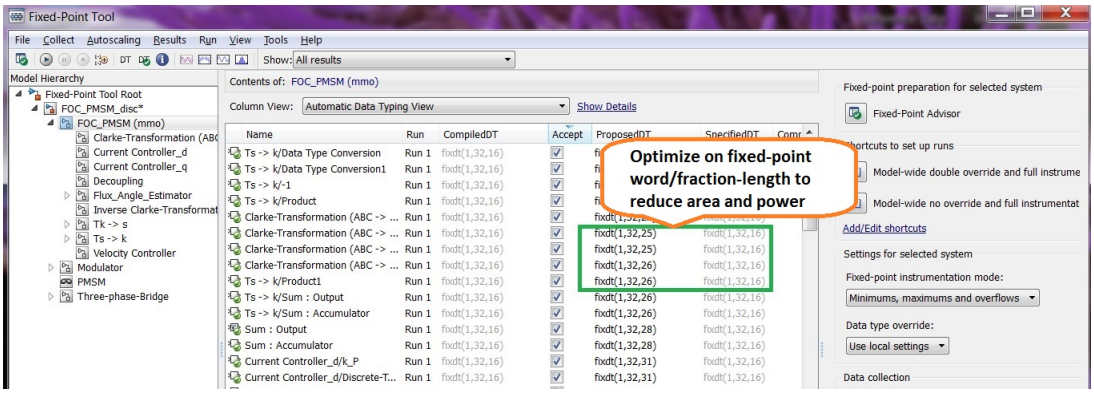

Figure 4.10: Optimization through *Fixed Point Tool*.

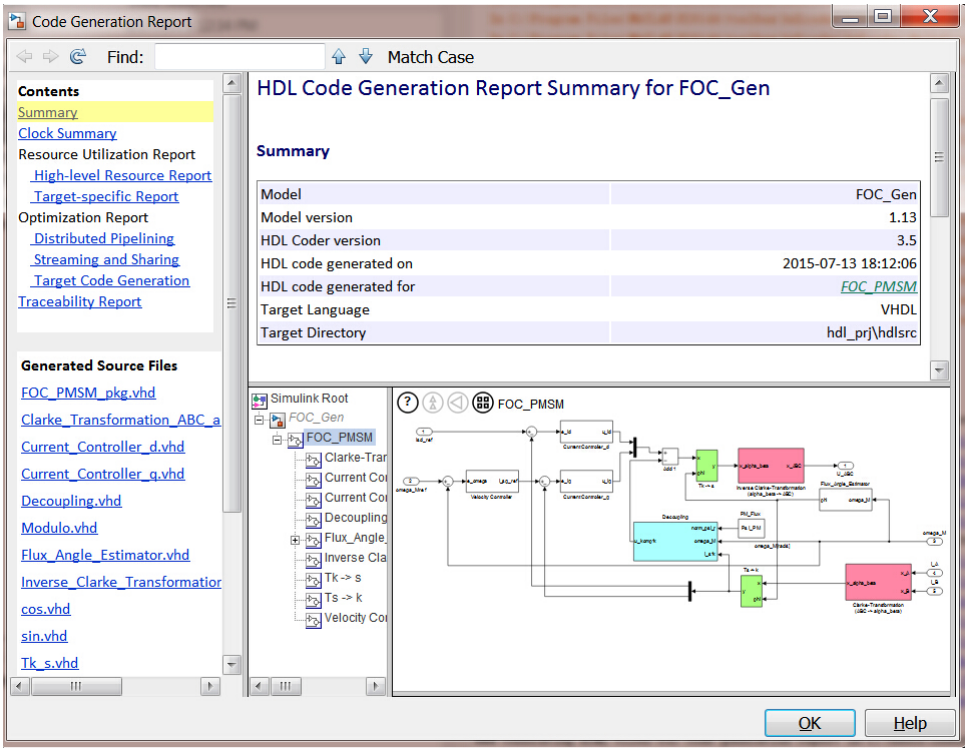

Figure 4.11: VHDL generation report.

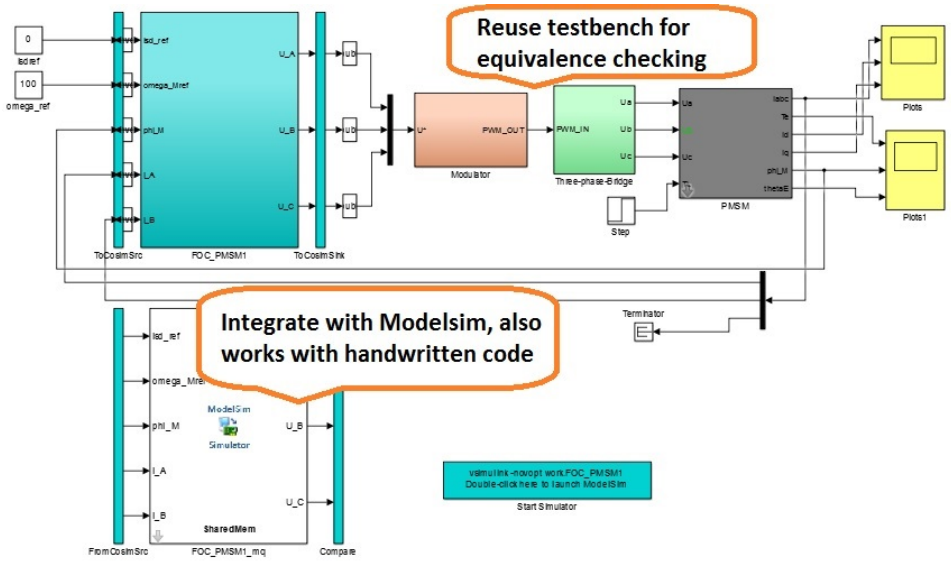

Figure 4.12: Matlab-ModelSim co-simulation.

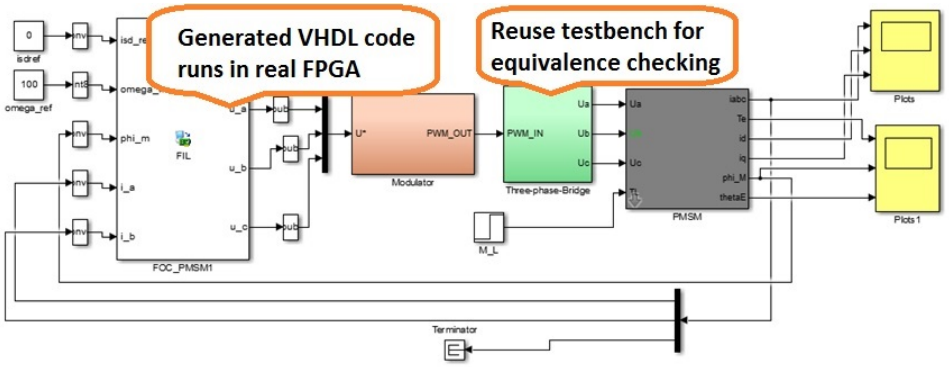

Figure 4.13: FPGA in the loop co-simulation.

In this section, VHDL generation is introduced briefly, which is helpful for designing any new algorithms based on an FPGA. In practice, the basic FOC controller for PMSM has been developed successfully by using the VHDL code generation. However, the performance is not so good as the CPU based controller due to the difficulty of debugging work. As a result, in all the experiments in following chapters, the CPU is still the core-processor.

4.6 Summary

In this chapter, the testbench used for verifying all proposed algorithms is introduced briefly. Two improvements inside the FPGA, SVPWM sub-module and resolver demodulation, are developed, which makes the testbench more flexible to adapt for more application areas. Moreover, two popular code generation methods based on Matlab®/Simulink® are introduced and applied to the existing controller for both CPU and FPGA. These tools can accelerate the de-

velopment of any complex algorithm, whether with a CPU or an FPGA, and save time for code debugging.

CHAPTER 5

Saliency tracking based sensorless method

This chapter deals with the sensorless control based on the saliency tracking method, which is good at the low speed and standstill sensorless control. However, the most difficult problem of sensorless control for cwSPMSM is its strong multiple saliencies. Thus, three individual methods from different perspectives are proposed in this chapter to solve the problem.

Firstly, a Multi-Signal Injection (MSI) method is proposed to combine two sets of saliency signals and synthesize a virtual saliency signal, based on which the sensorless control is performed. Secondly, on the contrary to utilizing both saliency signals, a Secondary Saliency Tracking (SST) method is proposed where only the secondary saliency signal is extracted taking advantage of the rotation difference between saliency signals of different orders, and of an Adaptive Notch Filter (ANF). Moreover, the corresponding initial position estimation is implemented. Finally, a Repetitive Control (RC) method is brought into the PLL loop for decoupling of the secondary saliency and the traditional primary saliency tracking is realized again. All these three sensorless methods are verified by experimental tests and show satisfactory performance.

5.1 Background

5.1.1 Sensorless control based on the HF signal injection

Fig. 5.1 gives the structure of a sensorless FOC system for a PMSM using the rotating HF signal injection method [37]. The input is the speed command ω_{ref}. The HF voltage u_c^s is superimposed on the fundamental component u_e^s in the stationary reference frame. There are two control loops: a fundamental current control loop and a speed control loop. The fundamental current i_e^s is obtained through a LPF, because the measured phase current i^s includes both fundamental and HF carrier components. The rotor position and speed, which are normally measured by an encoder, are calculated by a demodulator and a PLL estimator using the measured motor currents i^s. The estimated rotor position $\hat{\theta}_e$ and speed $\hat{\omega}_e$ are fed back to the regulator.

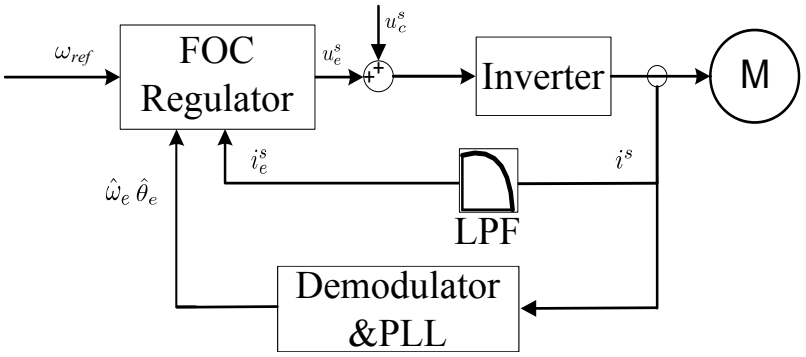

Figure 5.1: Sensorless control system using the HF signal injection method.

The demodulation and PLL parts have been introduced in Fig. 3.4. In the following methods, they all adopt FOC control and the PLL technique to estimate the rotor position and speed.

5.1.2 Saliency behavior of the tested cwSPMSM

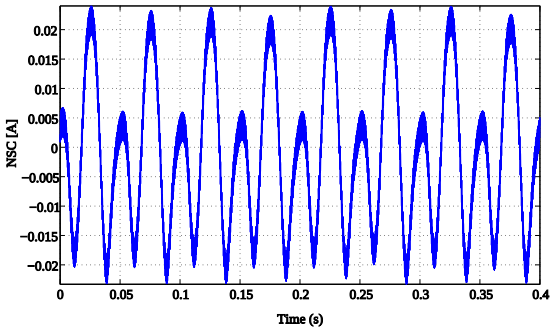

(a) Waveform of NSC with normal BPF.

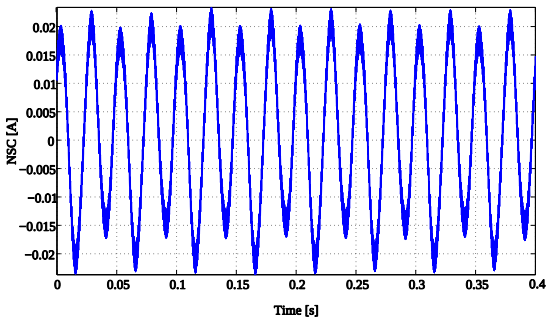

(b) Waveform of NSC with proposed BPF.

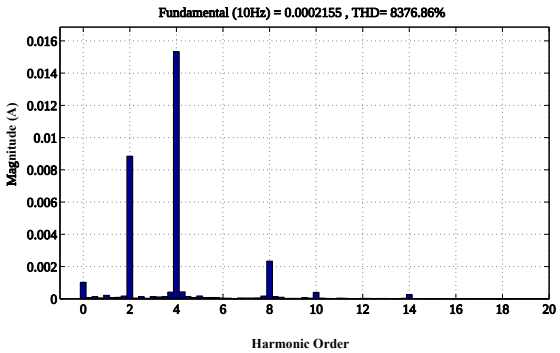

(c) FFT analysis of NSC with normal BPF.

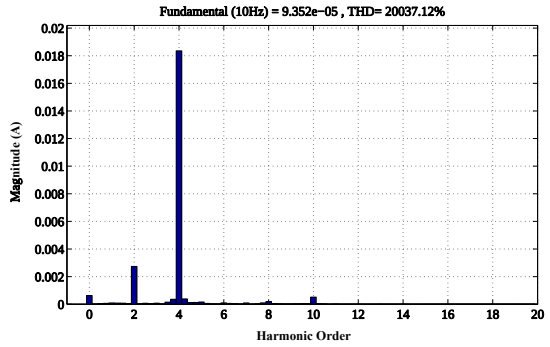

(d) FFT analysis of NSC with proposed BPF.

Figure 5.2: Waveforms of NSC and their FFT Analysis (1kHz 35V), left: (normal BPF), right: (proposed BPF).

As an example to demonstrate the phenomenon of multiple saliencies, a cwSPMSM is taken into consideration. The results of using the rotating HF signal (1kHz 35V) injection method are shown in Fig. 5.2. Fig. 5.2(a) gives the waveform of the NSC i_{dqcn}^{cn} extracted through a normal BPF in the demodulator, which has a bandwidth of [0.9kHz 1.1kHz] with 1kHz in the middle. The design can extract all effective saliency signals from the measured current signal regardless of their rotation directions. Fig. 5.2(c) is the Fast Fourier Transformation (FFT) analysis result of Fig. 5.2(a). Fig. 5.2(b) and Fig. 5.2(d) are corresponding results obtained through a specially designed BPF, which will be explained in 5.3.

It can be observed from Fig. 5.2(c) that the machine reveals different orders of saliency $h = 2, 4, 8$, among which the magnitude I_{cn8} of $h_8 = 8$ has a poor SNR and can be neglected. So based on the multiple saliencies model (3.44), the NSC response for cwSPMSM can be expressed as (5.1) according to its FFT analysis

$$\begin{aligned} i_c^s =& I_{cp}(\omega_c)e^{j(\omega_c t-\pi/2)} + I_{cn2}(\omega_c)e^{j(-\omega_c t+2\theta_e+\varphi_2-\pi/2)}+ \\ & I_{cn4}(\omega_c)e^{j(-\omega_c t-4\theta_e+\varphi_4-\pi/2)}. \end{aligned} \tag{5.1}$$

Note that, since the 4-th order frequency component rotates in the opposite direction as the second order component, it is marked with a minus symbol [59].

5.1.3 Challenges of strong multiple saliencies

As described in (3.42) and (3.44): $2\theta_e$ and $h\theta_e(h \neq 2)$ are general primary and secondary saliencies, respectively. And the saliency ratio D is defined in (5.2), which is an important parameter for describing multiple saliencies

$$D = \frac{I_{cnh}}{I_{cn2}}. \tag{5.2}$$

The existing decoupling methods using modeling [2] or look-up table [60] and other similar attempts (e.g, [3], [7], [61]) are presented for decoupling the secondary saliency signals. They work well when the magnitude of the secondary saliency signal is weak $D < 0.5$. However, as reported in [10] and [62], these decoupling methods fail if $D > 0.5$. From Fig. 5.2, it can be seen that the saliency ratio $D = \frac{I_{cn4}}{I_{cn2}}$ of the tested cwSPMSM is near 1.7 ($D^{-1} > 0.5$), which is beyond the working range of existing decoupling methods (i.e., traditional decoupling method for either primary saliency signal or secondary saliency signal dose not work any more). In order to solve this problem, three attempts are carried out.

Firstly, in addition to the high saliency ratio property of the machine, the dependency of the saliency signal on the injection frequency ($\Delta L_i = f(\omega_c)$) is another property that did not get the proper attention and is the foundation of the MSI method and will be explained in the following part of the MSI method. The first method can be seen as a combination method, while the other two are decoupling methods.

Secondly, on the contrary to the traditional primary saliency tracking method, the secondary saliency tracking method is proposed. This method utilizes a special designed BPF, which is designed based on the rotation difference between the primary and secondary saliency. An

adaptive notch filter acts as a supplementary to decouple the remaining primary saliency signal around zero speed.

Thirdly, another primary saliency tracking method is considered again. The repetitive control concept is brought into the PLL part so as to decouple the secondary saliency signal. It is not restricted by the saliency ratio and shows satisfactory performance.

5.1.4 The analysis of multiple saliencies

The former analysis has shown clearly the problem of multiple saliencies for the cwSPMSM. In this section, the physical mechanism of the strong secondary saliency is experimentally and theoretically verified and explained through two aspects: stator background and zigzag leakage flux. The stator background, taken literally, covers information of the stator. The zigzag leakage flux was already studied in [5, 63], which helps to explain the interaction between the stator and the surface-mounted PMSMs in this work. Finally, it can be concluded that the secondary saliency is a result of the combination of these two aspects.

5.1.4.1 Stator background

The main differences between the cwSPMSM and a normal distributed winding SPMSM (dwSPMSM) are the stator winding distribution, physical geometry and slotting (in summary, the stator background). Saliency tracking based sensorless methods substantially rely on the stator background and rotor permanent magnet position. In order to realize the impact of the stator background on the cwSPMSM, the alternating HF signal injection method is applied in this subsection.

The cwSPMSM was driven at constant speed of 50 rpm and a 1kHz 20V alternating signal was injected along the real d axis whose information was provided by an encoder. Because this injected HF signal was always along the d axis, its HF current response contained only the information of the stator background. The same tests have been done for a normal dwSPMSM as well. The parameters of both machines are listed in Table. C.3and C.4. It can be assumed in advance that, the trajectory of the HF current response should be a circle if the stator background is symmetrical within one electrical period.

The experimental results are given in Fig. 5.3. The outer dashed blue line represents the trajectory of the injected HF voltage signal in an electrical period, while the inner dashed red line represents the trajectory of its induced HF current response. Because the d/q axis HF currents obtained from the experimental data formulates a filled shape, only the profile that is of most importance is provided to show clearly the difference. From Fig. 5.3, it can be observed that the current response trajectory of the tested cwSPMSM shows a hexagon form in Fig. 5.3(b) compared to the circular trajectory of the normal dwSPMSM in Fig. 5.3(a).

The circular trajectory of the tested dwSPMSM shows, as expected, that the dwSPMSM's stator background is symmetrical. On the contrary, the hexagon form for the tested cwSPMSM results from the asymmetrical characteristic of its stator background. A reason is that each stator winding of the cwSPMSM locates around one tooth (tooth winding) [5] whose width is wider than that of the normal dwSPMSM. The self inductance of the cwSPMSM is more significant than the mutual inductance. As a consequence, the current flow inside the stator winding is more sensitive to the change of rotor flux distribution in comparison with dwSPMSM whose

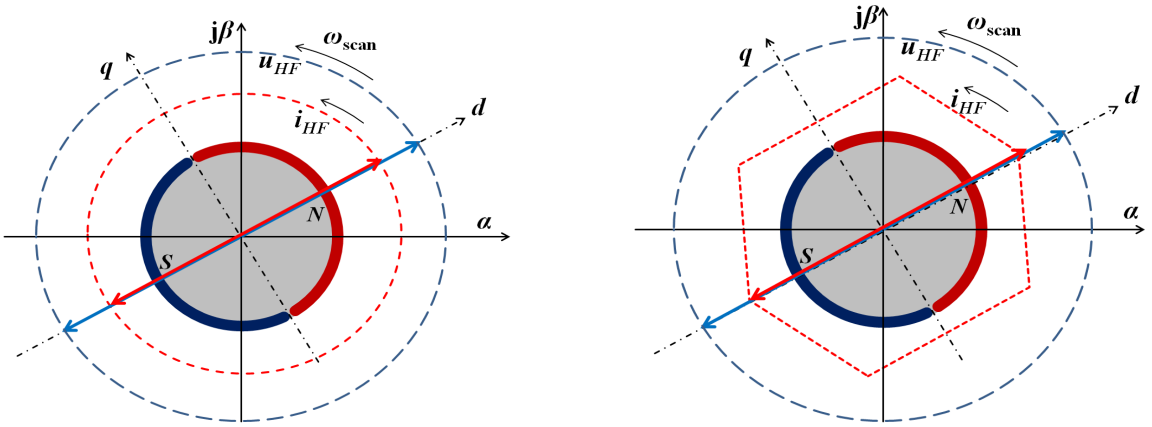

(a) Stator background of a normal dwSPMSM (b) Stator background of the tested cwSPMSM

Figure 5.3: Stator background comparison.

mutual inductance distribution is significant in the total phase inductance. Moreover, the shape of the hexagon can serve as a hint to infer the stator structure of the tested cwSPMSM.

The cross section of the tested cwSPMSM is speculated and a structure is demonstrated in Fig. 5.4 in accordance with the hexagon form. There are six teeth within one electrical period. Only two windings of phase A are shown and other phases' (B and C) windings are omitted for simplicity. However, the stator winding distribution mentioned in Fig. 5.4 is only one possibility and does not reflect the real machine structure. The main target of Fig. 5.4 is to explain the relation between the zigzag leakage flux and the main flux in the next subsection.

When the HF voltage signals are injected into the special stator windings of the cwSPMSM, its HF current response can reflect the interaction between the stator winding distribution and the rotor flux distribution. The interaction information recorded in the HF current response is, in fact, the saliency signal.

5.1.4.2 Zigzag leakage flux

In addition to the special stator background of the cwSPMSM, there is another phenomenon called the "zigzag leakage flux" which is the physical mechanism of the secondary saliency as well.

Both, the main flux (two big ellipses, single line) and the zigzag leakage flux (two small circulars around the stator winding, double line), are shown in Fig. 5.4 for a one-pole-pair PMSM model, which is a sketch map to show the special phenomenon of the "zigzag leakage flux". The zigzag leakage flux can be more significantly observed by the cwSPMSM compared with the dwSPMSM [5]. Moreover, the superimposed rotating HF flux is a leakage flux around the stator winding [64] and its HF current response reflects the flux distribution near the stator. As a result, when the rotating HF signal scans one electrical period (one circumference in Fig. 5.4), it can detect that the main flux distribution changes twice, which is the physical origin of the primary 2nd saliency signal ($L_q < L_d$ for HF components [64]).

On the one hand, the zigzag leakage flux locates in the q axis (actual d axis winding) and it decreases L_d and makes the difference between L_d and L_q smaller. On the other hand, the

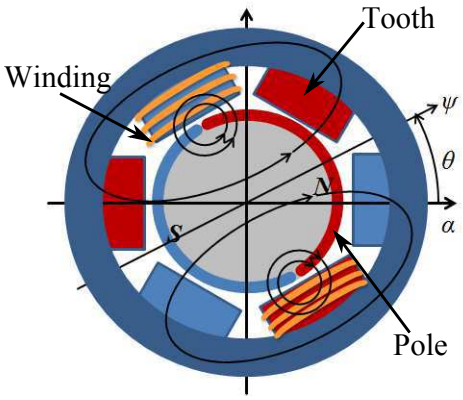

Figure 5.4: Flux distribution.

zigzag leakage flux and its equivalent part of the main flux near the tooth winding can be treated as a periodical saliency. Its period is half of a pole pitch and it results in the secondary -4th saliency [58].

In general, different from the primary saliency signal (saturation induced saliency signal, highly depending on operating points of the motor), the secondary saliency signal is mainly induced by the mechanical configuration (e.g.,slots/poles combination, winding distribution, magnet installation etc). In this work, for the tested cwSPMSM, the reason is the zigzag leakage flux combined with the tooth winding structure, which means it is less sensitive to operating points and is therefore more reliable [65]. The insensitivity of the secondary saliency signal will be shown later in the experimental section.

Note that, in practice, the frequency of the excitation HF signal should be much higher than the frequency of the fundamental signal in order to make sure the easy separation between fundamental signals and HF signals. Therefore, in this work, a 1kHz signal is chosen for both alternating (only used in previous subsection to detect the stator background) and rotating (for the rest sections) HF signal injection methods.

5.1.4.3 Impact of slot/pole combination

There are already some papers [5, 65] dealing with the effect of slot/pole combination on the performance of the PMSM. It is demonstrated that the combination indeed has an impact on saliency creation including the zig-zag flux-based saliency.

In [5], the authors have listed a table containing several possible slot/pole combinations for the cwSPMSM. The influence of the slot/pole combination on sensorless capability was also shown. A selection rule for choosing the combination was recommended and validated through a Finite Element Analysis (FEA) tool in the paper. Moreover, there is another paper [65], which gave a deep insight into the relation between the $d-q$ inductance and the slot/pole combination. The theoretical analysis was performed based on detailed machine parameters. As a result, the effect of the slot/pole combination on saliency signals should be taken into consideration by machine designers to design a high sensorless-capable machine.

5.2 Multi-signal injection method

In order to further investigate the saliency behavior of a cwSPMSM, a series of experimental tests have been developed. It has been found that the behavior of the multiple saliencies of the cwSPMSM is principally frequency dependent. Based on the characteristics of such machines, the Multi-Signal Injection method for realizing sensorless control is proposed. This method injects multiple HF signals with different frequencies and magnitudes into the machine. Different frequency components in the response current signals are demodulated and then combined together to get the clear primary saliency signal, which is used to identify the rotor position. This new method was validated using a cwSPMSM at low speed. The experimental results proved the effectiveness and accuracy of the new method.

5.2.1 Derivation of the proposed MSI method

5.2.1.1 Precise multiple saliencies model

Further investigation of the machine saliencies reveals that the saliency behavior often changes depending on the frequency of the injected carrier signals. The changing rates of the magnitudes I_{cnh}, for different saliencies, are also dependent on frequencies. The saliency behavior has a relationship to the voltage magnitude of the injected signals as well but it plays a less important role in this variation [64]. In this section, we focus on the relationship to the frequency. Thus, the multiple saliencies model should be more precisely represented as in

$$i_c^s = I_{cp}(\omega_c)e^{j(\omega_c t-\pi/2)} + \sum_h I_{cnh}(\omega_c)e^{j(-\omega_c t+h\theta_e+\varphi_i-\pi/2)} \tag{5.3}$$

The magnitudes of the positive and negative carrier currents of the h-th order saliency become carrier frequency dependent (nonlinear relationship), and are redefined in

$$I_{cp}(\omega_c) = \frac{V_c}{\omega_c}\left[\frac{\Sigma L(\omega_c)}{\Sigma L^2(\omega_c) - \sum_k \Delta L_k^2(\omega_c)}\right] \tag{5.4}$$

$$I_{cnh}(\omega_c) = \frac{V_c}{\omega_c}\left[\frac{\Delta L_i(\omega_c)}{\Sigma L^2(\omega_c) - \sum_k \Delta L_k^2(\omega_c)}\right] \tag{5.5}$$

where ΔL_i represents the inductance difference of the related hth-order saliency. k is the saliency order.

If a single carrier signal with a constant frequency is used, the saliency behavior does not show any difference compared with the model of (3.44). However, this frequency dependent property can be used to observe the rotor position by simultaneously injecting multiple carrier signals with different frequencies.

5.2.1.2 Principle of MSI method

If multiple carrier signals with different frequencies are applied on the machine, the multiple saliencies model is described as

$$\begin{aligned} i^s_{dqc} = \sum_m \Big[& I_{cp}(\omega_{cm}) e^{j(\omega_{cm}t - \pi/2)} + \\ & \sum_h I_{cnh}(\omega_{cm}) e^{j(-\omega_{cm}t + h\theta_e + \varphi_{mh} - \pi/2)} \Big] \end{aligned} \tag{5.6}$$

where $m = 1, 2, \ldots M$ and $h = 1, 2, \ldots N$.

If M signals with different frequencies are injected into the machine, the response current will contain M frequency components. Suitable BPFs can be used to separate them. The result is

$$\begin{aligned} i^s_{dqcm} = & I_{cpm} e^{j(\omega_{cm}t - \pi/2)} + \\ & \sum_h I_{cnmh} e^{j(-\omega_{cm}t + h\theta_e + \varphi_{mh} - \pi/2)} \end{aligned} \tag{5.7}$$

where $I_{cpm} = I_{cp}(\omega_{cm})$, $I_{cnmh} = I_{cnh}(\omega_{cm})$.

By multiplying $e^{j(\omega_{cm}t)}$ on both sides of each equation in (5.7), the new term of the positive sequence current has twice the frequency of the former one, which can be removed using a LPF. Thus, the pure rotor position information (5.8) can be extracted from the response signals (5.7).

$$i^{cn}_{dqcnm} = \sum_{h=1}^{N} I_{cnmh} e^{j(h\theta_e + \varphi_h + \delta_m - \pi/2)} \tag{5.8}$$

The signal processing will usually introduce different phase shifts to the current signals. Most of them are phase lag effects resulting from different filters and they are represented with δ_m in (5.8). They can be calculated from filter design parameters or experiment analysis. Whereas, φ_h has the same value for different injected signals. The term e^{δ_m} can be moved to the left side by multiplying a $e^{-\delta_m}$ on both sides of (5.8). The result is shown in

$$i^{cn}_{dqcnm} e^{-\delta_m} = \sum_{h=1}^{N} I_{cnmh} e^{j(h\theta_e + \varphi_h - \pi/2)} \tag{5.9}$$

If $M = N$, by combining all responses of N different signals, we can obtain the following expression (detailed process is explained in the Appendix)

$$i_{\boldsymbol{com}} = \sum_{m=1}^{M} \alpha_m i^{cn}_{dqcnm} e^{-\delta_m} = \beta e^{j(h\theta_e + \varphi_h - \pi/2)} \tag{5.10}$$

where α_m and β are combination parameters of I_{cnmh}. The combined signal $i_{\boldsymbol{com}}$ is a combination of all measured currents.

As a result, (5.10) only contains the information of the h-th order saliency, and all other saliencies are eliminated. Therefore, the multiple-saliency model is transformed to a single saliency model, and the rotor position can be easily estimated with the PLL, as in Fig. 3.4. To

get the best accuracy, usually the equation representing the most significant saliency is used for rotor position estimation. Here, this concept will be further explained with a model, which has only two saliencies, as an example for better understanding. In this case, two voltage signals with different frequencies are injected into the machine. Therefore, (5.9) becomes

$$\begin{cases} i^{cn}_{dqcn1} e^{-\delta_1} = I_{cn11} e^{j(h_1\theta_e+\varphi_1-\pi/2)} + I_{cn12} e^{j(h_2\theta_e+\varphi_2-\pi/2)} \\ i^{cn}_{dqcn2} e^{-\delta_2} = I_{cn21} e^{j(h_1\theta_e+\varphi_1-\pi/2)} + I_{cn22} e^{j(h_2\theta_e+\varphi_2-\pi/2)} \end{cases} \tag{5.11}$$

Supposing the first saliency $h_1\theta_e$ is to be used for rotor position estimation, it can be defined

$$i_{\boldsymbol{com}} = I_{cn22} i^{cn}_{dqcn1} e^{-\delta_1} - I_{cn12} i^{cn}_{dqcn2} e^{-\delta_2} \tag{5.12}$$

Substituting (5.11) into (5.12), it is (5.13)

$$i_{\boldsymbol{com}} = (I_{cn11} I_{cn22} - I_{cn21} I_{cn12}) e^{j(h_1\theta_e+\varphi_1-\pi/2)} \tag{5.13}$$

(5.13) proves that the combined current signal $i_{\boldsymbol{com}}$ only contains the information of the first saliency. And the original double-saliency model is now converted to a single-saliency model. However, in practice, (5.12) is used to calculate the combined current signal $i_{\boldsymbol{com}}$. A more practical variation of (5.12) is (5.14)

$$i_{\boldsymbol{com}f} = \frac{e^{\delta_1}}{I_{cn22}} i_{\boldsymbol{com}} = i^{cn}_{dqcn1} - \frac{I_{cn12}}{I_{cn22}} e^{\delta_1-\delta_2} i^{cn}_{dqcn2} \tag{5.14}$$

$i_{\boldsymbol{com}f}$ is the final signal that is to be input into the PLL for flux angle estimation. Using this equation, only the relative ratio $\frac{I_{cn12}}{I_{cn22}}$ of the same saliency magnitudes under different injection conditions and the phase difference $e^{\delta_1-\delta_2}$ are necessary. Exact values are not required. This can make the application much easier. The complete flux estimation procedure can be illustrated with Fig. 5.5.

In Fig. 5.5, two HF signals with different frequencies are injected. "**1**" represents the first signal with lower frequency, "**2**" represents the second signal with higher frequency. The criteria to choose these two signals is that they can result in significant different saliency ratios (e.g., $D_1 = 0.56$, $D_2 = 2.25$ in the experiment Fig. 5.6 of this work). These two NSCs are obtained through a respective demodulator. This combination procedure is expressed in (5.14), in which $e^{\delta_1-\delta_2}$ can be acquired by comparing with a reference signal of multiple saliencies generated by an encoder. Afterward, they are combined to get only $h_1\theta_e$ saliency, which will drive the PLL in the next step.

5.2.1.3 Remarks of MSI method

For the machines which show strong multiple saliencies, the ratio D is remarkable, which invalidates the existing decoupling methods [10]. On the contrary, the multi-signal injection method utilizes another characteristic, $\Delta L_k = f(\omega_c)$ to implement sensorless control. This method has the following advantages:

- Complicated modeling and training process based on mass commissioning are not required.
- The NSC responses reflect intrinsically the same multiple saliencies information, which guarantees the precise combination.
- If the primary saliency ($2\theta_e$) is chosen as the final combined saliency, the existing polarity identification methods can be applied for the initial position estimation.

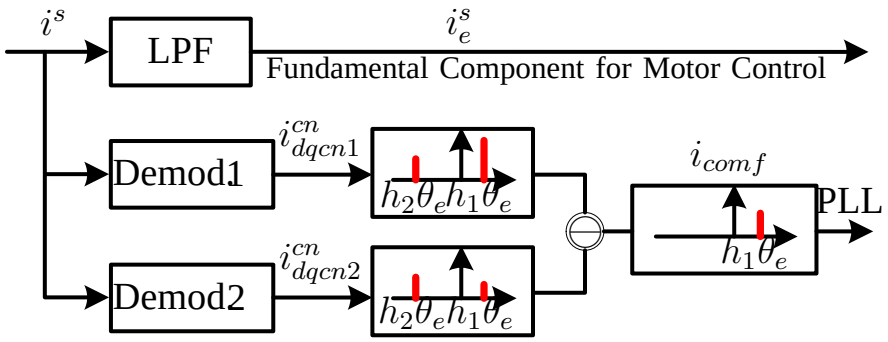

Figure 5.5: Multi-signal injection method.

5.2.1.4 Other related issues

All HF based sensorless methods have the disadvantage of increasing the losses, both in the rotor and in the stator. These issues are really great research topics and need to be studied individually. Fortunately, some related HF loss analysis such as eddy current loss [66], hysteresis loss [67], temperature issues [68] for HF injection based methods have already been studied during the recent years. Especially according to the conclusions of [69], the cwSPMSM is better suited for HF injection based sensorless methods and it has minor impact on the HF losses. Furthermore, for higher speeds, the switchover to a model-based sensorless method is mandatory since then, the loss issues resulting from the HF injection are no longer present. On the other hand, it is a time-consuming work to give the precise loss analysis based on FEA due to the lack of knowledge about the detailed stator, rotor, and material information of the tested cwSPMSM, which is a commercial product from the company SEW. As a result, we did not include loss analysis due to the above reasons and the limited scope of this work. But it will be the topic of ongoing research.

Another issue of the HF based sensorless methods is the so called HF-induced resistance effect or eddy-current-reflected asymmetric resistance presented in [6, 66, 70]. Most of all, in [6], the authors gave a comparison between inductance-based and resistance-based sensorless control for the cwSPMSM. The conclusion of this work shows that the inductance-based method is more suitable than the resistance-based method for the cwSPMSM, which has a lower SNR.

The inverter non-linearity effects of the HF injection method are also important and have been studied in [4, 71, 72]. In the experiments of this work, the dead time of the inverter is set to 0.8 μs which is shorter than [71, 72] and comparable with [4]. According to the conclusion of [4], for such dead-time the non linearity effects are small for both rotating and pulsating carriers. Furthermore, the magnitude and phase become sensitive to the loading of the inverter, but this effect is also not very significant either. We have tested the saliency ratio of this cwSPMSM based on other test benches with different controllers and similar dead time inverters. They all demonstrate that these non linearity effects are not so significant.

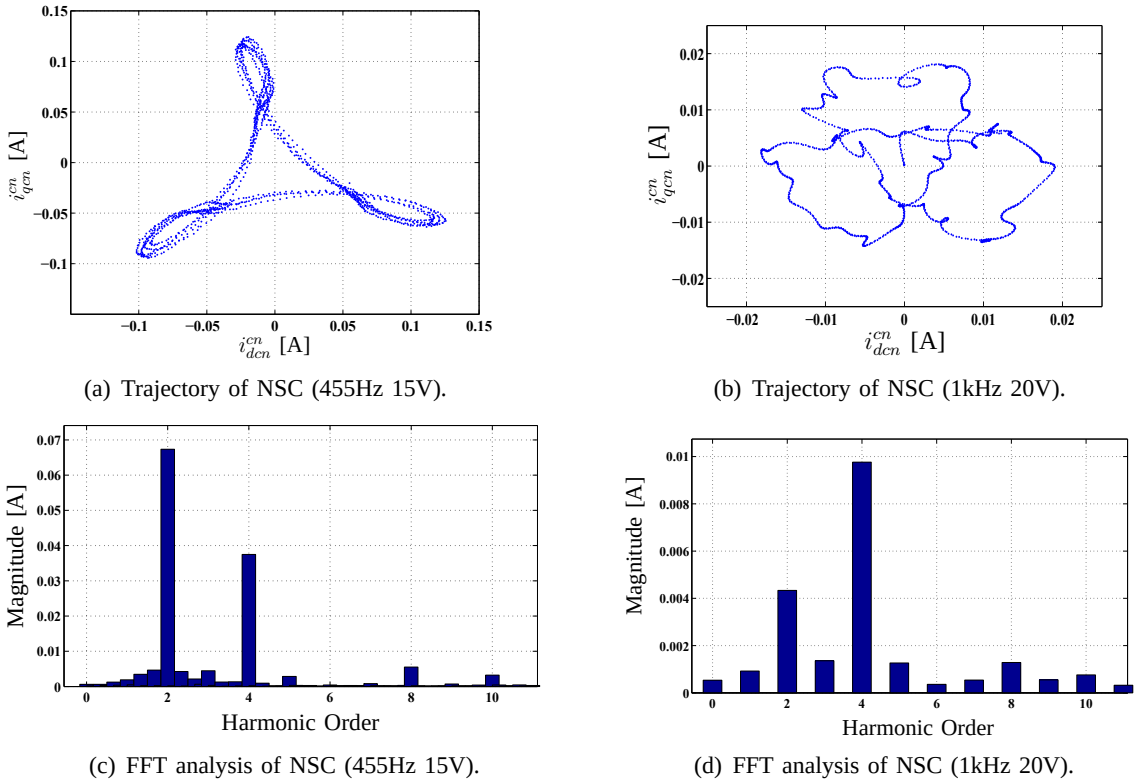

(a) Trajectory of NSC (455Hz 15V).

(b) Trajectory of NSC (1kHz 20V).

(c) FFT analysis of NSC (455Hz 15V).

(d) FFT analysis of NSC (1kHz 20V).

Figure 5.6: NSC trajectory and FFT Analysis, left: (455Hz 15V), right: (1kHz 20V).

5.2.2 Behavior of the frequency-dependent saliencies

In this part, all the expressions and experimental results are carried out using the traditional rotating HF injection method.

For a normal SPMSM with distributed windings, the trajectory of the NSC, depending on the flux angle, is a circle due to the presence of only one primary saliency $2\theta_e$ as depicted in (3.43). However, the relatively lower stator slot numbers, combined with the concentrated winding structure in cwSPMSMs, bring extra saliencies into the machine. Experimental results of the NSC trajectory for a cwSPMSM are given in Fig. 5.6.

From Fig. 5.6(a) and 5.6(b), it is seen that the NSC trajectory is eccentric and shows a form with lobes [58], [73]. With the spectral FFT analysis given in Fig. 5.6(c) and Fig. 5.6(d), this NSC contains two major frequency components, $2\theta_e$ and $-4\theta_e$.

According to the multiple saliencies model (5.3), the NSC response for the cwSPMSM can be expressed as

$$\begin{aligned} i_c^s =& I_{cp}(\omega_c)e^{j(\omega_c t-\pi/2)} + I_{cn2}(\omega_c)e^{j(-\omega_c t+2\theta_e+\varphi_2-\pi/2)}+ \\ & I_{cn4}(\omega_c)e^{j(-\omega_c t-4\theta_e+\varphi_4-\pi/2)} \end{aligned} \tag{5.15}$$

It contains the primary saliency $2\theta_e$ and the secondary saliency $-4\theta_e$.

Furthermore, from Fig. 5.6 we can also find that this trajectory changes with the frequency variation of the injected signals. Fig. 5.6(c) gives the result of the injected signal with 455Hz 15V and the magnitude of the $2\theta_e$ saliency is nearly 1.5 times the magnitude of the $-4\theta_e$

saliency. Whereas in Fig. 5.6(d), when the injected signal is 1kHz 20V, the magnitude of the $-4\theta_e$ saliency is twice the magnitude of the $2\theta_e$ saliency. Note that, saliency magnitudes under 1kHz 20V are relatively lower compared to the result of the 455Hz 15V condition due to the inverse relationship between the saliency magnitude and the frequency of the injected signal $I_{cnh} \propto \frac{V_c}{\omega_c}$.

To investigate more about this special characteristic of the cwSPMSM, many experiments were done and the conclusion is summarized in (5.16) (saliency ratio $D = \frac{I_{cn4}}{I_{cn2}}$)

$$D \Rightarrow \begin{cases} 0.6 < D \leq 1 & \text{if } f_c < 500\text{Hz}, \\ \text{Resonance} & \text{if } 500\text{Hz} < f_c < 600\text{Hz}, \\ D > 1.5 & \text{if } f_c > 600\text{Hz} \end{cases} \tag{5.16}$$

where f_c is the frequency of the injected signal and $\omega_c = 2\pi f_c$.

The results of injection conditions between 500Hz and 600Hz have not been performed due to the mechanical resonance problem. Even without these results, the provided measurements based on many tests can reveal the variation tendency of this saliency ratio according to the frequency of the injected signal.

From this conclusion (5.16), it is obvious that the magnitude of the secondary saliency of the cwSPMSM is comparable or even larger than the primary saliency. This conclusion confirms the former relationship $\Delta L_i = f(\omega_c)$.

5.2.3 Application of MSI Method

The multi-signal injection method is suitable for the sensorless control of cwSPMSM which has strong multiple saliencies. As described above, the primary saliency $h_2 = 2$ and the secondary saliency $h_4 = -4$ can be found in its NSC responses. The example of the double-saliency model in (5.11)-(5.14) can be used. Then, only the primary saliency is left after this combination. Based on the saliency signal obtained with the multi-signal injection method, traditional sensorless methods can be applied.

5.2.4 Implementation and experiment results

5.2.4.1 Combination parameters

There are two parameters during the combination procedure. The ratio, $\frac{I_{cn12}}{I_{cn22}}$, which is measured by an FFT analysis, and the angle difference, $\delta_1 - \delta_2$, which is obtained by comparing with a reference signal of multiple saliencies generated by an encoder. It has close relation to the parameters of designed filters and the sampling frequency of the controller

- Utilizing BPFs and LPFs, we can get the separate saliency responses as shown in (5.8) for different HF conditions ((5.17) is for 1kHz and (5.18) is for 455Hz). Then an FFT tool is adopted to obtain their individual magnitudes including I_{cn11}, I_{cn12}, I_{cn21} and I_{cn22} as they are shown in Fig. 5.6.

- In order to acquire the angle difference $\delta_1 - \delta_2$, the position θ_e measured by an encoder will be used as a parameter to produce a reference signal of multiple saliencies as shown

in (5.19) and (5.20), in which the parameters λ_{1-4} are adjustable. λ_1 and λ_3 represent the phase lags and λ_2 and λ_4 denote the phase shifts between these two saliency signals.

- Using real time D/A channels of our control system, we can output (5.17) and (5.19) or (5.18) and (5.20) signals to an oscilloscope at the same time. Then, adjusting parameters λ_{1-4} can make the outline of (5.19) coincide with (5.17) and the outline of (5.20) coincide with (5.18). Comparing the equations (5.17)-(5.20), we get (5.21)-(5.22). Then it is easy to get the angle difference $\delta_1 - \delta_2$ in (5.23). (Normally, φ_1 is treated as 0 for simplification without introducing any difference)

$$i_{dqcn1}^{cn} = I_{cn11} e^{j(2\theta_e + \delta_1 + \varphi_1 - \pi/2)} + I_{cn12} e^{j(-4\theta_e + \delta_1 + \varphi_2 - \pi/2)} \tag{5.17}$$

$$i_{dqcn2}^{cn} = I_{cn21} e^{j(2\theta_e + \delta_2 + \varphi_1 - \pi/2)} + I_{cn22} e^{j(-4\theta_e + \delta_2 + \varphi_2 - \pi/2)} \tag{5.18}$$

$$i_{ref1} = I_{cn11} e^{j(2(\theta_e + \lambda_1) - \pi/2)} + I_{cn12} e^{j(-4(\theta_e + \lambda_1) + \lambda_2 - \pi/2)} \tag{5.19}$$

$$i_{ref2} = I_{cn21} e^{j(2(\theta_e + \lambda_3) - \pi/2)} + I_{cn22} e^{j(-4(\theta_e + \lambda_3) + \lambda_4 - \pi/2)} \tag{5.20}$$

$$2\lambda_1 = \delta_1 \tag{5.21}$$

$$2\lambda_3 = \delta_2 \tag{5.22}$$

$$\delta_1 - \delta_2 = 2\lambda_1 - 2\lambda_3 \tag{5.23}$$

5.2.4.2 Flux angle estimation

In practice, the experimental data should replace the corresponding ones in Fig. 5.5: "**1**" represents 455Hz 15V signal, "**2**" represents 1kHz 20V signal. The saliencies information in Fig. 5.6 is depicted in

$$I_{cnh} \Rightarrow \begin{cases} I_{cn2} = 67\text{mA}, I_{cn4} = 38\text{mA} & f_c = 455\text{Hz}15\text{V} \\ I_{cn2} = 4\text{mA}, I_{cn4} = 9\text{mA} & f_c = 1\text{kHz}20\text{V} \end{cases} \tag{5.24}$$

The combination parameters are $\frac{I_{cn12}}{I_{cn22}} = 4.22$, $\delta_1 - \delta_2 = \pi$.

After the signal combination, we kept the $2\theta_e$ saliency instead of the $-4\theta_e$ one. The following two reasons support this selection.

- The primary saliency of signal "**1**" has a higher SNR. This is an advantage to get a more precise position and speed estimation.
- The secondary saliencies (always high order e.g., $-4\theta_e$, $8\theta_e$) are considered as interferences for initial polarity identification, which is essential to start a PMSM, and thus should be eliminated

Based on the experimental results, the NSCs were extracted and the d axis components are demonstrated in Fig. 5.7. The first two curves show the d-axis components of the NSCs responses of signal "**1**" and signal "**2**", respectively. The third curve shows the d axis component of the synthesized signal using the multi-signal injection method. The last curve shows the estimated rotor position, which is precise enough to implement closed-loop control.

Observing Fig. 5.7, it is obvious that the synthesized signal, i_{dcomf}, shows a regular sinusoidal form. This indicates that the signal precisely expresses the rotor position information.

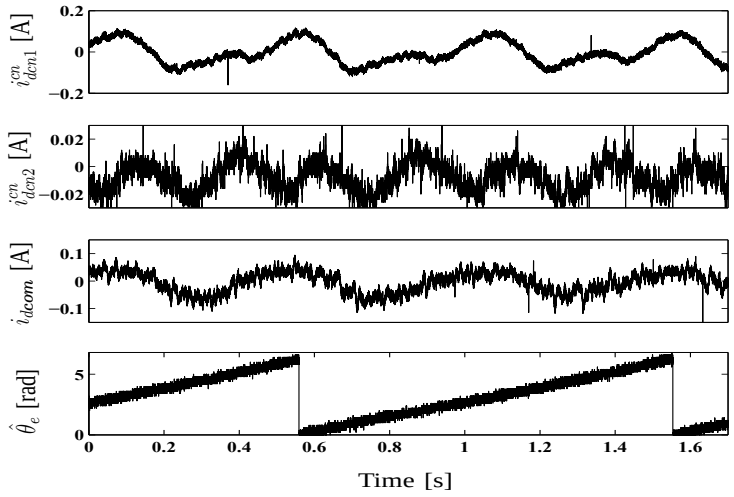

Figure 5.7: Flux angle estimation results of the multi-signal injection method.

5.2.4.3 Sensorless experimental results

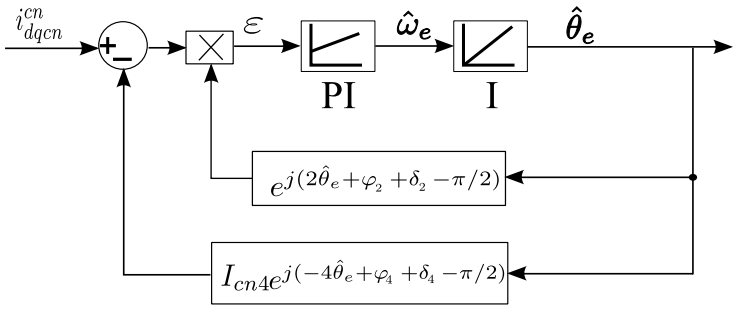

Figure 5.8: Block diagram of the decoupling method.

For comparison, the decoupling method mentioned in [1], whose structure is depicted in Fig. 5.8, was tested for sensorless control of the cwSPMSM. The HF condition is 455Hz 15V. It failed, however, because the estimated rotor position was not accurate enough for the closed-loop control. Therefore, only the open-loop estimation performance at 100 rpm (0.03 rated speed) is shown in Fig. 5.9. The blue line represents the reference rotor position θ_e measured by the encoder, which was fedback for the speed control loop. The red line denotes $\hat{\theta}_e$. Obviously, this decoupling method fails to estimate the rotor position in the presence of strong multiple saliencies. The $\hat{\theta}_e$ and θ_e have almost 180 electrical degree difference, which is because the NS poles identification function is not added to this traditional method and they have 50% chance to converge to S pole (180 degree) or to N pole (0 degree). We took the result that the tracking has 180 degree error in order to clearly show the difference between the reference and the estimated values.

The proposed multi-signal injection method for closed-loop estimation was firstly tested at 100 rpm speed without load. The measured speed ω_e and position θ_e, the estimated speed $\hat{\omega}_e$ and position $\hat{\theta}_e$, and the position error $\tilde{\theta}$ are presented in Fig. 5.10. The speed error (not shown) $\tilde{\omega}$ is limited within ± 10 rpm and the peak value of the position error of $\tilde{\theta}$ is less than

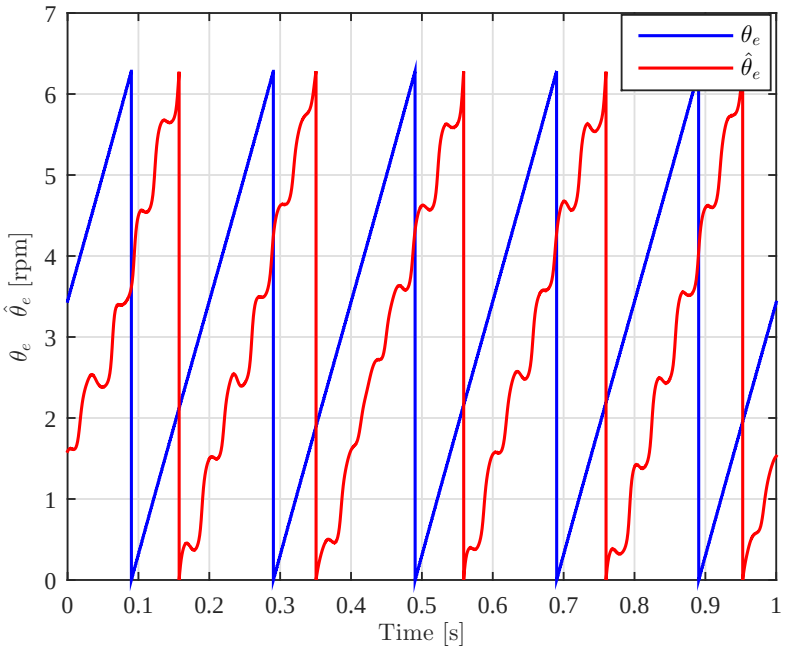

Figure 5.9: Position estimation performance at 100 rpm speed using the traditional decoupling method.

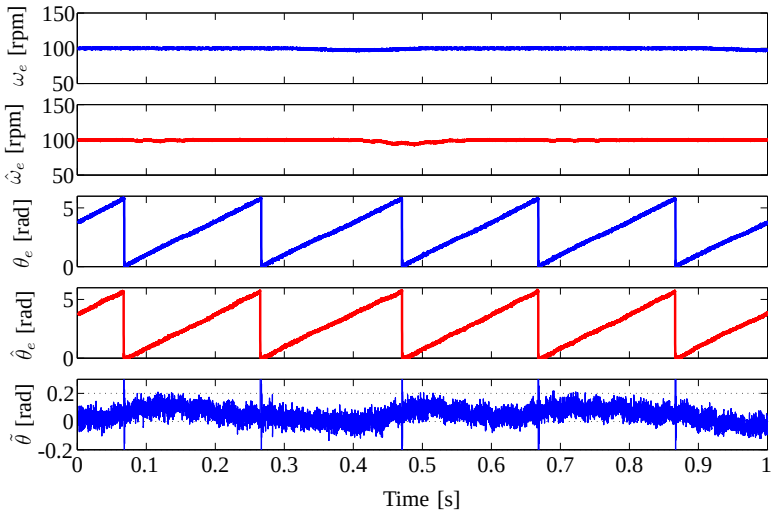

Figure 5.10: Sensorless performance at 100 rpm speed without load using the multi-signal injection method.

0.2 rad. The error mainly arises from the speed filter parameter- and speed loop PI parameter-tuning. However, the average value is almost zero. This test verifies that the multi-signal injection method has a better estimation performance than the traditional decoupling method for machines which show strong multiple saliencies.

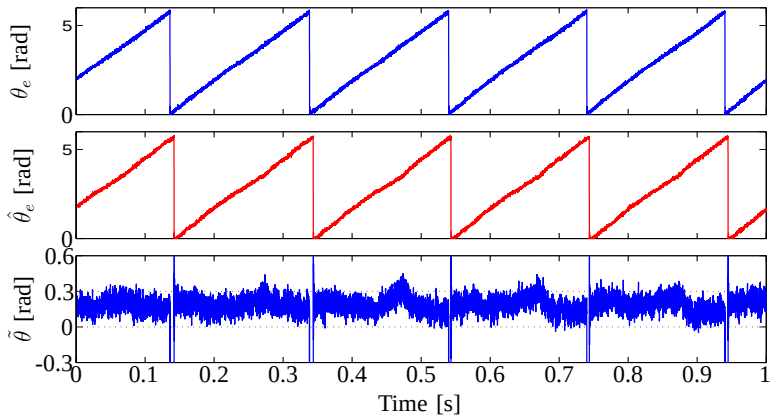

Figure 5.11: Sensorless performance at 100 rpm speed with a rated load torque using the multi-signal injection method without compensation.

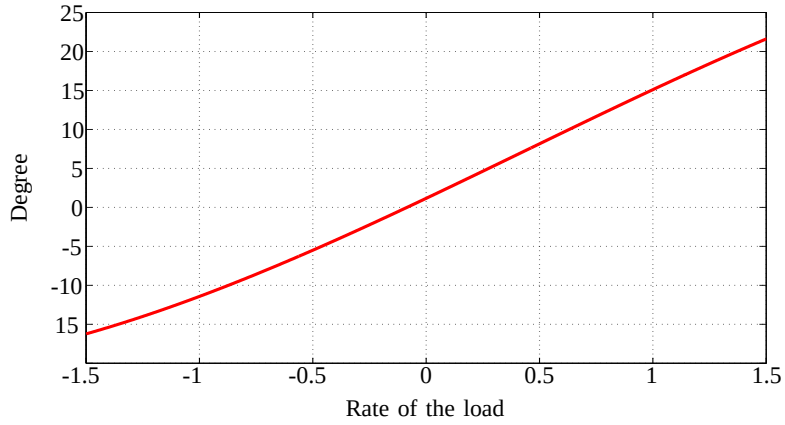

Figure 5.12: Load dependent angle compensation.

As described before, HF based sensorless methods have the the disadvantage of increasing the losses. With higher speed, the switchover to a model based sensorless method is mandatory. Therefore, it was verified on the test bench that the model based method such as the MRAS can work well at the speed reference higher than 200 rpm with or without load. Thus, sensorless control of cwSPMSM will be implemented by using model based methods in the middle and high speed ranges to eliminate the noise and losses induced by the HF injection based methods. Therefore, only different loads at 100 rpm have been investigated based on the multi-signal injection method. The results showed that the system was stable at different loads. For a load less than 30% of the rated load, the position error $\tilde{\theta}$ was similar to that in Fig. 5.10. However, for a load greater than 40% of the rated load, the position error $\tilde{\theta}$ increased. A full load test at 100 rpm

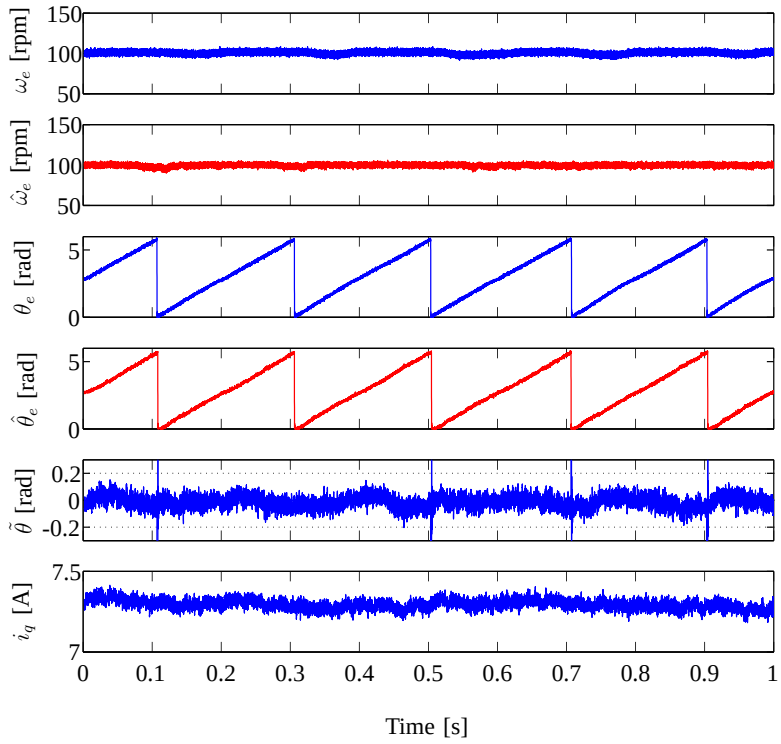

Figure 5.13: Sensorless performance at 100 rpm speed with a rated load torque using the multi-signal injection method with a compensation.

rotating speed is presented in this work. Experimental results are given in Fig. 5.11. Compared to the no-load test, the peak of the position error became larger and reached 0.3 rad, which resulted from the load dependent variation of the flux displacement [74]. This error can be compensated by either a LUT or a polynomial function. To compensate this error, the LUT was built as shown in Fig. 5.12. The picture introduces a curve regarding the relationship between the compensated angle and the rate of the load. The data was collected on the test bench. The same test with a rated load at 100 rpm was investigated by considering the compensation with this LUT method and experimental results are depicted in Fig. 5.13. The parameter definitions are the same with Fig. 5.10 and the q-axis current i_q is presented as well. From Fig. 5.13, the position error $\tilde{\theta}$ has obviously decreased compared to the previous one without compensation and the average error of the position is almost zero.

The system dynamic performance was observed by implementing a low speed reverse test. The speed reference varied from 100 rpm to -100 rpm and vice versa. The results are given in Fig. 5.14, which shows the same parameters as in Fig. 5.13. From Fig. 5.14, the highest $\tilde{\theta}$ is about 0.17 rad, while the mean error of $\tilde{\theta}$ at steady state is less than 0.07 rad. Because the speed command trajectory is manually planed in this case, the dynamic response does not reach its fastest limit.

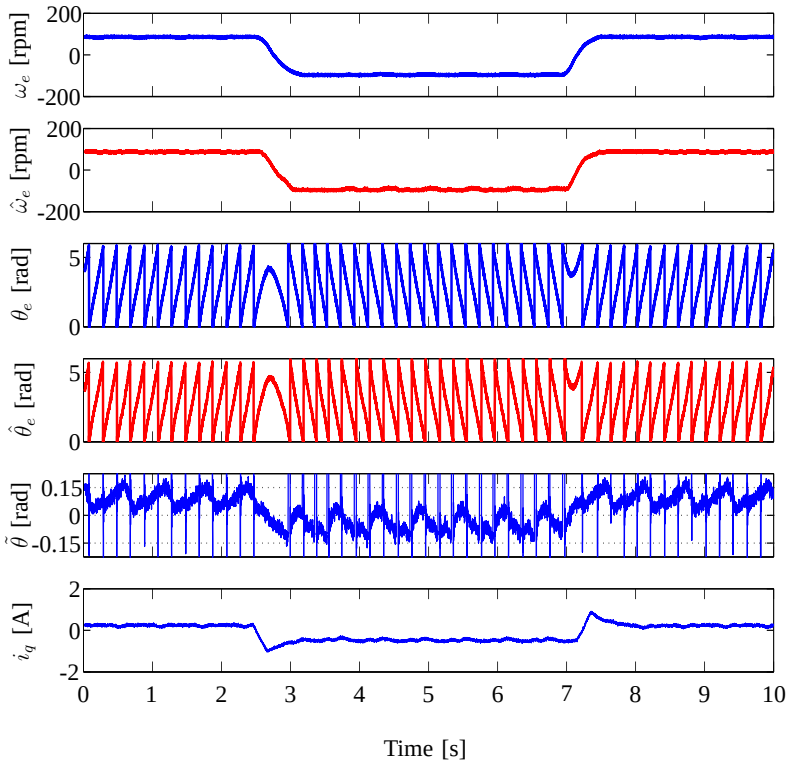

Figure 5.14: Sensorless performance of ± 100 rpm speed reverse using the multi-signal injection method.

5.2.5 Conclusion

A novel multi-signal injection method for solving a specific problem in sensorless control of cwSPMSMs is proposed in this section. For such machines, traditional sensorless control methods, based on a single HF signal injection, fail. Furthermore, if the high order saliencies are stronger than half of the primary saliency, even the decoupling methods, which are specifically designed for sensorless control of machines with multiple saliencies, fail too. In this situation, the multi-signal injection method proposed in this section provides a successful solution. This method utilizes another property of machines with multiple saliencies (i.e., the dependency of different orders of the saliencies on frequency).

This method was tested in an experimental system with a cwSPMSM. Although the machine showed very strong high order saliencies, especially with the fourth order saliency being even higher than the primary one above a certain frequency level, the multi-signal injection method still eliminated the influence of the fourth order saliency successfully and provided clear information about the rotor position, also in load condition. With the same method, the initial position of the rotor can be also estimated accurately within $\pm$ 3 electrical degrees.

Theoretical analysis reveals that the proposed multi-signal injection method is not limited to machines with only two saliencies. It is a general method and can be used for any machine with any order of saliencies. It has been proved that this method can remove any number of multiple saliencies and only leaves one saliency for the identification of the rotor flux position.

This multi-signal injection method has no restriction on the frequencies of the injected sig-

nals. This freedom makes it possible for engineers to select the optimal frequencies based on specific problems, such as to achieve the best SNR or to avoid mechanical resonances.

5.3 Secondary saliency tracking method

In this section, in addition to the Multi-signal injection method, a novel Secondary Saliency Tracking (SST) algorithm is proposed to implement the sensorless control exclusively for such machines in the low speed range. Instead of processing the primary saliency signal, the secondary saliency signal, which has a better signal to noise ratio and more precise resolution, is processed by a specially designed band pass filter and an adaptive notch filter for speed and rotor position estimation. The effectiveness and accuracy of the newly proposed SST method are verified by experimental results.

5.3.1 Secondary saliency tracking method

In this section, the selection principle of the most appropriate saliency signal to drive the PLL is firstly derived, which is a general rule for all saliency based sensorless methods. Then, the SST method together with a special BPF design are introduced in detail. At the end of this section, initial position identification based on the SST method is proposed accordingly.

5.3.1.1 Selection principle of saliency signals

For saliency based sensorless control methods, several selection principles of saliency signals for the position estimation are described as follows:

- The saliency signal should be a rotor position-dependent signal, which demonstrates exactly the physical characteristic of the rotor.
- The SNR of the saliency signal should be high enough to guarantee the accuracy of position estimation.
- The saliency signal should be less sensitive to operation points.

According to these three principles, comparisons between primary and secondary saliency signals are performed.

Firstly, it can be found in (5.1) that both primary and secondary saliency signals contain the rotor position information. There is no difference for both saliency signals. However, the secondary saliency signal has higher order and thus is of more precise resolution than the primary saliency signal.

Secondly, the saliency ratio of a cwSPMSM is $D = 1.7$. The secondary saliency signal has an obvious higher SNR than that of the primary saliency signal.

Finally, the primary saliency signal can be influenced by the cross-saturation and especially by secondary saliency signals. On the contrary, the secondary saliency signal is a structure-induced effect and it is less sensitive to operation points.

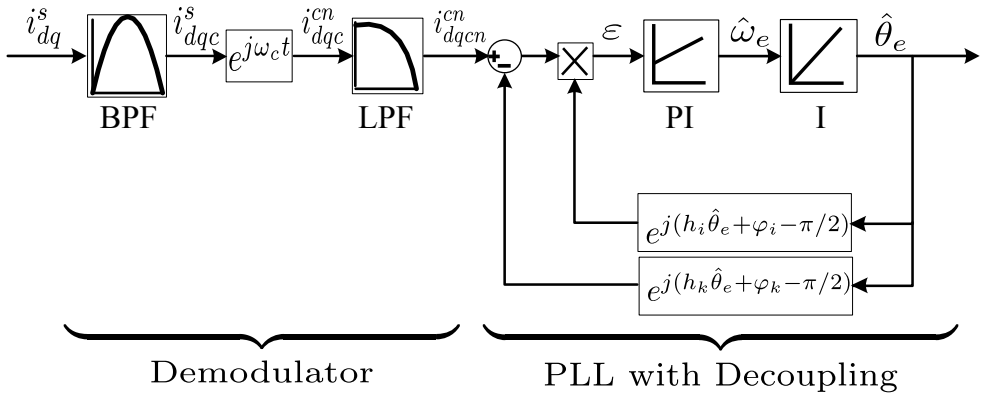

Figure 5.15: General decoupling of one saliency signal within PLL.

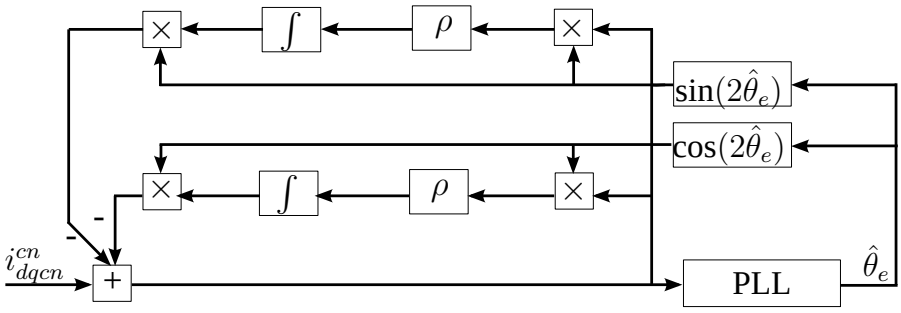

Figure 5.16: Decoupling of the primary saliency signal with ANF.

5.3.1.2 Secondary saliency tracking

Based on the previous analysis, the advantages of utilizing the secondary saliency signal for position estimation is clear. The SST method can operate also with the PLL as shown in Fig. 5.15. The comparatively weak primary saliency signal can be eliminated by two individually designed filters: a BPF and an adaptive notch filter.

Firstly, note that, a benefiting characteristic of the secondary saliency signal can be utilized: it rotates in a different direction compared with the primary saliency signal [58]. This makes it easier to extract only the secondary saliency signal through a specially designed BPF which locates in the upstream of the PLL as shown in Fig. 5.15. Its design procedures will be introduced in the following subsection. After the attenuation of the primary saliency signal by this BPF, the saliency ratio D becomes greater than 2 ($D^{-1} < 0.5$) and then the stability of the decoupling method is valid again, which means the primary saliency signal can be decoupled effectively.

Secondly, in order to further eliminate the effect of the residual primary saliency signal at very low speeds, an ANF mentioned in [75] is adopted between the demodulator and the PLL as a supplement. The structure of the ANF is illustrated in Fig. 5.16. It is of simple algorithm and only one parameter ρ is needed. ρ is set with 0.005 (it behaves like the PI parameter and has no unit) in practice. The ANF can adaptively change its output in accordance with operation points so that the primary saliency can be effectively decoupled.

5.3.1.3 Band pass filter design

Because the different rotations of the primary and secondary saliency signal result in different NSC signals, when the frequency of fundamental current is $f_e = 10\text{Hz}$, $\theta_e = 2\pi(10\text{Hz})t$, $\omega_c = 2\pi(1\text{kHz})$, these two saliency signals are

$$I_{cn2}e^{j(-\omega_c t+2\theta_e+\varphi_2-\pi/2)} = I_{cn2}e^{j(2\pi(-980\text{Hz})t+\varphi_2-\pi/2)} \tag{5.25}$$

$$I_{cn4}e^{j(-\omega_c t-4\theta_e+\varphi_4-\pi/2)} = I_{cn4}e^{j(2\pi(-1040\text{Hz})t+\varphi_4-\pi/2)} \tag{5.26}$$

From (5.25) and (5.26), it can be seen that with an increase of the fundamental frequency, the frequency difference between the primary and secondary saliency signals also increases. Moreover, they locate in different sides of the injected frequency, which can be utilized to separate one from another by a specially designed BPF. With the help of filter design functions in Matlab and a cascaded Second Order Sections (SOS) filter as shown in (5.27), it is convenient to implement a digital filter with any-order and any-expected performance. The final SOS filter needs only an L(rows)-by-6(column) matrix containing the coefficients of each second-order section in its rows (5.28).

$$H(z) = g\prod_{k=1}^{L} H_k(z) = g\prod_{k=1}^{L}\frac{b_{0k}+b_{1k}z^{-1}+b_{2k}z^{-2}}{1+a_{1k}z^{-1}+a_{2k}z^{-2}} \tag{5.27}$$

$$SOS = \begin{bmatrix} b_{01} & b_{11} & b_{21} & 1 & a_{11} & a_{21} \\ b_{02} & b_{12} & b_{22} & 1 & a_{12} & a_{22} \\ \vdots & \vdots & \vdots & \vdots & \vdots & \vdots \\ b_{0L} & b_{1L} & b_{2L} & 1 & a_{1L} & a_{2L} \end{bmatrix} \tag{5.28}$$

According to the previous analysis, an elliptic bandpass filter that has a steeper cut-off characteristic than the others is designed and the bode diagram of this example is shown in Fig. 5.17. The pass-band frequency is [f_c f_c+4f_e] and f_c locates in the left edge. This BPF can extract only the secondary saliency signal at a positive speed. In Fig. 5.15, it is $i^s_{dqc} = \mathcal{Z}^{-1}\{H(z)\}i^s_{dq}$ where $\mathcal{Z}^{-1}$ represents the inverse Z transformation. When the speed goes to negative, the rotations of both saliency signals change their signs, that means the NSC is $i^s_{dqc} = i^s_{dq} - \mathcal{Z}^{-1}\{H(z)\}i^s_{dq}$.

The designed BPF guarantees that the secondary saliency signal can be fully extracted out from current signals and meanwhile the magnitude of the primary saliency signal is attenuated greatly. The results of the NSC using the newly designed BPF are shown in Fig. 5.2(b) and 5.2(d). It is clearly seen that the secondary saliency signal dominates all saliency signals, which ensures a better SNR of the secondary saliency signal and a successful rotor position estimation based on the SST method. With the aid of the ANF demonstrated in Fig. 5.16, the primary saliency signal can be even suppressed so that the SST method works better.

5.3.1.4 Initial position estimation

Initial position is important for starting a PMSM. For the tested cwSPMSM, the secondary saliency signal rotates four times as the rotor flux completes one revolution. Therefore, similar to the fact that the primary saliency (2nd) signal solely cannot identify the N and S magnetic

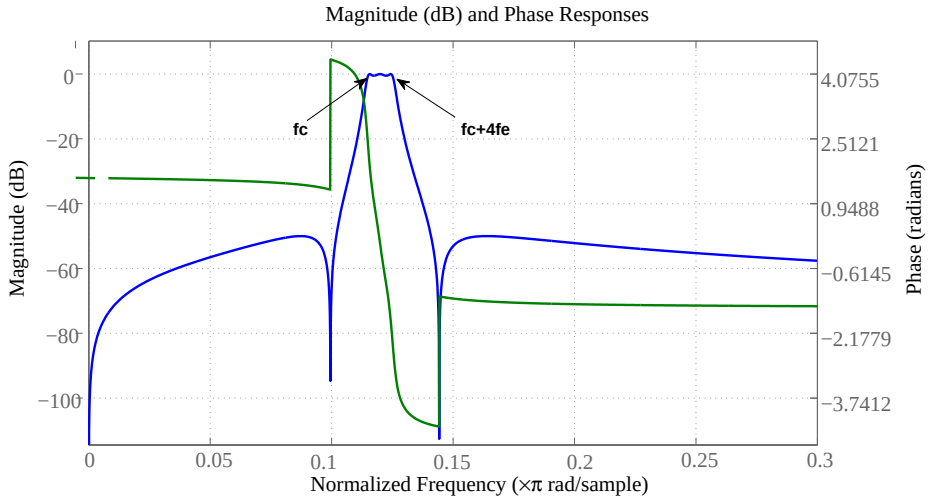

Figure 5.17: Specially designed BPF (Sampling frequency is 16kHz).

poles of the rotor, the secondary saliency signal solely cannot distinguish any two angles with a $\pi/2$ difference (or $n\pi/2$, where $n = 0, \pm 1, 2$ total 4 points). In this work, an initial position estimation based on the -4th saliency signal is proposed and the 4 convergence points are clearly distinguished as illustrated in Fig. 5.18.

During the initial position identification procedure, the $\pm\hat{d}$ axis pulse excitation method mentioned in [28] is extended for distinguishing another 2 points i.e., $\pi/2$ and $-\pi/2$ away from the N pole. σ is a threshold of the $+d$ and $-d$ axis current difference. If $\hat{\theta}_0$ converges to the N or S pole, σ should be large enough. On the contrary, if $\hat{\theta}_0$ converges to $\pi/2$ and $-\pi/2$, σ should be small since the flux path is vertical to the main flux. In this case, a $\hat{\theta}_0 - \pi/2$ correction of the park transformation is adopted to make the estimated position return to the N or S pole and then the same procedure will be done again. Once the initial position is corrected, it is ready to start the machine with a sensorless closed-loop control. In practice, $\sigma = 0.21A$ is set through trial and error tests.

5.3.2 Experimental results

The open loop estimation result (encoder measured position and speed are fedback to the FOC controller) of the primary saliency tracking method for the cwSPMSM was shown in Fig. 5.19, in which $\hat{\theta}_e$ and θ_e were included. Because the SNR of the secondary saliency signal is much higher than that of the primary saliency, the frequency of $\hat{\theta}_e$ is twice the frequency of θ_e. Moreover, they have opposite directions which results from the rotation difference of these saliency signals. The result illustrated that the primary saliency tracking method fails for a cwSPMSM because of its lower SNR and it is in accordance with the previous analysis.

To verify the sensitivity of the SST method to machine operation points, the load-dependent position estimation error of the SST method was compared with that of the MSI method. The experimental results of the comparison were shown in Fig. 5.20, where the red line is for the SST method and the blue line is for the MSI method. It can be observed from this figure that the

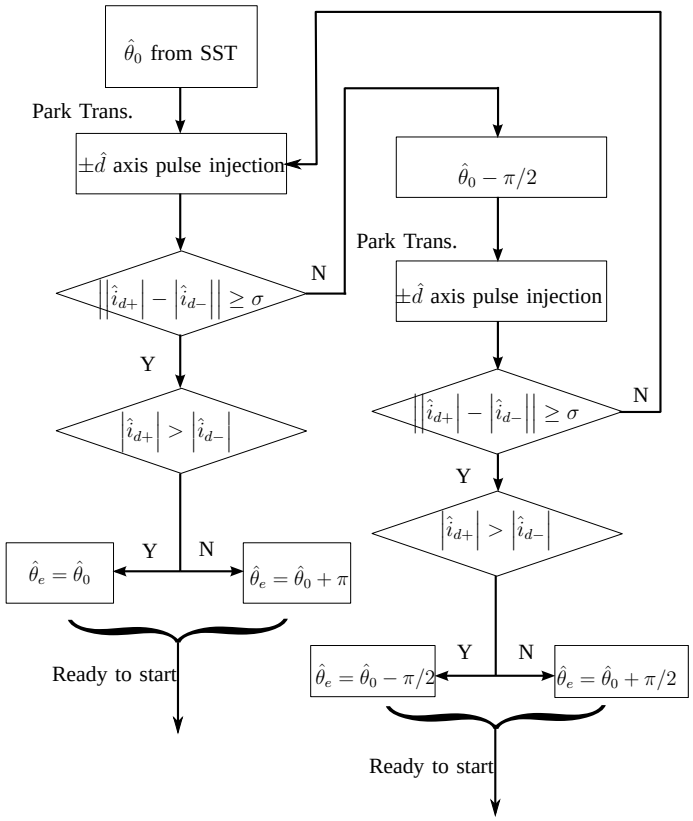

Figure 5.18: Initial position estimation flow chart.

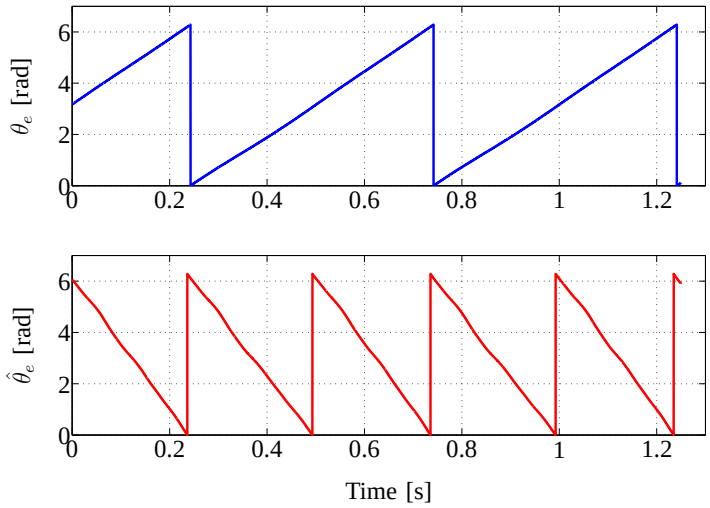

Figure 5.19: Primary saliency tracking results (rotating HF signal injection 1kHz,35V).

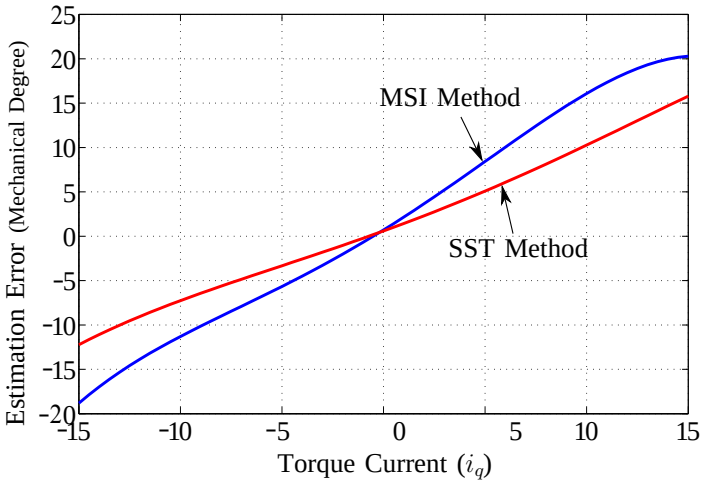

Figure 5.20: Load dependent angle compensation.

load-dependent error of the SST method is only half of that of the MSI method, which validated the insensitivity of the proposed SST method. In practice, the error was compensated by the LUT that was built according to the data in Fig. 5.20.

As analyzed before, the estimated $\hat{\theta}_e$ of the SST method at standstill may converge to 3 wrong points: $\pm\pi/2$ and π away from the correct position (N pole). Therefore, in order to verify the proposed initial position estimation method, experimental results of corrections at $-\pi/2$ and π were shown in Fig. 5.21(a) and 5.21(b), respectively. A flag is defined in the first sub-figure to illustrate the different stages in Fig. 5.18. Its values 0, 1, 4 and 3 represent the acquisition of $\hat{\theta}_e$, π and 0, $\pm\pi/2$ and the final correction stage, respectively (2 is reserved for another purpose). From Fig. 5.21, the difference of σ for these four convergence points is clear. The proposed initial position estimation method works well without load. Nevertheless, the frequencies of both saliency signals are zero at standstill and thus the designed BPF does not work. With the increase of load, the initial position estimation method becomes more sensitive to load and unstable. As a result, only a slight load (below 10% rated load) can be applied to the cwSPMSM at standstill right now. Further research will focus on the improvement of the zero-speed performance.

To verify the decoupling effectiveness of the ANF, a sensorless closed-loop test at 20 rpm (0.0067p.u.) with 50% rated load was done and the results were delivered in Fig. 5.22. From 0 second to 3.5 second, the ANF was disabled and the $\tilde{\theta}_e$ was great and reached near 0.2 rad. From 3.5 seconds on, the ANF was enabled. The $\tilde{\theta}_e$ became smaller than 0.1 rad. The test demonstrated that the ANF works well and is especially important for very low speed range sensorless control.

The speed tracking performance of the SST method was shown in Fig. 5.23. The speed command varied from 0 to 200 rpm and then back to 0. During the acceleration and deceleration transients, the $\tilde{\omega}_e$ is below 10 rpm and the $\tilde{\theta}_e$ is below 0.2 rad. At the steady state of 200 rpm, both $\tilde{\omega}_e$ and $\tilde{\theta}_e$ are around 0. When the speed goes higher than 200 rpm, a model based method can substitute the proposed SST method. The hybrid whole speed range sensorless control will be the topic of further work.

The proposed SST method for a sensorless closed-loop estimation was tested at 100 rpm

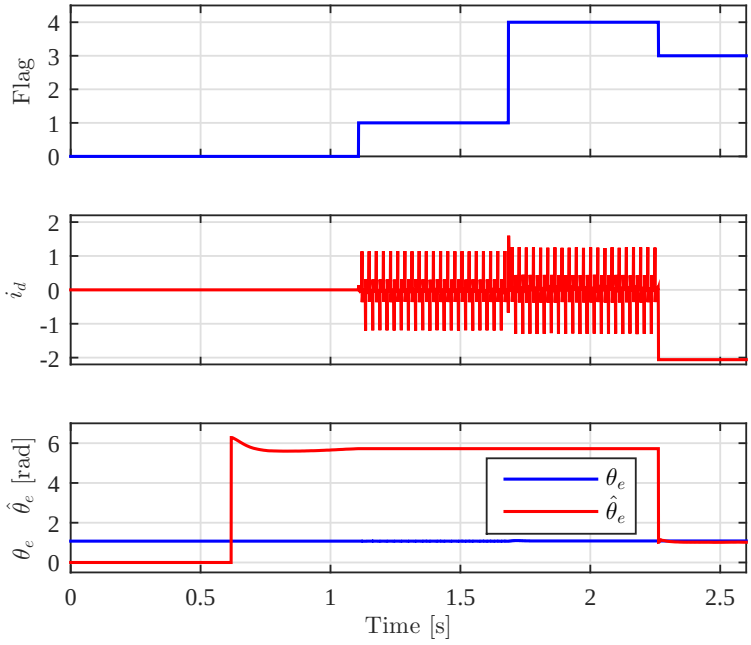

(a) Initial position converges to a $-\pi/2$ difference point

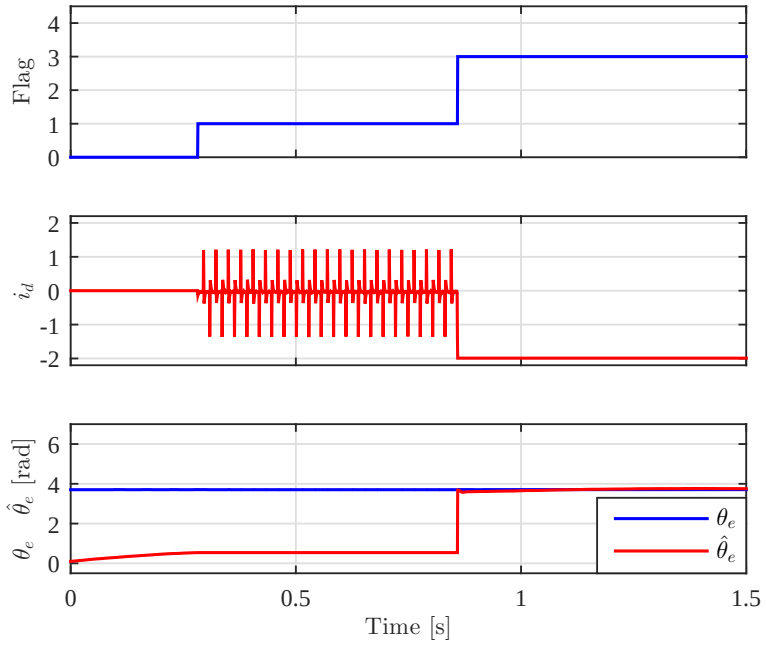

(b) Initial position converges to a π difference point (S pole)

Figure 5.21: Initial position estimation (a) $-\pi/2$ difference (b) π difference.

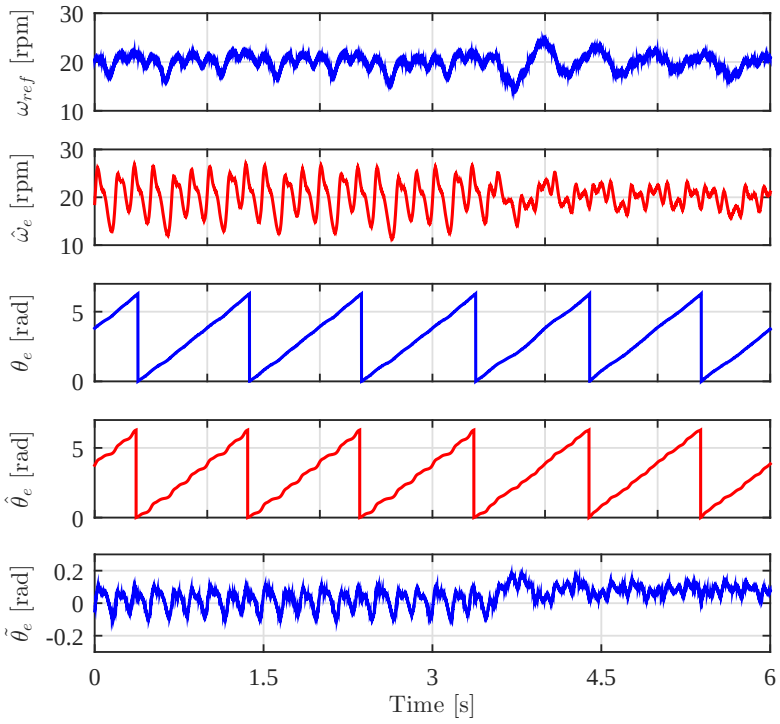

Figure 5.22: Sensorless closed-loop performance of without(0-3.5s) and with (3.5s-) ANF at 20 rpm with 50% rated load.

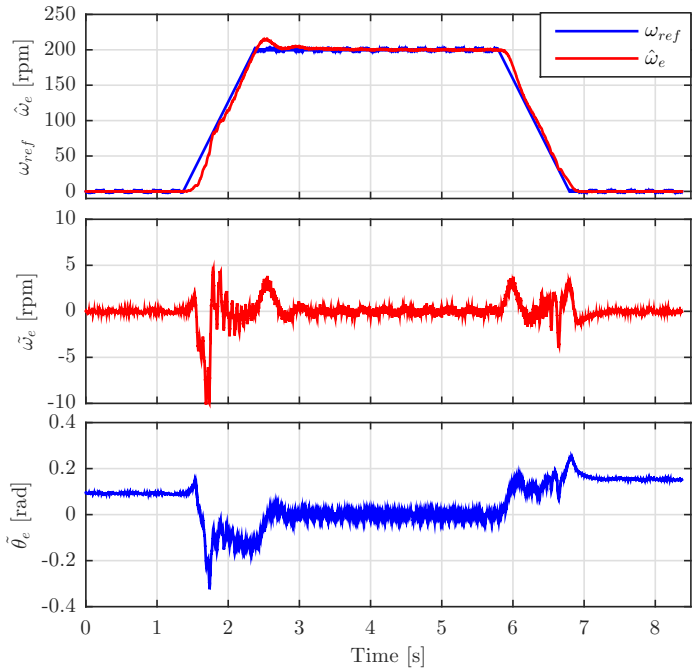

Figure 5.23: Sensorless closed-loop performance from 0 to 200 rpm without load.

(0.03pu) speed with a rated-load. The measured speed ω_e and position θ_e, the estimated speed $\hat{\omega}_e$ and position $\hat{\theta}_e$, the position error $\tilde{\theta}$ and q axis current i_q were presented in Fig. 5.24. The peak value of the position error of $\tilde{\theta}$ was less than 0.1 rad and the average value was almost zero. The test proved that the SST method has a comparable estimation performance with other traditional sensorless methods.

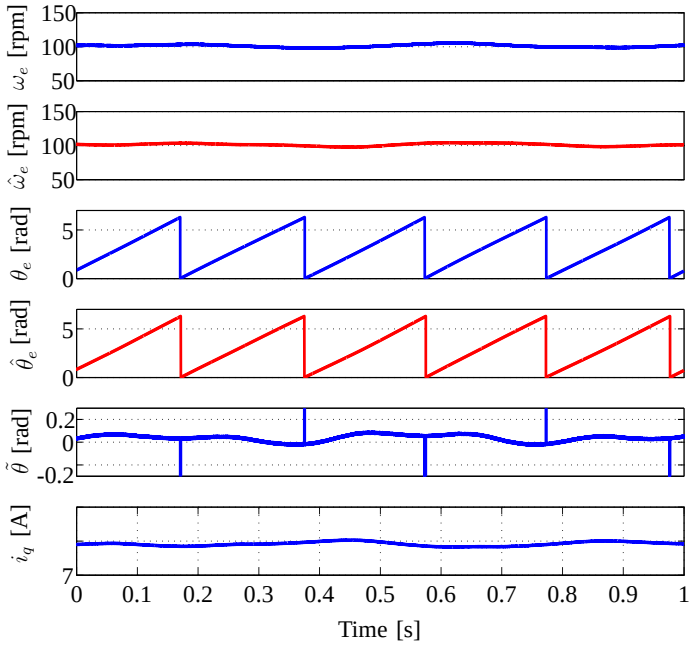

Figure 5.24: Sensorless closed-loop performance at 100 rpm speed with a rated load using the SST method.

Another system dynamic performance of the SST method was observed by implementing a low speed reverse test with a rated load. The speed reference varied from -100 rpm to 100 rpm. The rated load, produced by the load induction machine, kept the same direction for both speeds. The results were given in Fig. 5.25, which includes the same parameters as in Fig. 5.24. The highest $\tilde{\theta}$ is about 0.17 rad, while the mean error of $\tilde{\theta}$ at steady state is less than 0.07 rad.

5.3.3 Conclusion

This section proposed a secondary saliency tracking method for machines with strong multiple saliencies. The experimental investigation of the saliency behavior of the cwSPMSM has illustrated the possibility of utilizing a secondary saliency signal instead of the primary saliency signal for extracting rotor position information.

A specially designed BPF enhanced the estimation performance of the proposed SST method. It is convenient to be implemented in most existing digital controllers. Meanwhile, the initial position estimation is done by extending the $\pm$ d axis pulse excitation method to differentiate 4 convergence points. The proposed SST method shows accurate estimation results and is less sensitive to operation points.Theoretical analysis reveals that the proposed method is not restricted only for the cwSPMSM but can be applied to other AC machines.

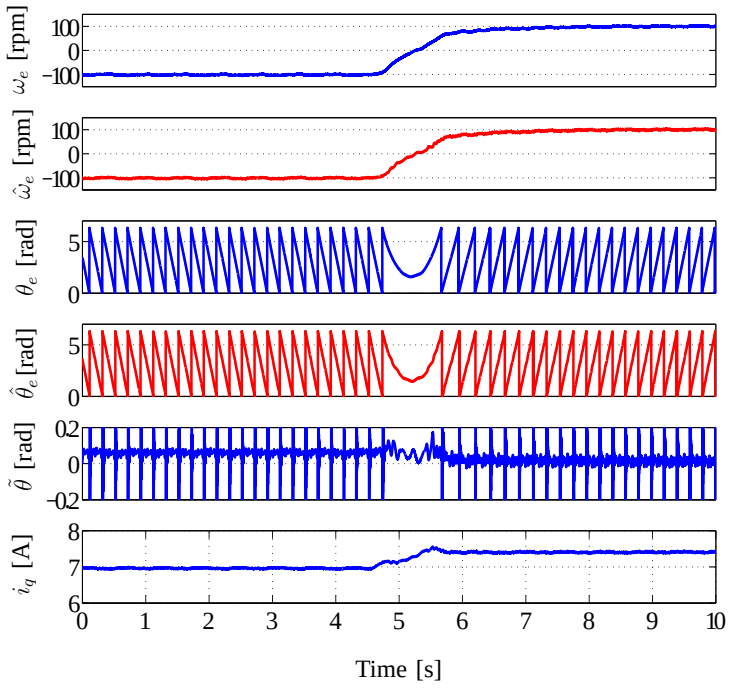

Figure 5.25: Sensorless closed-loop performance from -100 to 100 rpm with a rated load.

5.4 Repetitive control method

In this section, a novel Repetitive Control (RC) based sensorless control method, which is straightforward and machine parameters-independent, is proposed. The traditional RC method aims to solve the periodic control problem in a time domain but it can be extended to an angle domain. The concept of angle domain RC is applied to compensate the additional secondary saliency signal of a cwSPMSM which is a periodic function of the rotor angle [76]. The proposed RC is easy to implement and requires less computational effort compared with other methods based on the time domain. The proposed decoupling method is then applied to the cwSPMSM. The contributions of this method are addressed as follows:

- a novel RC method based on angle domain RC is proposed, and it is effective regardless of the saliency ratio;
- a nonlinear gain learning method is adopted to avoid the interference from strong noisy environments.

5.4.1 Repetitive control in time domain

The principle of RC originates from the internal model theory. That is, the controlled output can track a set of reference inputs without steady-state errors only if the model that generates these references is incorporated in the stable closed-loop system. For example, when the system is required to have a zero steady-state error to a step input, the model of the step function (1/s) should be also included in the loop gain. Similarly, if a periodic disturbance is injected into the

system, the controller itself also needs to generate the same periodic signal to compensate for it [77].

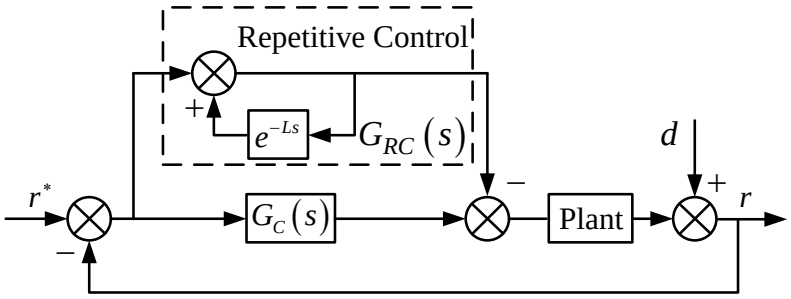

Figure 5.26: The structure of a Plug-in repetitive control.

The RC is usually implemented as a plug-in module to the primitive controller [78], shown in Fig. 5.26. In the presence of high periodic disturbance, the steady-state error can not be eliminated due to the limitation of the bandwidth of the regulator and the lack of a disturbance model in the closed-loop system. Therefore, the RC is inserted into the original control loop as a supplement to compensate the external periodic disturbance [77].

5.4.2 The design of RC in angle domain

For the cwSPMSM under test, although it is a surface-mounted permanent magnet type, it shows a remarkable saliency ratio by using the rotating HF signal injection method at standstill and low speed owning to its special stator windings, which has been demonstrated already in previous sections. In this section, the same demodulation as explained in Fig. 3.4 is adopted and its output NSC is

$$i_{dqc}^{cn} = I_{cn2} e^{j(2\theta_e + \varphi_2 - \pi/2)} + I_{cn4} e^{j(-4\theta_e + \varphi_4 - \pi/2)} \tag{5.29}$$

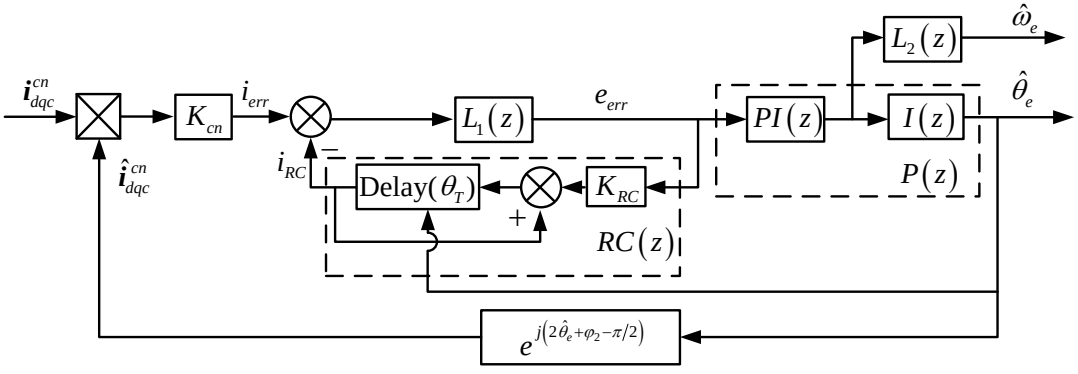

Figure 5.27: The proposed Plug-in repetitive control in an angle domain.

The error signal $\boldsymbol{i}_{err}$ is obtained by taking the cross-product between the measured current $\boldsymbol{i}_{dqc}^{cn}$ and the estimated current $\hat{\boldsymbol{i}}_{dqc}^{cn} = e^{j(2\hat{\theta}_e + \varphi_2 - \pi/2)}$, expressed as

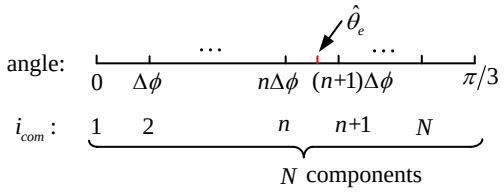

Figure 5.28: Realization of RC in the angle domain.

$$\boldsymbol{i}_{err} = K_{cn}\hat{\boldsymbol{i}}^{cn}_{dqc} \times \boldsymbol{i}^{cn}_{dqc} = I_{cn2}\sin(2(\theta_e - \hat{\theta}_e)) + \underbrace{I_{cn4}\sin(-4\theta_e - 2\hat{\theta}_e - \Delta\varphi)}_{d_{n6}} \tag{5.30}$$

where K_{cn} is a proportion parameter and can be taken into account in the magnitudes of I_{cn2} and I_{cn4}. When $\hat{\theta}_e$ tracks θ_e, the estimated position contains a 6th-order harmonic disturbance d_{n6} in (5.30) relative to the rotor electrical angle. Its period in angle domain is obtained as below

$$\theta_T = \frac{2\pi}{6} = \frac{\pi}{3} \tag{5.31}$$

where θ_T is a periodic constant in angle domain. Every time i_{err} is sampled together with $\hat{\theta}_e$. When $\hat{\theta}_e$ approaches θ_e, RC generates an output $\boldsymbol{i}_{RC}$ to approximate d_{n6}, which is then subtracted from the input of the PLL. Gradually, the 6th-order harmonic disturbance can be totally compensated by RC if the term i_{err} reaches zero.

The z-transfer function of RC, shown in Fig. 5.27, is given by

$$RC(z) = K_{RC}\frac{Z^{\theta_T}}{Z^{\theta_T} - F_1} \tag{5.32}$$

where the F_1 is a LPF which increases the stability of RC. To avoid the influence of the strong noise at steady states, an adaptive nonlinear gain $f(e)$ expressed in (5.33) is adopted inside the K_{RC}. When the error i_{err} is large, the gain is also large to accelerate the convergence and vice versa [79]. When the error is under the uncontrolled error limit, the gain becomes zero and learning process stops.

$$f_e \Rightarrow \begin{cases} 1 & |\boldsymbol{i}^{cn}_{err}| > \delta_2, \\ \frac{1}{\delta_2 - \delta}(|e| - \delta) & \delta < |\boldsymbol{i}^{cn}_{err}| < \delta_2, \\ 0 & |\boldsymbol{i}^{cn}_{err}| < \delta. \end{cases} \tag{5.33}$$

The gain K_{RC} is expressed as

$$K_{RC} = A \times f(e) \tag{5.34}$$

where A is the amplitude that regulates the speed of convergence.

In order to implement the proposed RC in a digital controller, a discrete RC should be designed. The angle period $\pi/3$ is divided into N components equally, shown in Fig. 5.28, and each component has a length of $\Delta\phi = \pi/(3N)$.

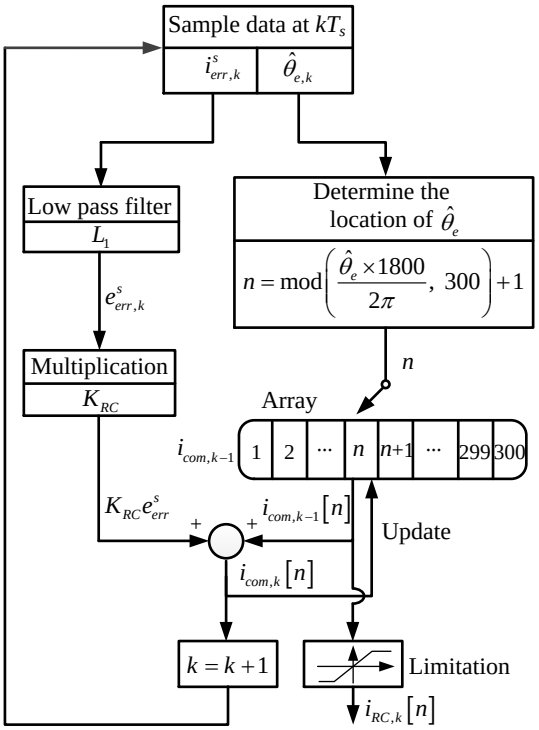

Figure 5.29: Flow chart of calculation of the proposed RC.

To describe the proposed RC more clearly, Fig. 5.29 shows detailed processes at kT_s. At every sampling instance, the calculations of the proposed RC consist of a one-order LPF, a modulo operator to determine the location of $\hat{\theta}_e$, a multiplication and an addition to update the storage array i_{com}. A limitation will restrict the output of RC.

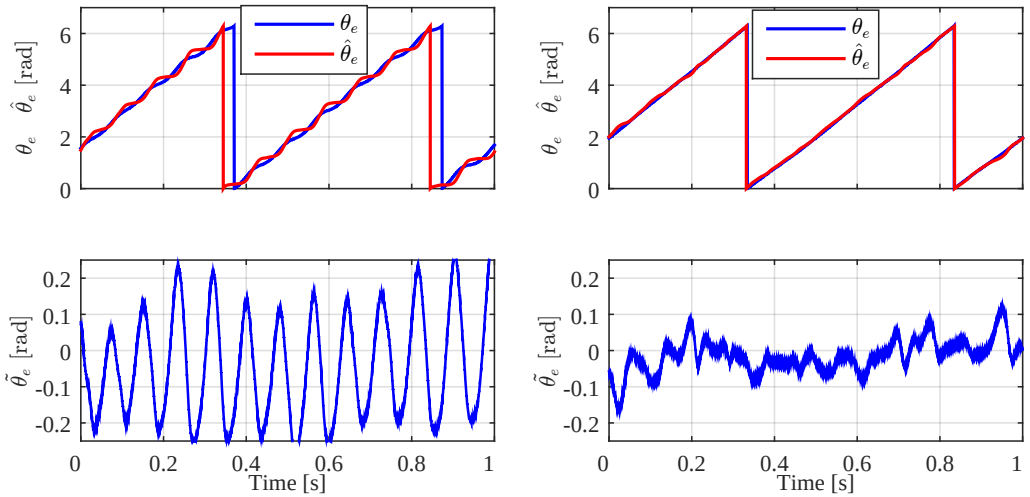

(a) PLL without proposed RC. (b) PLL with proposed RC.

Figure 5.30: Comparison of PLL without and with RC at 40 rpm.

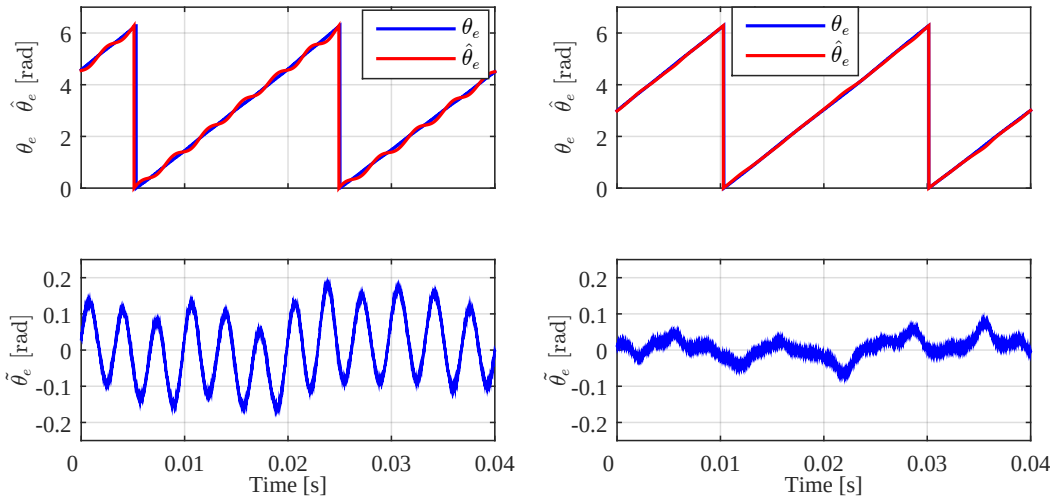

(a) PLL without proposed RC at 100 rpm. (b) PLL with proposed RC at 100 rpm.

Figure 5.31: Comparison of PLL without and with proposed RC at 100 rpm.

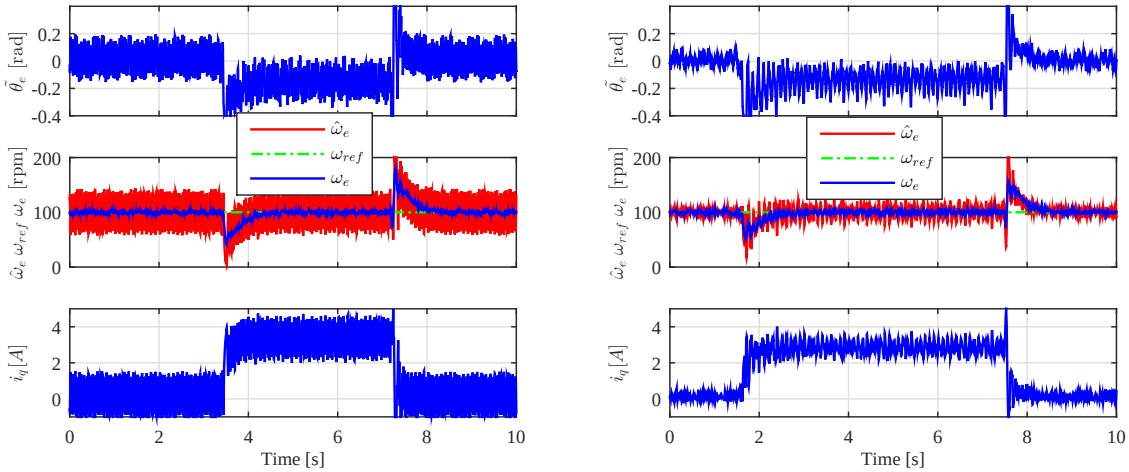

(a) PLL without proposed RC. (b) PLL with proposed RC.

Figure 5.32: Comparison of dynamic performance under step half rated torque at 100 rpm.

5.4.3 Implementation and experimental results

5.4.3.1 Application of the proposed RC

There are three steps to train RC. Firstly, the cwSPMSM runs with an encoder closed-loop control in order to reach a steady state. Secondly, the RC begins to learn based on its estimated position rather than the encoder provided position. After several periods of learning, the RC can generate an exact disturbance signal to compensate the existing one. Finally, the data of the generated disturbance signal is stored by the software. After the leaning process, the system can switch to the sensorless closed-loop control with an RC compensation.

The frequency and magnitude of the rotating HF voltage are 455 Hz and 10 V respectively.

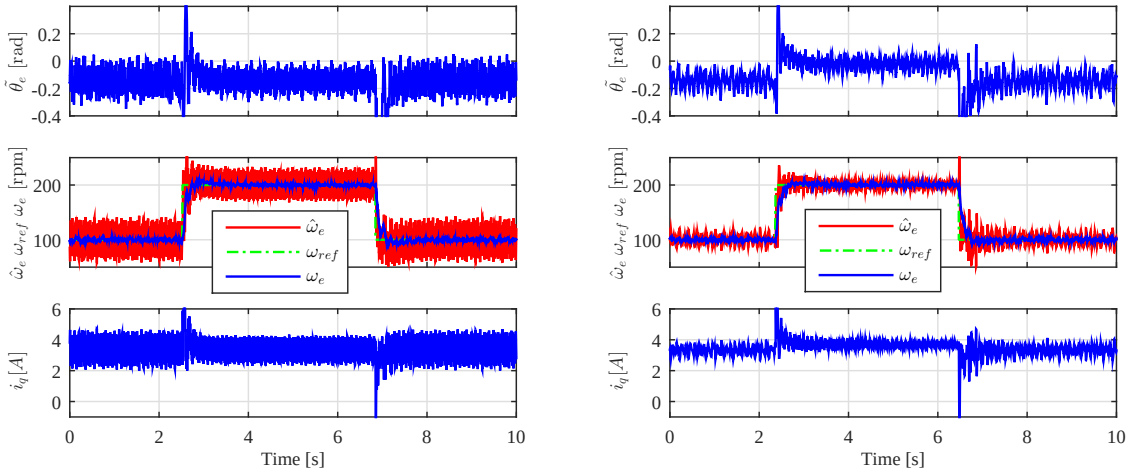

(a) PLL without proposed RC.

(b) PLL with proposed RC.

Figure 5.33: Comparison of dynamic performance under step speed change with half rated torque.

The parameters of the PLL are: $K_P = 600$, $K_I = 8000$, $K_{cn} = 0.26$. The cutoff frequency of L_1 is 27 Hz. $N = 300$ is selected in the experiments through trials. The RC gain K_{RC}, according to experimental adjustment, is set with 0.1 in the experiments. d-axis current reference is 3 A (to increase saliency ratio) and the motor operates under sensorless speed closed-loop control.

5.4.3.2 Experimental results

Position tracking performance of the PLL without (Fig. 5.30(a)) and with (Fig. 5.30(b)) RC at 40 rpm ($f_e = 2$ Hz) with half rated torque (about 3.6 Nm) is illustrated. It can be seen from Fig. 5.30(a) that both the real position and the estimated position contain a 6th-order harmonic (12 Hz). The magnitude of 6th-order harmonic is approximately 0.2 rad. After adopting the proposed method shown in Fig. 5.30(b), the real position and the estimated position become much smoother and the magnitude of 6th-order harmonic is near 0.

Fig. 5.31 shows the similar results as demonstrated in Fig. 5.30 but at 100 rpm ($f_e = 10$ Hz). The 6th-order harmonic (60 Hz) is also suppressed effectively.

Fig. 5.32 shows the results of using the PLL without RC (Fig. 5.32(a)) and with RC (Fig. 5.32(b)) under a step change of half rated torque at 100 rpm. Although the original PLL can track the step change, the estimated speed and current contain many harmonics in Fig. 5.32(a) due to the high ripple of the estimated position. By adopting the PLL with the proposed RC, the ripple of the estimated position, estimated speed, and q-axis current is reduced in Fig. 5.32(b).

The dynamic performance of the step speed change with half rated torque is shown in Fig. 5.33. When speed command steps from 100 rpm to 200 rpm are applied, using the proposed method, the estimated position, the estimated speed and the q-axis current shown in Fig. 5.33(b) (PLL with proposed RC) become more accurate than these in Fig. 5.33(a) (PLL without the proposed RC).

5.4.4 Conclusion

In this section, a novel repetitive control method is proposed to decouple the secondary saliency in sensorless controlled cwSPMSM drive. The method is parameter independent and requires less computational effort compared with the existing decoupling methods. Only the frequencies of multiple saliencies are needed, which can be easily acquired by advanced experimental analysis. This method is valid for all AC machines and can also be applied for machines with three or more saliencies with repetitive control in parallel mode. The application of this novel decoupling method is done with a cwSPMSM and the results validate its effectiveness.

5.5 Summary

In this chapter, three saliency based sensorless methods are proposed for solving the multiple-saliency problem of a cwSPMSM. They are Multi-Signal Injection method, Secondary Saliency Tracking method and Repetitive Control method. These methods view the problem from different perspectives but lead to the same destination. The MSI method is a combination method and it utilizes the frequency-dependent characteristic of saliency signals. On the contrary, the SST method is a decoupling method and it is realized based on the rotation difference of difference saliency signals and specially designed filters. The RC method is another decoupling method and it adaptively models the unwanted saliency signals that are periodical functions of rotor position. It is a general decoupling scheme and can be further extended to other similar situations.

CHAPTER 6

Fundamental model based sensorless method

In the previous Ch. 5, the saliency tracking based sensorless method has been introduced exclusively for the tested cwSPMSM at low speed and standstill. However, when the speed goes higher, it is mandatory to switch to a fundamental model based method that has lower energy consumption and higher accuracy. In other words, a hybrid scheme is the complete solution for the whole speed range sensorless control. In this section, three fundamental model based sensorless methods that are already introduced in Ch. 2 are comparatively investigated and experimentally verified for the higher speed range. They are the Model Reference Adaptive System (MRAS), Sliding Mode Observer (SMO) and Extended Kalman Filter (EKF).

6.1 Model reference adaptive system

The structure of MRAS has been described in Fig. 2.6 and the basic design principle is explained as well. We know there are various types of MRAS. In this section, a current-error based MRAS is chosen for the position and speed estimation.

(3.37) gives the matrix form of a PMSM model in the $d-q$ frame. It can be rewritten as

$$\frac{d}{dt}\begin{bmatrix} i_d \\ i_q \end{bmatrix} = \begin{bmatrix} -\frac{R_s}{L_d} & \omega_e \frac{L_q}{L_d} \\ -\omega_e \frac{L_d}{L_q} & -\frac{R_s}{L_q} \end{bmatrix} \begin{bmatrix} i_d \\ i_q \end{bmatrix} + \begin{bmatrix} \frac{1}{L_d} & 0 \\ 0 & \frac{1}{L_q} \end{bmatrix} \begin{bmatrix} u_d \\ u_q \end{bmatrix} + \begin{bmatrix} 0 \\ -\omega_e \frac{\psi_{\mathrm{PM}}}{L_q} \end{bmatrix}. \tag{6.1}$$

If we redefine the state variable as $\boldsymbol{x} = [x_1; x_2]$, input variables as $\boldsymbol{u} = [u_1; u_2]$ and output

variables as $\boldsymbol{y} = [y_1; y_2]$ for the system description [42],

$$\begin{aligned} \boldsymbol{x} &= \begin{bmatrix} x_1 \\ x_2 \end{bmatrix} = \begin{bmatrix} i_d + \frac{\psi_{\text{PM}}}{L_d} \\ i_q \end{bmatrix}, && (6.2) \\ \boldsymbol{u} &= \begin{bmatrix} u_1 \\ u_2 \end{bmatrix} = \begin{bmatrix} \frac{u_d}{L_d} + \frac{R_s \psi_{\text{PM}}}{L_d} \\ \frac{u_q}{L_q} \end{bmatrix}, && (6.3) \\ \boldsymbol{y} &= \begin{bmatrix} y_1 \\ y_2 \end{bmatrix} = \begin{bmatrix} \frac{L_d}{L_q} & 0 \\ 0 & \frac{L_q}{L_d}. \end{bmatrix} \begin{bmatrix} x_1 \\ x_2 \end{bmatrix}. && (6.4) \end{aligned}$$

The new system is adopted as the reference model (actually it is the machine itself and only the output $\boldsymbol{y}$ is useful for MRAS) and it can be describes as

$$\frac{d}{dt} \begin{bmatrix} x_1 \\ x_2 \end{bmatrix} = \begin{bmatrix} -\frac{R_s}{L_d} & \omega_e \frac{L_q}{L_d} \\ -\omega_e \frac{L_d}{L_q} & -\frac{R_s}{L_q} \end{bmatrix} \begin{bmatrix} x_1 \\ x_2 \end{bmatrix} + \begin{bmatrix} u_1 \\ u_2 \end{bmatrix} = A\boldsymbol{x} + \boldsymbol{u}. \tag{6.5}$$

The adjustable model containing the estimated $\hat{\omega_e}$ is exactly the same as the reference model. It is shown in

$$\begin{aligned} \frac{d}{dt} \begin{bmatrix} \hat{x}_1 \\ \hat{x}_2 \end{bmatrix} &= \begin{bmatrix} -\frac{R_s}{L_d} & \hat{\omega_e} \frac{L_q}{L_d} \\ -\hat{\omega_e} \frac{L_d}{L_q} & -\frac{R_s}{L_q} \end{bmatrix} \begin{bmatrix} \hat{x}_1 \\ \hat{x}_2 \end{bmatrix} + \begin{bmatrix} u_1 \\ u_2 \end{bmatrix} = \hat{A}\hat{\boldsymbol{x}} + \boldsymbol{u}, \\ \hat{\boldsymbol{y}} &= \begin{bmatrix} \hat{y}_1 \\ \hat{y}_2 \end{bmatrix} = \begin{bmatrix} \frac{L_d}{L_q} & 0 \\ 0 & \frac{L_q}{L_d} \end{bmatrix} \begin{bmatrix} \hat{x}_1 \\ \hat{x}_2 \end{bmatrix}. \end{aligned} \tag{6.6}$$

The principle of the MRAS observer is to compare the outputs of the adaptive model and reference model and then use a mechanism to make them equal to each other. The estimation error of the state variable $\boldsymbol{e}$ and the output $\boldsymbol{\varepsilon}_y$ are determined by

$$\begin{aligned} \boldsymbol{e} &= \boldsymbol{x} - \hat{\boldsymbol{x}} = \begin{bmatrix} i_d + \frac{\psi_{\text{PM}}}{L_d} \\ i_q \end{bmatrix} - \begin{bmatrix} \hat{i}_d + \frac{\psi_{\text{PM}}}{L_d} \\ \hat{i}_q \end{bmatrix} = \begin{bmatrix} i_d - \hat{i}_d \\ i_q - \hat{i}_q \end{bmatrix}, \\ \boldsymbol{\varepsilon}_y &= \boldsymbol{y} - \hat{\boldsymbol{y}} = \begin{bmatrix} \frac{L_d}{L_q} & 0 \\ 0 & \frac{L_q}{L_d} \end{bmatrix} \begin{bmatrix} x_1 - \hat{x}_1 \\ x_2 - \hat{x}_2 \end{bmatrix} = \begin{bmatrix} \frac{L_d}{L_q} & 0 \\ 0 & \frac{L_q}{L_d} \end{bmatrix} \boldsymbol{e}. \end{aligned} \tag{6.7}$$

Then the estimation error dynamics is given by

$$\frac{d}{dt}\boldsymbol{e} = A\boldsymbol{x} - \hat{A}\hat{\boldsymbol{x}} = A\boldsymbol{x} - \hat{A}\hat{\boldsymbol{x}} + A\hat{\boldsymbol{x}} - A\hat{\boldsymbol{x}} = A\boldsymbol{e} + (A - \hat{A})\hat{\boldsymbol{x}} = A\boldsymbol{e} + \boldsymbol{\rho}. \tag{6.8}$$

The goal is to make the estimation error converge to zero. In this case, when the hyper-stability criterion

$$\eta(0, t_1) = \int_0^{t_1} \boldsymbol{\varepsilon}_y^{\mathrm{T}} \boldsymbol{\rho}\, dt \geq -\gamma_0^2 \qquad . \qquad ; \gamma_0 > 0 \tag{6.9}$$

$$\begin{aligned} \eta(0, t_1) &= \int_0^{t_1} \boldsymbol{\varepsilon}_y^{\mathrm{T}} \boldsymbol{\rho}\, dt = \int_0^{t_1} \boldsymbol{\varepsilon}_y^{\mathrm{T}} (A - \hat{A})\hat{\boldsymbol{x}}\, dt = \int_0^{t_1} \boldsymbol{\varepsilon}_y^{\mathrm{T}} (A - \hat{A})\hat{\boldsymbol{x}} \frac{\omega_e - \hat{\omega_e}}{\omega_e - \hat{\omega_e}}\, dt = \\ &= \int_0^{t_1} \boldsymbol{\varepsilon}_y^{\mathrm{T}} A_{\text{er}} \hat{\boldsymbol{x}} (\omega_e - \hat{\omega_e})\, dt \geq -\gamma_0^2 \qquad ; \gamma_0 > 0. \end{aligned} \tag{6.10}$$

is fulfilled [38], the MRAS is stable and the estimation goal can be achieved. Usually, this can be guaranteed by applying a PI type controller

$$\hat{\omega_e} = K_{\mathrm{I}} \int_0^{t_1} \boldsymbol{\varepsilon}_y^{\mathrm{T}} A_{\mathrm{er}} \hat{\boldsymbol{x}}\, dt + K_{\mathrm{P}} \cdot \boldsymbol{\varepsilon}_y^{\mathrm{T}} A_{\mathrm{er}} \hat{\boldsymbol{x}} + \hat{\omega}_e(0). \tag{6.11}$$

Substituting (6.3) into (6.11), we get

$$\begin{aligned} \hat{\omega_e} \;\; = \;\; & K_{\mathrm{I}} \int_0^{t_1} \left[i_d \hat{i}_q - i_q \hat{i}_d - \frac{\psi_{\mathrm{PM}}}{L_d} (i_q - \hat{i}_q) \right] dt \\ & + K_{\mathrm{P}} \cdot \left[i_d \hat{i}_q - i_q \hat{i}_d - \frac{\psi_{\mathrm{PM}}}{L_d} (i_q - \hat{i}_q) \right] + \hat{\omega}_k(0). \end{aligned} \tag{6.12}$$

The rotor position can be estimated by integrating the estimated speed

$$\hat{\theta_e} = \int_0^{t_1} \hat{\omega_e}\, dt + \hat{\theta}(0). \tag{6.13}$$

6.2 Sliding mode observer

The SMO is widely used because of its simple algorithm and robustness. The general structure of an SMO has been shown in Fig. 2.9. In this section, because an $\alpha - \beta$ frame based SMO will be introduced, the original PMSM model in this frame is derived by substituting (3.23)-(3.24) into (3.22) and shown as

$$\begin{aligned} L_s \frac{di_\alpha}{dt} &= u_\alpha - R_s i_\alpha - e_\alpha, \\ L_s \frac{di_\beta}{dt} &= u_\beta - R_s i_\beta - e_\beta, \\ e_\alpha &= -\psi_{\mathrm{PM}} \omega_e \mathrm{sin}\theta_e, \\ e_\beta &= \psi_{\mathrm{PM}} \omega_e \mathrm{cos}\theta_e, \end{aligned} \tag{6.14}$$

where $L_s = L_\alpha = L_\beta = L_d = L_q$ since an SPMSM is considered only in this work.

The SMO for the position and speed estimations is demonstrated as

$$\begin{aligned} L_s \frac{d\widehat{i}_\alpha}{dt} &= u_\alpha - R_s \widehat{i}_\alpha - kF(\widehat{i}_\alpha - i_\alpha), \\ L_s \frac{d\widehat{i}_\beta}{dt} &= u_\beta - R_s \widehat{i}_\beta - kF(\widehat{i}_\beta - i_\beta), \\ \hat{e}_\alpha &= kF(\widehat{i_\alpha} - i_\alpha), \\ \hat{e}_\beta &= kF(\widehat{i_\beta} - i_\beta), \end{aligned} \tag{6.15}$$

where k is a constant and F(x) is the switch function. In a traditional SMO, the switch function *sign* is commonly used. However, it causes chattering problems. To avoid this problem, an improved SMO is proposed in [80] and presented in this section. The switch function is replaced by a *sigmoid* function, which is shown as

$$F(x) = [\frac{2}{1 + e^{-ax}}] - 1, \tag{6.16}$$

where a is a constant.

Comparing (6.15) with (6.14), it is clear that the back EMF terms e_α and e_β can be estimated by the $kF(\widehat{i_\alpha} - i_\alpha)$ and $kF(\widehat{i_\beta} - i_\beta)$, respectively. However, these estimates contain HF ripples and can not be applied directly for position calculation. Thus, another back EMF observer is further proposed in [80] to solve this problem. It is described as

$$\begin{aligned}
\frac{d\widehat{e}_\alpha}{dt} &= -\widehat{\omega}\widehat{e}_\beta - l(\widehat{e}_\alpha - e_\alpha), \\
\frac{d\widehat{e}_\beta}{dt} &= -\widehat{\omega}\widehat{e}_\alpha - l(\widehat{e}_\beta - e_\beta), \\
\frac{d\widehat{\omega}_e}{dt} &= (\widehat{e}_\alpha - e_\alpha)\widehat{e}_\beta - (\widehat{e}_\beta - e_\beta)\widehat{e}_\alpha, \\
\widehat{\theta} &= -arctan(\frac{\widehat{e}_\alpha}{\widehat{e}_\beta}).
\end{aligned} \tag{6.17}$$

where l is the observer gain. The stability of both observers, SMO and back EMF, can be found in [80]. In this work, the introduced SMO serves only as a standard SMO example for comparison.

6.3 Extended Kalman filter

EKF is an optimal recursive estimator, which can be used for estimating the states of nonlinear systems [81]. The general structure of the EKF has been presented in Fig. 2.8. The system state equations are expressed as

$$\begin{aligned}
\dot{x}(t) &= f[x(t)] + \mathbf{B}u(t) + w(t), \\
y(t) &= \mathbf{C}x(t) + v(t).
\end{aligned} \tag{6.18}$$

where $w(t)$ and $v(t)$ are system noise and measurement noise with covariance $\mathbf{Q}(t)$ and $\mathbf{R}(t)$, respectively. $u(t)$ and $y(t)$ are the input and output variables, respectively. The initial state vector $x(t_0)$ is expressed as a Gaussian random vector with covariance P_0. $\mathbf{B}$ is the input matrix and $\mathbf{C}$ is the output matrix. $f(x)$ is the system transition function.

In a digital controller, the system state equations should be converted from a continuous form to a discrete form. Therefore, the discrete state equations are derived as

$$\begin{aligned}
x_k &= f(x_{k-1}) + \mathbf{B}u_{k-1} + w_{k-1} \\
y_k &= \mathbf{C}x_k + v_k
\end{aligned} \tag{6.19}$$

where the subscript k and $k-1$ represent the k-th and (k-1)th instance, respectively. Other symbol definitions are the same as (6.18)

The EKF algorithm contains two steps: a prediction step and an innovation step. The prediction step performs a prediction of the state vector $x_{k/k-1}$ and the error covariance matrix $\mathbf{P}$ based on previous estimates $x_{k-1/k-1}$. It is described as

$$\begin{aligned}
x_{k/k-1} &= x_{k-1/k-1} + f[x_{k-1/k-1}, u(k-1)]T_s \\
\mathbf{P}_{k/k-1} &= \mathbf{J}_{k-1}\mathbf{P}_{k-1/k-1}\mathbf{J}_{k-1}^T + \mathbf{Q},
\end{aligned} \tag{6.20}$$

where $f[x_{k-1/k-1}, u(k-1)] = f[x_{k-1/k-1}] + \mathbf{B}u(k-1)$, and the Jacobian matrix is defined as $\mathbf{J}_{k-1} = \frac{\partial x_{k/k-1}}{\partial x_{k-1/k-1}}$. $\mathbf{P}$ and $\mathbf{Q}$ denote the error covariance matrix and the system noise matrix respectively. T_s is the sampling period.

The innovation step updates and corrects the predicted state estimate $x_{k/k-1}$ and the covariance matrix $\mathbf{P}$. It is represented by

$$\begin{aligned} x_{k/k} &= x_{k/k-1} + \mathbf{K}_k(y_k - \mathbf{C}x_{k/k-1}) \\ \mathbf{P}_{k/k} &= \mathbf{P}_{k/k-1} - \mathbf{K}_k\mathbf{C}\mathbf{P}_{k/k-1}, \end{aligned} \tag{6.21}$$

where the EKF gain is defined as $\mathbf{K}_k = \mathbf{P}_{k/k-1}\mathbf{C}^T(\mathbf{C}\mathbf{P}_{k/k-1}\mathbf{C}^T + \mathbf{R})^{-1}$.

In order to estimate the rotor position and speed, the $\alpha - \beta$ frame based machine model is chosen. The corresponding matrices are

$$u_k = \begin{bmatrix} u_\alpha & u_\beta \end{bmatrix}^T \tag{6.22}$$

$$x_k = \begin{bmatrix} \hat{i}_\alpha & \hat{i}_\beta & \hat{\omega}_e & \hat{\theta}_e \end{bmatrix}^T \tag{6.23}$$

$$y_k = \begin{bmatrix} \hat{i}_\alpha & \hat{i}_\beta \end{bmatrix}^T \tag{6.24}$$

$$\mathbf{B} = \begin{bmatrix} \frac{1}{\hat{L}_s} & 0 \\ 0 & \frac{1}{\hat{L}_s} \\ 0 & 0 \\ 0 & 0 \end{bmatrix} \tag{6.25}$$

$$\mathbf{C} = \begin{bmatrix} 1 & 0 & 0 & 0 \\ 0 & 1 & 0 & 0 \end{bmatrix} \tag{6.26}$$

$$f(x,u) = \begin{bmatrix} -\frac{R_s}{L_s}\hat{i}_\alpha + \frac{\hat{\omega}_e\psi_{PM}}{L_s}\sin\hat{\theta}_e + \frac{1}{L_s}u_\alpha \\ -\frac{R_s}{L_s}\hat{i}_\beta - \frac{\hat{\omega}_e\psi_{PM}}{L_s}\cos\hat{\theta}_e + \frac{1}{L_s}u_\beta \\ 0 \\ \hat{\omega}_e \end{bmatrix} \tag{6.27}$$

$$\mathbf{J} = \begin{bmatrix} 1-\frac{R_s}{L_s}T_s & 0 & \frac{\psi_{PM}}{L_s}\sin\hat{\theta}_e T_s & \frac{\psi_{PM}}{L_s}\hat{\omega}_e\cos\hat{\theta}_e T_s \\ 0 & 1-\frac{R_s}{L_s}T_s & -\frac{\psi_{PM}}{L_s}\cos\hat{\theta}_e T_s & \frac{\psi_{PM}}{L_s}\hat{\omega}_e\sin\hat{\theta}_e T_s \\ 0 & 0 & 1 & 0 \\ 0 & 0 & T_s & 1 \end{bmatrix}. \tag{6.28}$$

The initial values of $\mathbf{P}$, $\mathbf{Q}$ and $\mathbf{R}$ are chosen as

$$P = \begin{bmatrix} 0.01 & 0 & 0 & 0 \\ 0 & 0.01 & 0 & 0 \\ 0 & 0 & 200 & 0 \\ 0 & 0 & 0 & 10 \end{bmatrix} \tag{6.29}$$

$$Q = \begin{bmatrix} 0.02 & 0 & 0 & 0 \\ 0 & 0.02 & 0 & 0 \\ 0 & 0 & 400 & 0 \\ 0 & 0 & 0 & 0.2 \end{bmatrix} \tag{6.30}$$

$$R = \begin{bmatrix} 0.2 & 0 \\ 0 & 0.2 \end{bmatrix} \tag{6.31}$$

6.4 Theoretical comparison of MRAS, SMO and EKF

In previous sections, the implementations of MRAS, SMO and EKF are introduced. The theoretical comparison of these three estimation methods is performed in this section so as to demonstrate their similarity as well as their difference. They are listed in Table 6.1

Feature	MRAS	SMO	EKF
Coordinate	$d-q$	$\alpha-\beta$	$\alpha-\beta$
Convergence	Popov	Lyapunov	Lyapunov
Computation effort	Middle	Simple	High
Initial values	-	-	$\mathbf{P}$ $\mathbf{Q}$ $\mathbf{R}$
Tuning parameters	$K_{\mathrm{P}}, K_{\mathrm{I}}$	k, l	-

Table 6.1: Theoretical comparison of MRAS, SMO and EKF.

6.5 Experimental comparison

6.5.1 Estimation accuracy and limitation

The speed step and load step experimental results of all the three sensorless control methods are given in Fig. 6.1 and Fig. 6.2, respectively. The ω_e, $\hat{\omega}_e$, $\tilde{\omega}_e$ and $\tilde{\theta}_e$ are shown in each figure. The machine parameters used in each method are the same and they are listed in Table C.3.

From Fig. 6.1 and Fig. 6.2, it can be observed that the EKF shows the best performance in both dynamic state and steady state among these three methods. The position estimation error $\tilde{\theta}_e$ of the SMO is the biggest and that of MRAS is in the middle.

The minimal speed at which the observer still works is experimentally detected. The corresponding values are listed in Table 6.2

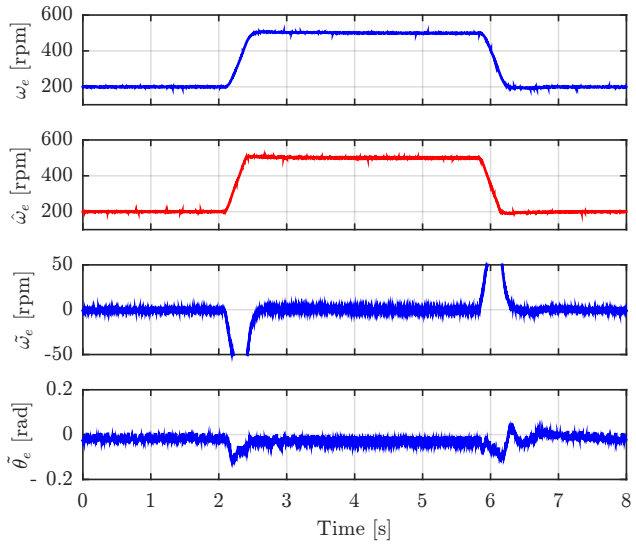

(a) Speed step performance of MRAS

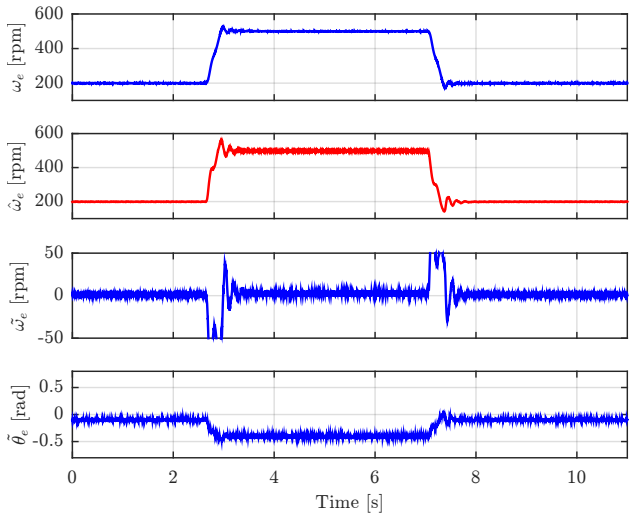

(b) Speed step performance of SMO

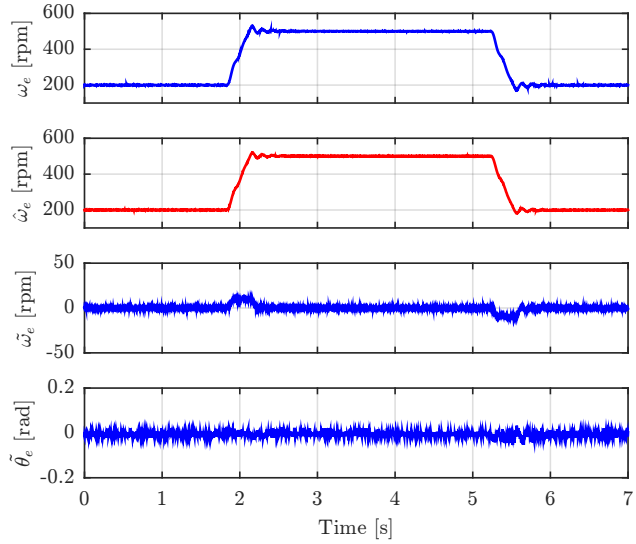

(c) Speed step performance of EKF

Figure 6.1: Speed step performance comparison (200 rpm-500 rpm-200 rpm).

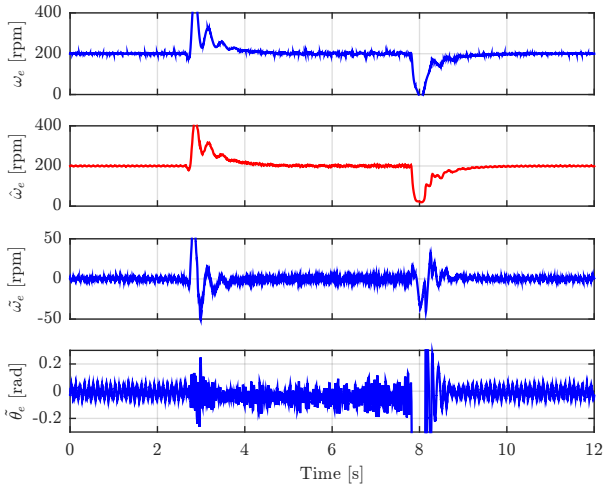

(a) Load step performance of MRAS

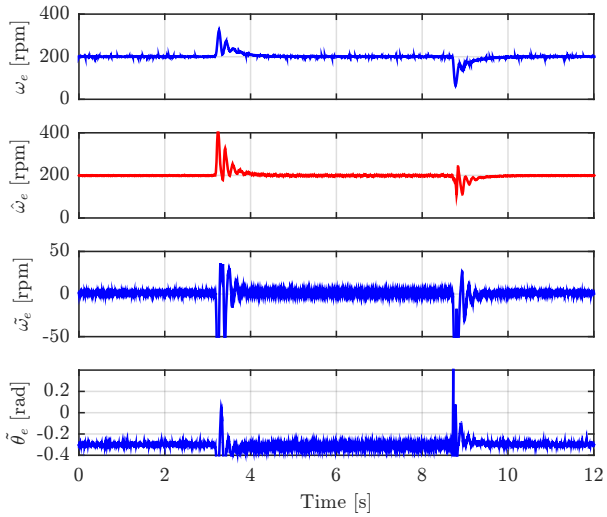

(b) Load step performance of SMO

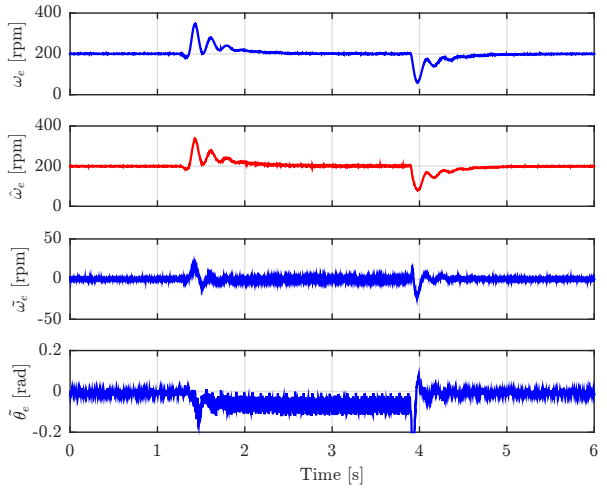

(c) Torque step performance of EKF

Figure 6.2: Torque step performance comparison (0 N.m-7 N.m-0 N.m).

Observer	$\omega_e[\mathrm{rpm}]\,\vert T_m = 0\,\mathrm{Nm}$	$\omega_e[\mathrm{rpm}]\,\vert T_m = 1\,\mathrm{Nm}$
MRAS	100	150
SMO	100	160
EKF	80	100

Table 6.2: Minimal Speed.

6.5.2 Parameter dependence and comparison overview

In order to detect the parameter tolerance range of these sensorless methods, the parameter dependence tests are done by varying the respective parameter value form 50% to 150%. The criteria is to check if the position estimation error is within the area of [-0.2 rad, 0.2 rad]. The experimental results are listed in Table 6.3

Observer	ΔR_s	ΔL_s	$\Delta \Psi_{\mathrm{PM}}$
MRAS	0,5 - 1,3	0,5 - 1,5	0,5 - 1,0
SMO	0,5 - 1,1	0,7 - 1,1	-
EKF	0,5 - 1,5	0,5 - 1,5	0,5 - 1,5

Table 6.3: Observers' parameter dependence range.

Finally, an overview of a comprehensive comparison is given in Table 6.4. It shows that the EKF has the best performance among these three observers but it consumes the most resources of the digital controller. The other two observers that bring less calculation burden to the controller demonstrate similar behavior.

Experiment	MRAS	SMO	EKF
tracking overshoot	large	middle	small
tracking accuracy	good	good	good
minimal speed	high	high	low
parameter dependence	robust	sensitive	very robust
speed reversal	good	bad	good
anti-noise ability	high	low	high

Table 6.4: Overview of experimental comparison.

6.6 Hybrid sensorless control

To perform a smooth transition between the saliency tracking based method and the fundamental model based method, a hybrid scheme should be adopted. The estimated position angle is obtained with a linear combination of results. The switching strategy is the same with [37]. Particularly, when the transition is from high speed to low speed, the estimated position signal $\hat{\theta}_{e1}$ from the saliency tracking based method should be corrected by $\hat{\theta}_{e2}$ from the fundamental

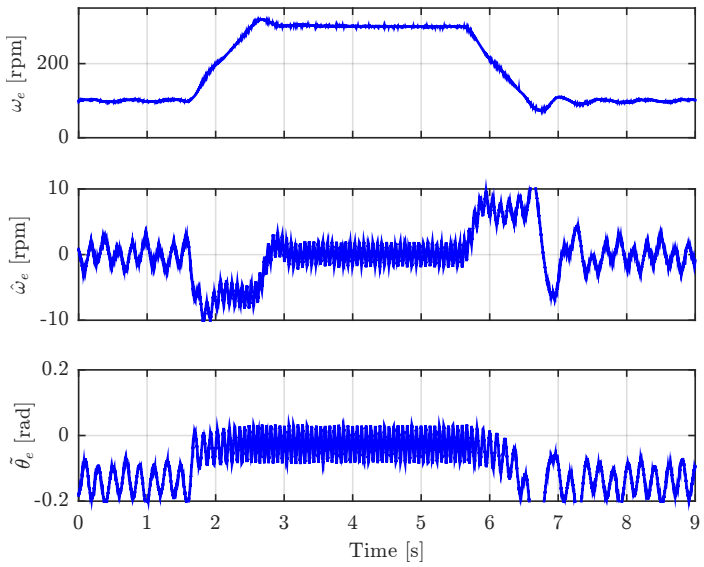

Figure 6.3: Hybrid sensorless control performance SST+MRAS, transition region 200 rpm-250 rpm.

model based method on account of its uncertainty of polarity information. Afterward, the control system will turn to the saliency tracking based method. A successful experimental result is illustrated in Fig. 6.3 combining the MSI method and MRAS method.

6.7 Summary

In this chapter, three fundamental model based sensorless methods are introduced as necessary supplements to the proposed saliency based sensorless methods in Ch. 5, which is only appropriate for the low speed range and at standstill. They are Model Reference Adaptive System, Sliding Mode Observer and Extended Kalman Filter. The design procedures of each observer are introduced in detail. In addition, the theoretical and experimental comparisons are summarized in respective tables. They reveal that the EKF shows the best estimation performance among the mentioned three methods at the cost of increasing calculation burden of the controller. The choice of the fundamental model based methods is highly application-requirement-dependent. Finally, a hybrid sensorless control scheme is introduced in this chapter and the transition performance is satisfactory.

CHAPTER 7

Multi-parameter identification

For the implementation of the sensorless PMSM control in the middle and high speed range, fundamental-model based methods are intensively investigated and applied in industry products. However, an obvious drawback of these methods is the high dependence on the accuracy of the machine parameters. Fortunately, two popular parameter estimators, MRAS and EKF, can remedy this disadvantage. In this chapter, the multi-parameter estimation for these two estimators is theoretically analyzed and experimentally compared in an identical sensorless controlled PMSM drive where an improved Active Flux Observer (AFO) is proposed for the rotor position and speed estimation. The AFO exchanges mutually the estimated parameters with MRAS or EKF. The corresponding issues like identifiability of parameter, inverter non-linearity compensation, steady and dynamic performance of both estimators are discussed. Finally, the comparative studies are verified by experimental results.

7.1 Introduction

In the fundamental model based sensorless observer, machine electrical parameters (e.g., the stator resistance R_s, rotor permanent flux ψ_{PM} and inductance L_s) are usually treated as constant values regardless of the operation point. In reality, however, they change with the load, temperature and saturation. As a result, the on-line [50, 51] or off-line [47, 48] parameter estimation becomes necessary so as to make the system itself adaptive to parameter variation. Moreover, the parameter estimation is more important for a fault prediction/detection or system health monitoring [82] in the application of PMSMs like aerospace, remote control. Thus, the parameter estimation can strengthen the robustness of the system especially in a sensorless controlled PMSM drive system. The existing parameter estimation methods were usually verified by comparing the estimated value with its nominal value. However, they were not applied adaptively in the controller to further validate its effectiveness. Moreover, in most existing publications, only a single parameter estimation was verified in the sensorless controller. The

multi-parameter estimation is still a suspending problem needed to be evaluated. In this chapter, two popular on-line multi-parameter estimators are theoretically analyzed and experimentally compared in the sensorless controlled PMSM drive to demonstrate their advantages and disadvantages. The conclusions are beneficial for choosing an appropriate parameter estimator in a specified application.

The structure of MRAS is demonstrated in Fig. 7.1(a). Note that, although Fig. 7.1(a) and Fig. 7.1(b) look the same as Fig. 2.6 and Fig. 2.8, they estimate different parameters: R_s, ψ_{PM} and L_s. The applications of MRAS can be found in [52, 55, 56] where different adaptive controllers were adopted taking advantage of the flexibility of the MRAS design principle. Particularly in [55], a hybrid sensorless method combining an MRAS and an alternating HF signal injection (HFSI) method was proposed for the PMSM. The estimation error signal ϵ generated by the alternating HFSI method was brought into the adaptive controller of the MRAS as an auxiliary correction factor when the speed of the PMSM was low. The R_s and ψ_{PM} were estimated separately in a different speed range. In [56], another similar parameter estimation scheme for the PMSM was proposed as well: θ_e and R_s estimation at low speed range, θ_e and ψ_{PM} estimation at higher speed range. In [83], two MRAS were connected to estimate ψ_{PM}, R_s and θ_e of the PMSM simultaneously. One of them was in charge of ψ_{PM}, R_s estimation and the other for θ_e estimation. These two MRAS exchanged bidirectionally their outputs in each step. The experimental results, however, were not provided to verify the effectiveness of the interconnected MRAS system. The parameter identifiability that is paramount for defining the test condition was not mentioned in all previous mentioned papers.

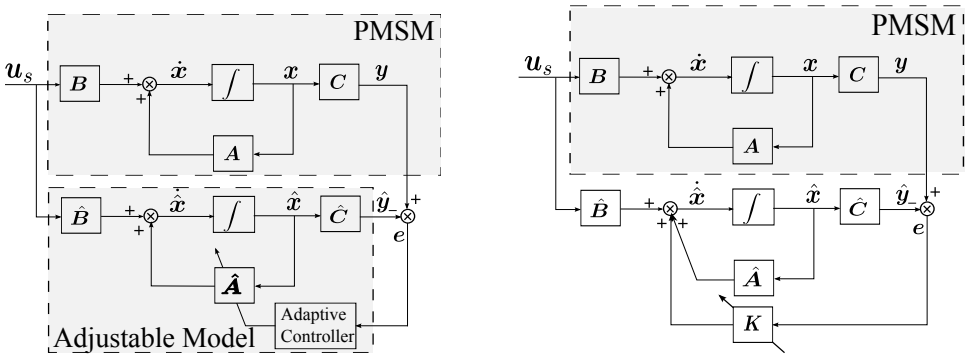

(a) MRAS observer. (b) EKF observer.

Figure 7.1: Observer structures of MRAS and EKF.

The other on-line parameter estimator is the EKF, whose structure is illustrated in Fig. 7.1(b) as well. Comparing Fig. 7.1(a) with Fig. 7.1(b), the difference between these two parameter estimators is obvious. The estimator gain matrix K of the EKF is adaptively calculated at each step, while the adaptive controller of the MRAS is normally realized by a fixed PI controller. The EKF based parameter estimator can be found in [42,52–54]. Especially in [54], two kinds of EKF, the current based or stator flux based EKF were analyzed and listed in a table considering different state variables, which gave a comprehensive introduction to the possibilities of EKF in the parameter estimation of PMSMs. However, the estimation results of the EKF in the papers mentioned above were not applied in practice to validate their effectiveness.

In order to validate the effectiveness of the estimated results form both MRAS and EKF, an

improved Active Flux Observer is designed for sensorless control of a PMSM. The AFO is in charge of the position and speed estimation and it exchanges mutually the estimated parameters with MRAS or EKF. The steady state and dynamic performance of parameter estimations in the sensorless controlled PMSM drive are experimentally verified. The multi-parameter identifiability and compensation of the non-linearity of the inverter have been discussed in this chapter as well.

7.2 System description

Fig. 7.2 is the detailed version of Fig. 5.1 and shows the detailed structure of a sensorless FOC controlled PMSM system. It utilizes the AFO to estimated $\hat{\theta}_e$ and $\hat{\omega}_e$. As demonstrated in Fig. 7.2, MRAS and EKF are adopted to estimate the L_s, R_s and ψ_{PM}, which are required parameters in the AFO. Meanwhile, the $\hat{\theta}_e$ and $\hat{\omega}_e$ estimated by the AFO are fed to the MRAS or EKF.

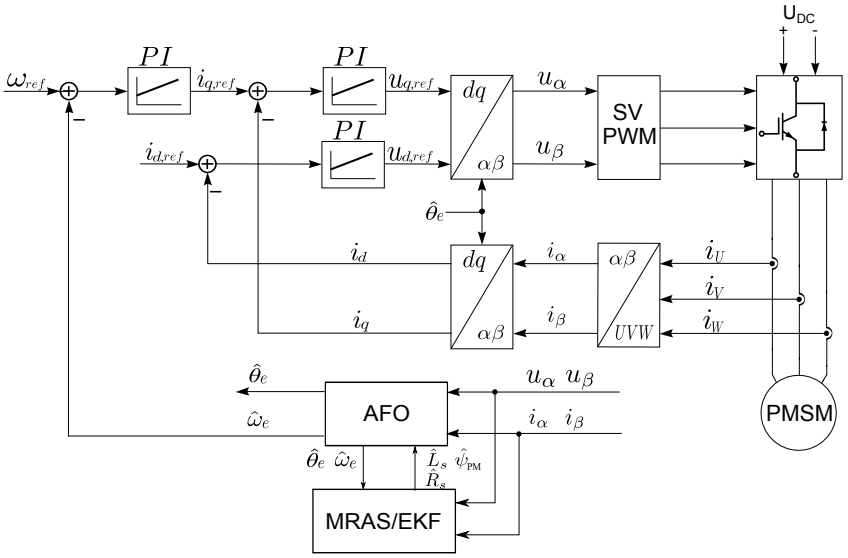

Figure 7.2: Overview of a sensorless PMSM control system.

7.3 Parameter estimation

In order to make the sensorless control system more adaptive to the variation of machine parameters, the aforementioned two on-line estimators MRAS and EKF are comparatively investigated in the existing sensorless PMSM drive employing the AFO.

Firstly, the parameter identifiability of a PMSM is discussed and the prerequisite for the simultaneous multi-parameter estimation is summarized as well. Secondly, the multi-parameter identification theory and the detailed mathematical calculation procedures of each estimator are introduced. Finally, the theoretical comparison between MRAS and EKF is performed, which is beneficial for choosing an appropriate estimator in specific situation.

7.3.1 Identifiability

The extended dq-axis equations of the PMSM considering parameter variation are expressed as

$$\begin{aligned}
\frac{di_d}{dt} &= -\frac{R_s}{L_s}i_d + \omega_e i_q + \frac{1}{L_s}u_d \\
\frac{di_q}{dt} &= -\frac{R_s}{L_s}i_q - \omega_e i_d + \frac{1}{L_s}u_q - \omega_e\frac{\psi_{PM}}{L_s} \\
\frac{dR_s}{dt} &\cong 0 \\
\frac{dL_s}{dt} &\cong 0 \\
\frac{d\psi_{\text{PM}}}{dt} &\cong 0.
\end{aligned} \tag{7.1}$$

We assume that the parameters change slowly compared with the current (unsaturated condition). As a result, only the first two equations in (7.1) are independent and can be used actually for parameter estimation.

In order to analyze the parameter identifiability, the dq-axis steady state equations can be further derived from (7.1) as (7.2) considering only the measurable quantities i_d, i_q with discrete time index

$$\begin{aligned}
u_d(k) &= R_s i_d(k) - L_s\omega_e(k)i_q(k) \\
u_q(k) &= R_s i_{q(k)} + L_s\omega_e(k)i_d(k) + \psi_{PM}\omega_e(k),
\end{aligned} \tag{7.2}$$

where k represents the k-th time instance in the control system.

Owing to the rank-deficient problem of the PMSM's state equations, the multi-parameter (≥ 3) estimation is impossible and a maximum of two parameters are simultaneously identifiable [84, 85]. Moreover, some further conclusions can be made:

- If $i_d = 0$ control is applied for the control of a SPMSM, it worsens further the rank-deficient problem and makes the simultaneous estimation of R_s and ψ_{PM} impossible.

- If $i_q = 0$ (without load), the simultaneous estimation of L_s and ψ_{PM} is impossible as well. Moreover, if the speed ω_e of the PMSM is low and without load, only R_s is identifiable.

- The accurate estimation of R_s and L_s can be done only when $i_d \neq 0$, $i_q \neq 0$ and ω_e is high enough.

It is clear that any two parameters can be simultaneously estimated only if specific conditions are satisfied. Therefore, a selection has to be made according to the demand of the particular control system. The aforementioned identifiability is valid for all parameter estimators and should be respected.

To solve the rank-deficient problem for multi-parameter estimation, a variety of approaches is presented [84–86]. Basically, they all need to excite an additional i_d or i_q at such period when the estimator works. In this chapter, $i_{d,ref} = 1$ is set only for L_s and ψ_{PM} estimation.

7.3.2 Parameter estimation based on MRAS

The main idea of the MRAS estimator is to design an adaptive algorithm based on the Popov criterion. First, the equations of a PMSM (7.1) containing only measurable quantities i_d, i_q are expressed as a state-space model,

$$\dot{\mathbf{x}} = \mathbf{A}\mathbf{x} + \mathbf{B}\mathbf{u} + \mathbf{C}\mathbf{w}, \tag{7.3}$$

where $\mathbf{x} = \begin{bmatrix} i_d \\ i_q \end{bmatrix}$, $\mathbf{u} = \begin{bmatrix} u_d \\ u_q \end{bmatrix}$, $\mathbf{w} = \begin{bmatrix} 0 \\ -\omega_e \end{bmatrix}$,

$\mathbf{A} = \begin{bmatrix} -a & \omega_e \\ -\omega_e & -a \end{bmatrix}$, $\mathbf{B} = \begin{bmatrix} b & 0 \\ 0 & b \end{bmatrix}$, $\mathbf{C} = \begin{bmatrix} 0 & 0 \\ 0 & c \end{bmatrix}$,

$a = \frac{R_s}{L_s}$, $b = \frac{1}{L_s}$, $c = \frac{\psi_{PM}}{L_s}$.

The adjustable model is exactly the same as (7.3) but replaces the measured and unknown parameters with the estimated ones. The adjustable model is described as

$$\dot{\hat{\mathbf{x}}} = \hat{\mathbf{A}}\hat{\mathbf{x}} + \hat{\mathbf{B}}\mathbf{u} + \hat{\mathbf{C}}\mathbf{w}, \tag{7.4}$$

where $\hat{\mathbf{x}} = \begin{bmatrix} \hat{i}_d \\ \hat{i}_q \end{bmatrix}$, $\mathbf{u} = \begin{bmatrix} u_d \\ u_q \end{bmatrix}$, $\mathbf{w} = \begin{bmatrix} 0 \\ -\omega_e \end{bmatrix}$,

$\mathbf{A} = \begin{bmatrix} -\hat{a} & \omega_e \\ -\omega_e & -\hat{a} \end{bmatrix}$, $\mathbf{B} = \begin{bmatrix} \hat{b} & 0 \\ 0 & \hat{b} \end{bmatrix}$, $\mathbf{C} = \begin{bmatrix} 0 & 0 \\ 0 & \hat{c} \end{bmatrix}$,

$\hat{a} = \frac{\hat{R}_s}{\hat{L}_s}$, $\hat{b} = \frac{1}{\hat{L}_s}$, $\hat{c} = \frac{\hat{\psi}_{PM}}{\hat{L}_s}$. Note that the ω_e is measured through an encoder and assumed known.

The error between i_d, i_q and $\hat{i}_d$, $\hat{i}_q$ can be described as:

$$\mathbf{e} = \mathbf{x} - \hat{\mathbf{x}} = \begin{bmatrix} e_d \\ e_q \end{bmatrix} = \begin{bmatrix} i_d - \hat{i}_d \\ i_q - \hat{i}_q \end{bmatrix}. \tag{7.5}$$

Summarizing the work presented in [87,88], the adaptive algorithm for the estimation of each parameter can be obtained as

$$\frac{\hat{R}_s}{\hat{L}_s} = \frac{R_{s0}}{L_{s0}} - K_1 \int_0^t (e_d\hat{i}_d + e_q\hat{i}_q)\, dt - K_2(e_d\hat{i}_d + e_q\hat{i}_q) \tag{7.6}$$

$$\frac{1}{\hat{L}_s} = \frac{1}{L_{s0}} + K_3 \int_0^t (e_d u_d + e_q u_q)\, dt + K_4(e_d u_d + e_q u_q) \tag{7.7}$$

$$\frac{\hat{\psi}_{PM}}{\hat{L}_s} = \frac{\psi_{PM0}}{L_{s0}} - K_5 \int_0^t e_q\omega_e\, dt - K_6 e_q\omega_e \tag{7.8}$$

where K_1, K_3, K_5 and K_2, K_4, K_6 are proportional and integral gains, respectively. $R_{s0}, L_{s0}, \psi_{PM0}$ represent the initial values of respective parameters, which are set with their nominal values in experiments.

When the estimated parameters $\frac{\hat{R}_s}{\hat{L}_s}$, $\frac{1}{\hat{L}_s}$ and $\frac{\hat{\psi}_{PM}}{\hat{L}_s}$ are obtained, the individual $\hat{R}_s$, $\hat{L}_s$ and $\hat{\psi}_{PM}$ can be acquired as well. Note that, as explained in the previous section, only two parameters are

simultaneously identifiable and the rest of the parameters should be set with its nominal value. Moreover, the 6 PI parameters are really hard to tune at the same time. Thus, the selection of estimated parameters has to be made for MRAS as well.

7.3.3 Parameter estimation based on EKF

The implementation of the EKF has been introduced in Ch. 6. The EKF can be extended to estimate R_s, L_s or ψ_{PM} instead of $\hat{\theta}_e$ and $\hat{\omega}_e$. Similar to the MRAS method, the selection of parameters should be made to fulfill the criteria of identifiability. Consequently, three estimation types are selected and the respective calculation equations are given in detail.

In this section, contrary to Ch. 6, the $d-q$ frame is chosen for implementing the EKF. Note that, in all the selected estimation schemes, there are three matrices in common

$$y_k = \begin{bmatrix} i_d & i_q \end{bmatrix}^T \tag{7.9}$$

$$\mathbf{B} = \begin{bmatrix} \frac{1}{\hat{L}_s} & 0 \\ 0 & \frac{1}{\hat{L}_s} \\ 0 & 0 \\ 0 & 0 \end{bmatrix} \tag{7.10}$$

$$\mathbf{C} = \begin{bmatrix} 1 & 0 & 0 & 0 \\ 0 & 1 & 0 & 0 \end{bmatrix}. \tag{7.11}$$

7.3.3.1 Resistance and inductance estimation

$$x_k = \begin{bmatrix} i_d & i_q & \hat{R}_s & \frac{1}{\hat{L}_s} \end{bmatrix}^T \tag{7.12}$$

$$f(x,u) = \begin{bmatrix} -\frac{\hat{R}_s}{\hat{L}_s} i_d + \omega_e i_q + \frac{1}{\hat{L}_s} u_d \\ -\frac{\hat{R}_s}{\hat{L}_s} i_q - \omega_e i_d + \frac{1}{\hat{L}_s} u_q - \omega_e \frac{\psi_{PM}}{\hat{L}_s} \\ 0 \\ 0 \end{bmatrix} \tag{7.13}$$

$$\mathbf{J} = \begin{bmatrix} 1-\frac{\hat{R}_s}{\hat{L}_s}T_s & \omega_e T_s & -\frac{i_d}{\hat{L}_s}T_s & (-\hat{R}_s i_d + u_d)T_s \\ -\omega_e T_s & 1-\frac{\hat{R}_s}{\hat{L}_s}T_s & -\frac{i_q}{\hat{L}_s}T_s & (-\hat{R}_s i_q + u_q - \omega_e \psi_{PM})T_s \\ 0 & 0 & 1 & 0 \\ 0 & 0 & 0 & 1 \end{bmatrix} \tag{7.14}$$

7.3.3.2 Resistance and PM flux estimation

$$x_k = \begin{bmatrix} i_d & i_q & \hat{R}_s & \hat{\psi}_{PM} \end{bmatrix}^T \tag{7.15}$$

$$f(x,u) = \begin{bmatrix} -\frac{\hat{R}_s}{L_s} i_d + \omega_e i_q + \frac{1}{L_s} u_d \\ -\frac{\hat{R}_s}{L_s} i_q - \omega_e i_d + \frac{1}{L_s} u_q - \omega_e \frac{\hat{\psi}_{PM}}{L_s} \\ 0 \\ 0 \end{bmatrix} \tag{7.16}$$

$$\mathbf{J} = \begin{bmatrix} 1-\frac{\hat{R}_s}{L_s} T_s & \omega_e T_s & -\frac{i_d}{L_s} T_s & 0 \\ -\omega_e T_s & 1-\frac{\hat{R}_s}{L_s} T_s & -\frac{i_q}{L_s} T_s & -\frac{\omega_e}{L_s} T_s \\ 0 & 0 & 1 & 0 \\ 0 & 0 & 0 & 1 \end{bmatrix} \tag{7.17}$$

7.3.3.3 Inductance and PM flux estimation

$$x_k = \begin{bmatrix} i_d & i_q & \frac{1}{\hat{L}_s} & \hat{\psi}_{PM} \end{bmatrix}^T \tag{7.18}$$

$$f(x,u) = \begin{bmatrix} -\frac{R_s}{\hat{L}_s} i_d + \omega_e i_q + \frac{1}{\hat{L}_s} u_d \\ -\frac{R_s}{\hat{L}_s} i_q - \omega_e i_d + \frac{1}{\hat{L}_s} u_q - \omega_e \frac{\hat{\psi}_{PM}}{\hat{L}_s} \\ 0 \\ 0 \end{bmatrix} \tag{7.19}$$

$$\mathbf{J} = \begin{bmatrix} 1-\frac{R_s}{\hat{L}_s} T_s & \omega_e T_s & (-R_s i_d + u_d) T_s & 0 \\ -\omega_e T_s & 1-\frac{R_s}{\hat{L}_s} T_s & (-R_s i_q + u_q - \omega_e \hat{\psi}_{PM}) T_s & -\frac{\omega_e}{\hat{L}_s} T_s \\ 0 & 0 & 1 & 0 \\ 0 & 0 & 0 & 1 \end{bmatrix} \tag{7.20}$$

7.3.4 Theoretical comparison of MRAS and EKF

In previous sections, the implementations of both MRAS and EKF are introduced. The theoretical comparison of both estimators is performed in this section so as to demonstrate their similarities as well as differences.

- The goal of the error minimization of output signals and the feedback compensation structure for both estimators are the same.
- The MRAS aims for the parameter estimation of a deterministic linear system and it does not take system noise and measurement noise into consideration. By contrast, the EKF commits itself to a stochastic non-linear system and is an optimum estimation in noisy environment.
- The stability and convergence rate of MRAS is determined by Popov's or Lyapunov's theory and the adaptive mechanism is usually replaced by a PI type controller with fixed gains. On the contrary, the gain matrix $\mathbf{K}$ is updated adaptively in the EKF and plays a substantial role in the convergence rate of the estimator.
- The calculation burden of the EKF is obviously higher than that of the MRAS. Therefore, the EKF requires higher-performance digital controller to implement in practice.

7.4 Inverter nonlinearity

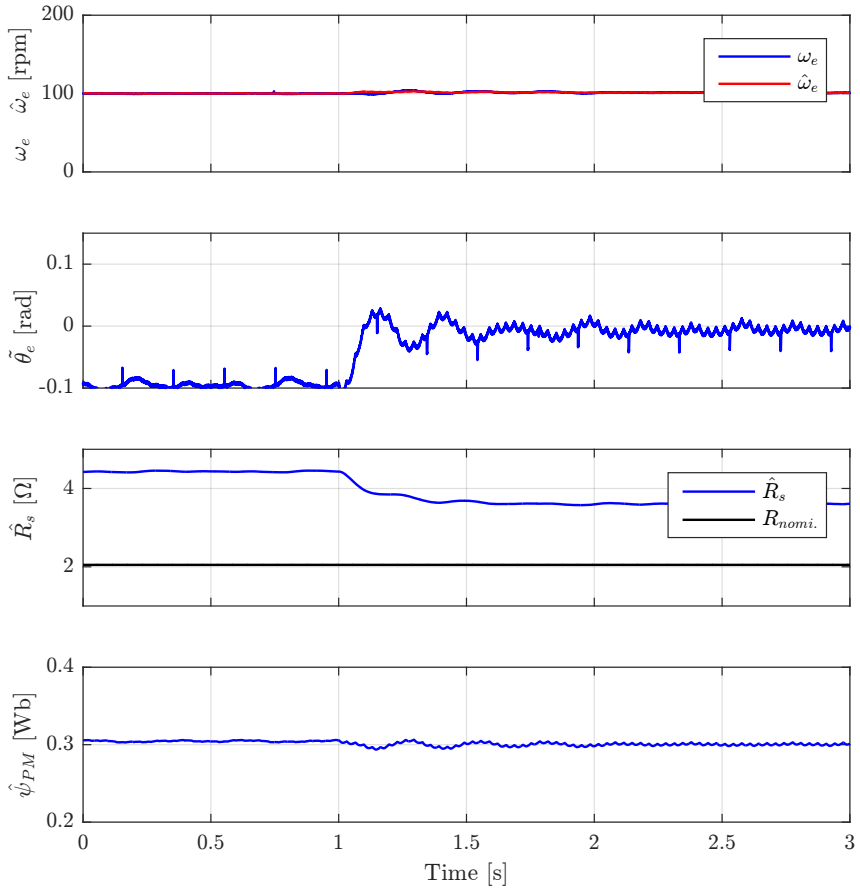

Figure 7.3: Sensorless performance with $\hat{R}_s$ and $\hat{\psi}_{PM}$ estimation based on EKF. No load, 100 rpm, without (0-1s) and with (1s-) compensation of inverter non-linearity.

In the practical implementation, the current signals are sampled by current sensors while the reference voltage signals instead of real measured voltage signals are used as inputs to the parameter estimator. Consequently, the estimated parameters have discrepancy with the nominal values if the inverter non-linearity (e.g.,dead time, switching delay, IGBT's voltage drop and the parasitic capacitance) influence is not considered. Accordingly, in order to provide a better performance of the control system, some previous work has investigated the compensation of the inverter nonlinearity [89–92].

Based on the research of [90, 92], the inverter non-linearity compensation model can be evaluated as

$$\begin{aligned} u_a &= u_{a0} + u_{comp-inv}(2\text{sign}(i_a) - \text{sign}(i_b) - \text{sign}(i_c)) \\ u_b &= u_{b0} + u_{comp-inv}(-\text{sign}(i_a) + 2\text{sign}(i_b) - \text{sign}(i_c)) \\ u_c &= u_{c0} + u_{comp-inv}(-\text{sign}(i_a) - \text{sign}(i_b) + 2\text{sign}(i_c)), \end{aligned} \tag{7.21}$$

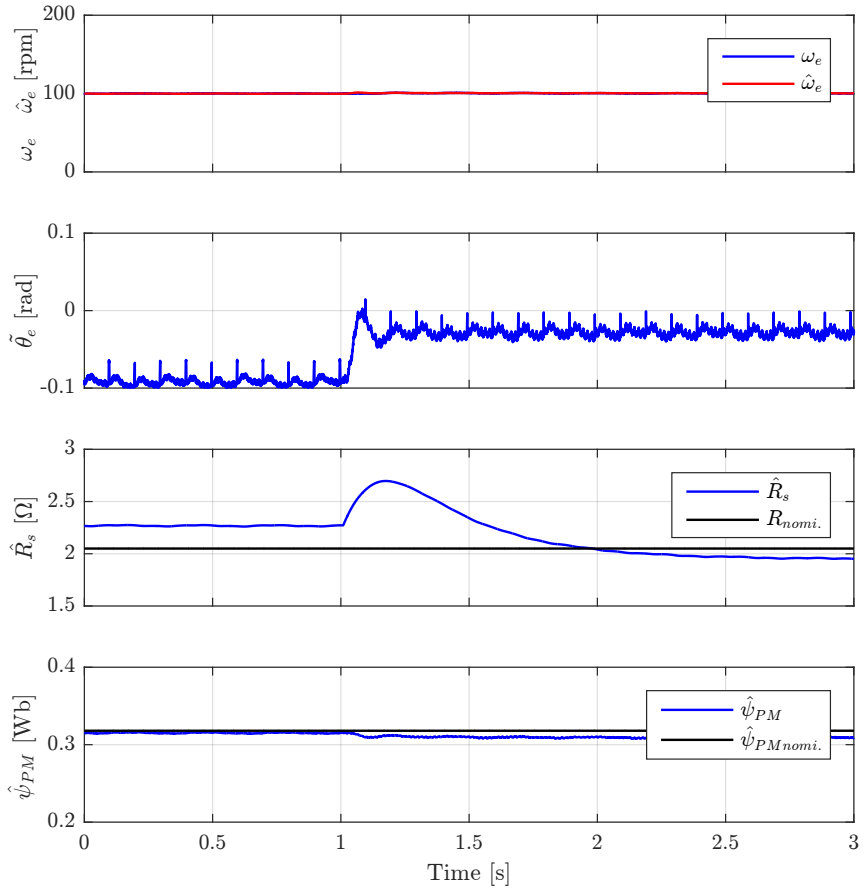

Figure 7.4: Sensorless performance with $\hat{R}_s$ and $\hat{\psi}_{PM}$ estimation based on MRAS. No load, 100 rpm, without (0-1s) and with (1s-) compensation of inverter non-linearity.

with

$$\text{sign}(i) = \begin{cases} 1, & i \geq 0 \\ -1, & i < 0 \end{cases}. \tag{7.22}$$

The output voltages from the VSI and the reference voltages are represented by u_a, u_b, u_c and u_{a0}, u_{b0}, u_{c0}, respectively. $u_{comp-inv}$ indicates the compensation voltage, which is given by

$$u_{comp-inv} = V_{dc}\frac{t_{comp}}{T_{PWM}} \tag{7.23}$$

where V_{dc} is the dc link voltage and T_{PWM} is the period of the PWM. t_{comp} indicates the compensated time, which is obtained by the dead time of the inverter. In the experiments performed the values of these parameters were: $V_{dc} = 582V$, $t_{comp} = 0.8\mu s$ and $T_{PWM} = 125\mu s$.

The compensation works not only for parameter estimators but also for the AFO and it can further improve the control performance especially in the low speed range.

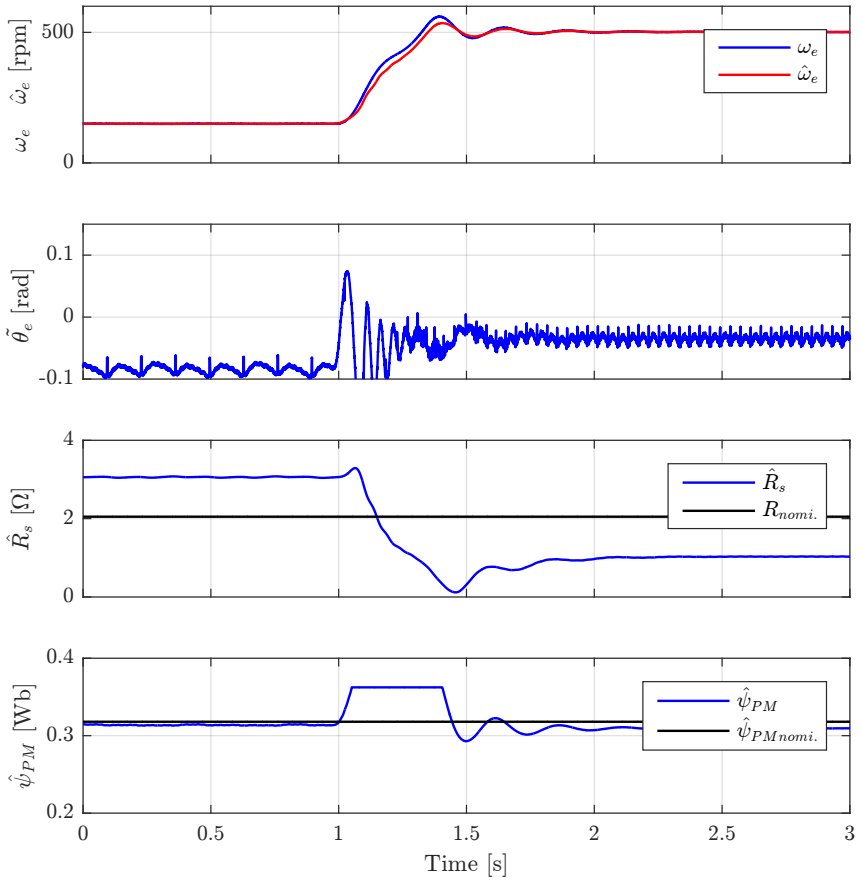

Figure 7.5: Sensorless performance with $\hat{R}_s$ and $\hat{\psi}_{PM}$ estimation based on EKF. No load, with compensation, speed changes from 150rpm to 500rpm.

7.5 Experimental results

The online parameter identification based on the EKF as well as MRAS are done in the sensorless closed-loop control. And then, the experimental comparison is given and the corresponding remarks are summarized.

7.5.1 Sensorless control with resistance and PM flux estimation

Sensorless control with parameter estimation using EKF and MRAS at 100 rpm (0.03p.u.) in steady state are illustrated in Fig. 7.3 and Fig. 7.4, respectively. The estimated rotor speed $\hat{\omega_e}$ and measured speed ω_e together with the position estimation error $\tilde{\theta}_e$ are shown in the figures. The difficulty of multi-parameter estimation is in the low speed range with a small load, because in this case, the measured u_d, u_q, i_d, i_q are quite small in (7.2) and the non-linearity effect of the inverter is comparatively significant. In this chapter, only lower speed range results are given. When the speed goes higher and with heavy load, the estimation performance becomes better. The nominal values of R_s, ψ_{PM} and L_s are **2.07Ω, 0.31778Wb and 14.2mH**. respectively.

EKF and MRAS were utilized separately to estimate $\hat{R}_s$ and $\hat{\psi}_{\text{PM}}$. In the AFO, L_s was set with its nominal value 14.4mH. As can be seen in Fig. 7.3 and Fig. 7.4, from 0s to 1s,

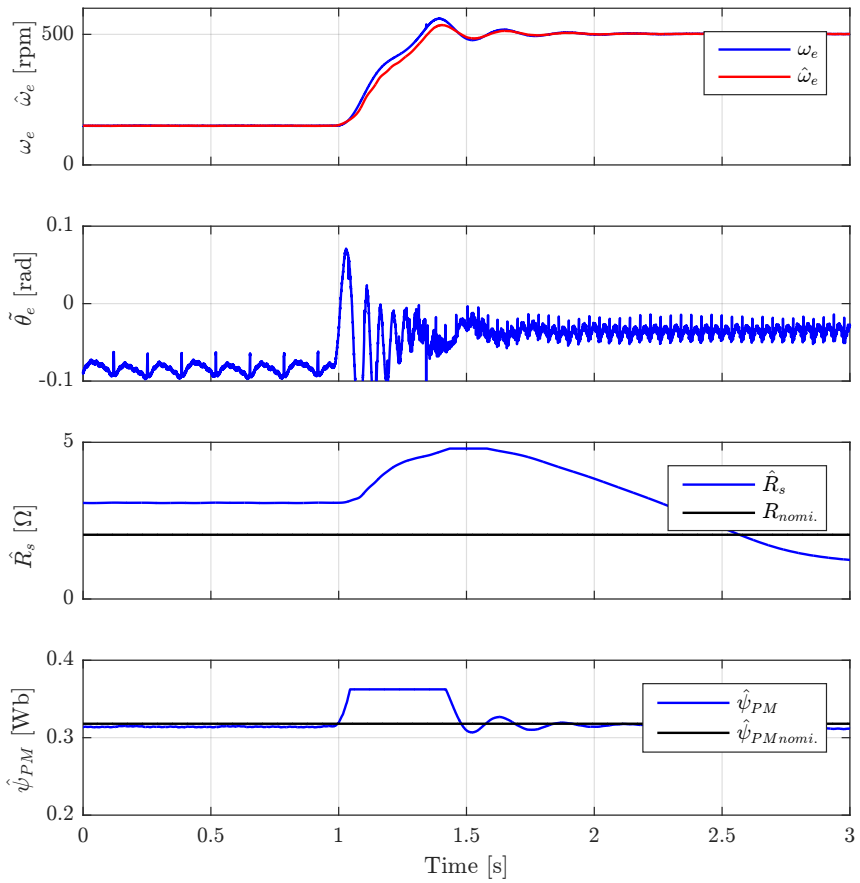

Figure 7.6: Sensorless performance with $\hat{R}_s$ and $\hat{\psi}_{PM}$ estimation based on MRAS. No load, with compensation, speed changes from 150rpm to 500rpm.

the compensation of dead-time was disabled and the position estimation error $\tilde{\theta}_e$ for EKF and MRAS were 0.12 rad and 0.1 rad, respectively. From 1s on, the same compensation scheme was enabled and $\tilde{\theta}_e$ decreased to 0.02 (EKF) and 0.04 (MRAS), respectively. The $\hat{R}_s$ resulting from the EKF (4.5 Ω) before inverter non-linearity compensation was comparatively higher than that of MRAS (2.2 Ω) and the nominal value 2.07 Ω. So was the $\hat{R}_s$ of EKF after compensation. The $\hat{\psi}_{\text{PM}}$ estimated from both EKF and MRAS had very similar values even in the transient state. It is clear that the effect of inverter non-linearity must be considered at very low speed ranges and especially for resistance estimation using the EKF method.

The speed step tests were done for both EKF and MRAS to demonstrate their dynamic behavior. The respective results are shown in Fig. 7.5 and Fig. 7.6. At 1s, the speed command altered from 150 rpm to 500 rpm. The $\tilde{\theta}_e$ and $\hat{\psi}_{\text{PM}}$ for both estimators showed similar results. Note that, all estimated quantities must be limited in order to avoid the unstable area during the transient states, which can be observed in the $\hat{\psi}_{\text{PM}}$ between 1s and 1.5s. The convergence rate of the estimation of $\hat{R}_s$ resulting from EKF was faster than that of MRAS. In addition, the estimation of $\hat{R}_s$ by both estimators converged automatically to its nominal value with the increase of the speed regardless of the dead-time compensation. That is because when the speed is very low and without any load (i.e., back EMF terms $L_s\omega_e(k)i_q(k)$ and $L_s\omega_e(k)i_d(k)$ in (7.2) are

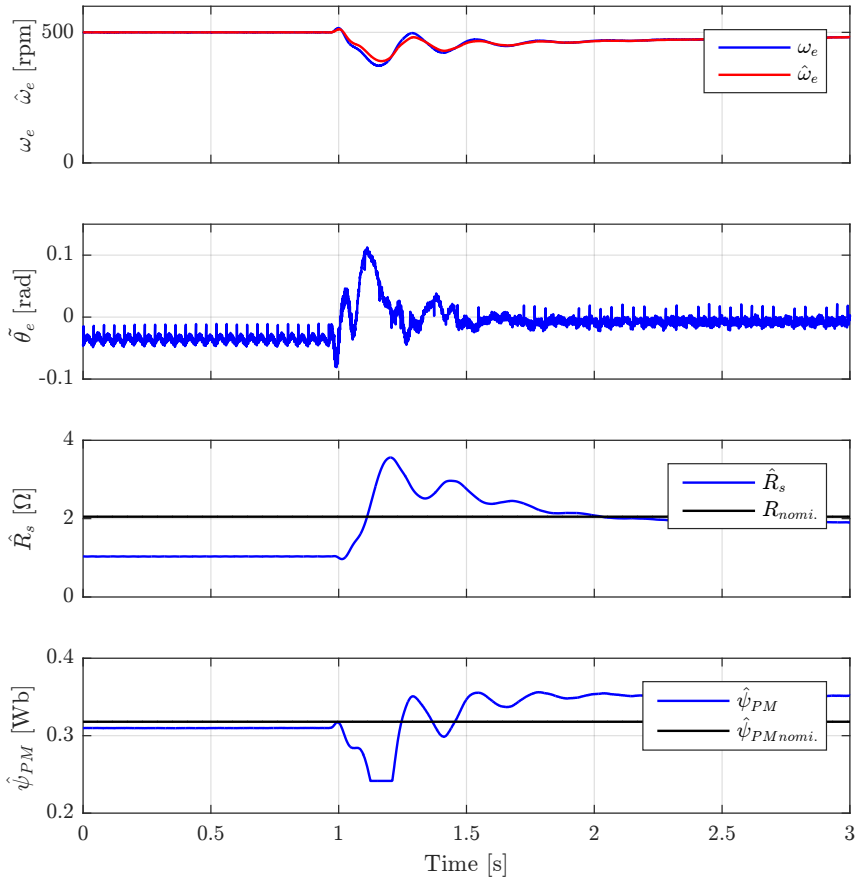

Figure 7.7: Sensorless performance with $\hat{R}_s$ and $\hat{\psi}_{PM}$ estimation based on EKF. Half rated load added at 1s, with compensation, 500rpm constant speed.

approximately 0), the estimation of $\hat{R}_s$ can only be calculated by the sampled u_d and i_d. On the contrary, the back EMF terms in (7.2) become more significant and accurate when the speed goes higher or with a higher load. In this case, the estimation of $\hat{R}_s$ is calculated by the balance of the resistive drop and the back EMF in (7.2) and is more accurate.

The load step test was done as well for both methods at a constant speed of 500 rpm. At 1s, a half rated load was added. The results are shown in Fig. 7.7 and Fig. 7.8. The $\tilde{\theta}_e$, $\hat{R}_s$ and $\hat{\psi}_{\text{PM}}$ had similar behavior for both EKF and MRAS. Exact comparisons are listed in Table 7.1.

Feature	EKF		MRAS	
Estimation Type	R_s and ψ_{PM}(Fig. 8)	L_s and ψ_{PM}(Fig. 10)	R_s and ψ_{PM}(Fig. 9)	L_s and ψ_{PM}(Fig. 11)
Estimation Prerequisite	$i_d \neq 0$	$i_q \neq 0$	$i_d \neq 0$	$i_q \neq 0$
Computation Time	10.8μs	10.75μs	6.44μs	6.435μs
Convergence Rate	1.05s/1.10s	0.88s/1.02s	1.62s/1.63s	1.32s/1.35s
Accuracy at Steady State$*$	6.2%/10.5%	94%/0.4%	3.4%/9.2%	1.7%/0.2%
Accuracy at Dynamic State$**$	73%/23%	94%/6.6%	82%/23.8%	45.8%/10.4%
Rotor Position Error	0.005 rad	0.02 rad	0.006 rad	0.03 rad
$*$:(Steady Value - Rated Value)/Rated Value $**$:(Maximum Value - Rated Value)/Rated Value				

Table 7.1: Comparative issues of sensorless performance between EKF and MRAS.

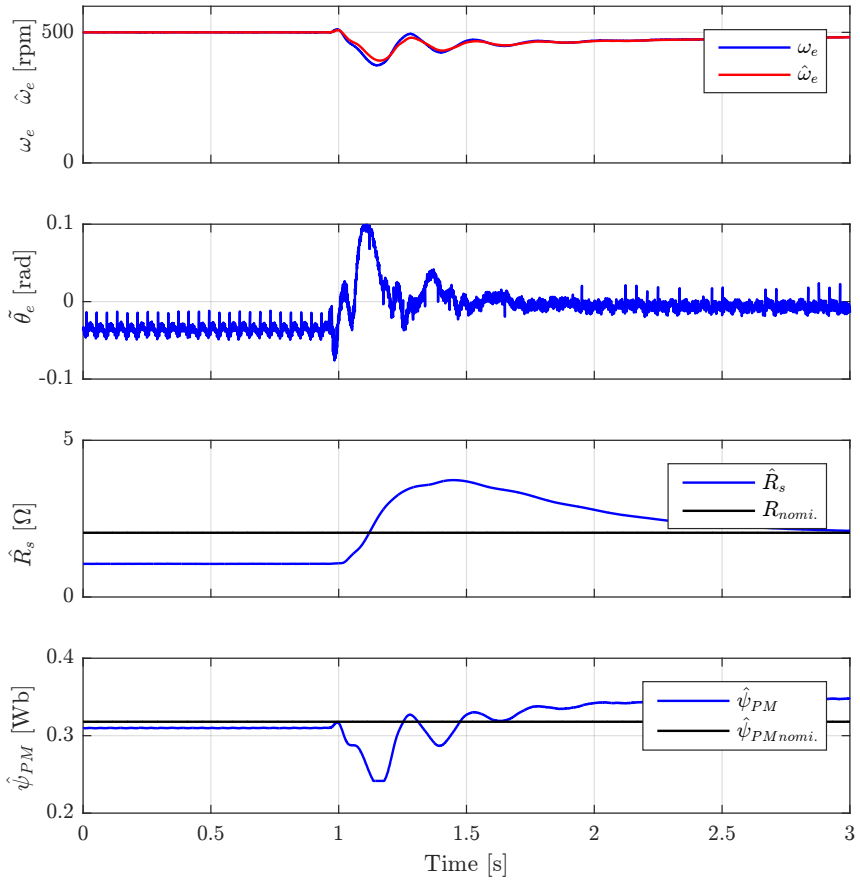

Figure 7.8: Sensorless performance with $\hat{R}_s$ and $\hat{\psi}_{PM}$ estimation based on MRAS. Half rated load added at 1s, with compensation, 500rpm constant speed.

7.5.2 Sensorless control with inductance and PM flux estimation

In previous subsection, the estimation performance of R_s and ψ_{PM} for both EKF and MRAS is illustrated. In this subsection, another estimation type L_s and ψ_{PM} estimation is experimentally compared as well. Note that, the L_s can be estimated only with load condition if $i_d = 0$.

The experimental results of EKF and MRAS under three step load changes are given in Fig. 7.9 and Fig. 7.10, respectively. The load 0.5 Nm, 1.5 Nm, 2.5 Nm were added step by step. The performance of $\tilde{\theta}_e$ and $\hat{\psi}_{PM}$ for both methods are similar. However, there is a slight difference for $\hat{L}_s$ estimation at dynamic state.

7.5.3 Experimental comparison of MRAS and EKF

The corresponding experimental results are shown in the Table 7.1. Several conclusions can be summarized:

- Any two parameters can be estimated only when such specific conditions are satisfied (e.g.,$i_d \neq 0$ or $i_q \neq 0$), which is valid for both estimators.
- The convergence rate of the EKF is faster than that of the MRAS.

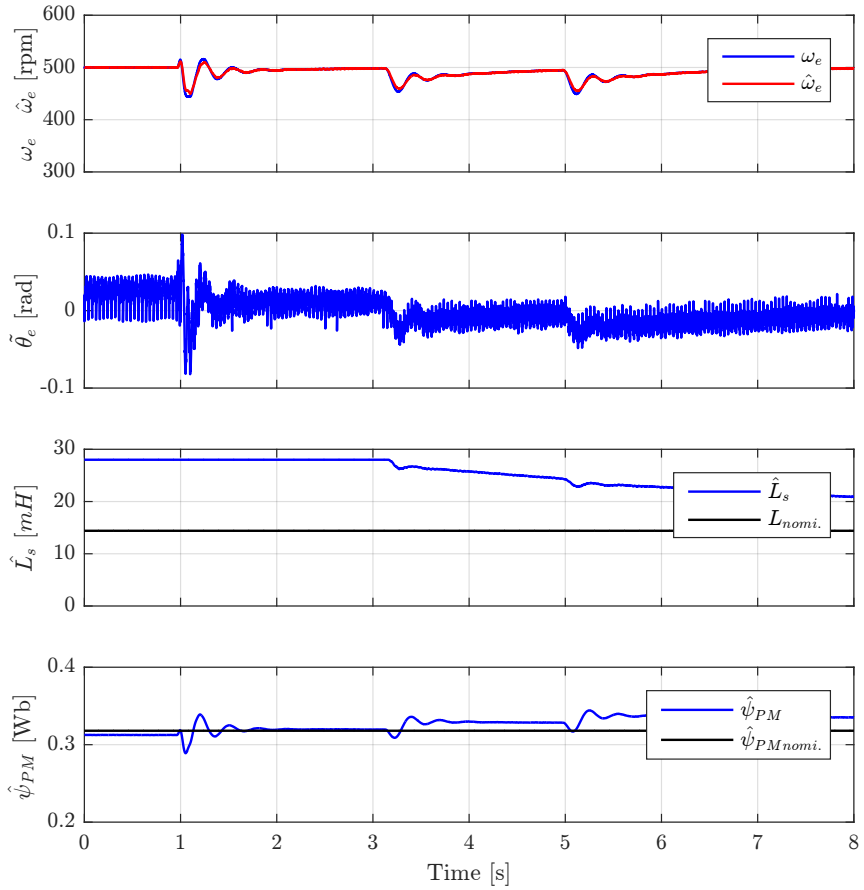

Figure 7.9: Sensorless performance with $\hat{L}_s$ and $\hat{\psi}_{PM}$ estimation based on EKF. 500rpm constant speed, step load:0.5Nm, 1.5Nm and 2.5Nm.

- The dynamic and steady state accuracy of the EKF has less precision than that of the MRAS.
- The rotor position estimation error for both EKF and MRAS are similar.
- The estimation of the rotor flux is less affected by operation conditions than that of the resistance and inductance.
- The estimated resistance and inductance for both estimators are not precisely equal to their nominal values, because they take into account other non-linearities of the control system (e.g., A/D sampling error, DC link voltage variation and the resistive voltage drops in the power devices).

7.6 Summary

This chapter presents a comparative study of two popular multi-parameter estimators, MRAS and EKF, in sensorless controlled PMSM drives where an active flux observer is adopted. The parameter identifiability is discussed and reveals that multi-parameter estimation is restricted

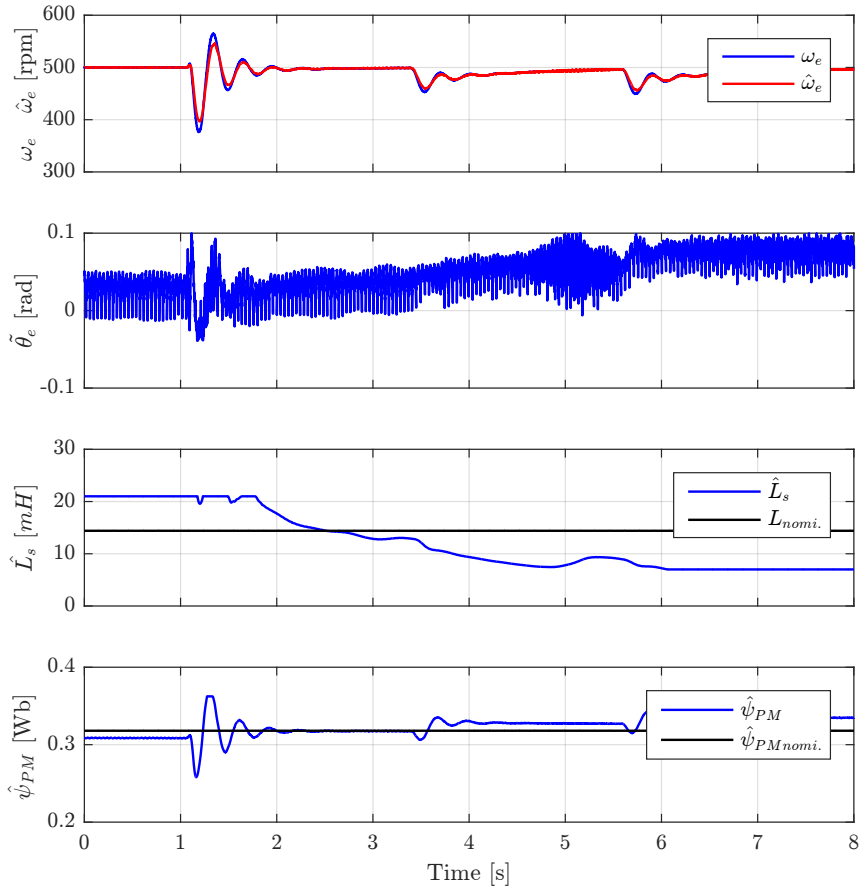

Figure 7.10: Sensorless performance with $\hat{L}_s$ and $\hat{\psi}_{PM}$ estimation based on MRAS. 500rpm constant speed, step load:0.5Nm, 1.5Nm and 2.5Nm.

by the $i_d - i_q$ condition. The potential parameter estimation possibilities for both estimators are comprehensively introduced and then theoretically compared. In order to avoid the effect of inverter non-linearity, a dead-time compensation scheme is adopted and improves the parameter estimation accuracy. In addition, the PMSM sensorless control system with both parameter estimators is comparatively tested on an experimental test bench. The merits and demerits of both estimators are concluded according to different standards and requirements.

CHAPTER 8

Conclusion

This dissertation is carried out mainly to solve the sensorless control problem of the SPMSM with strong multiple saliencies (cwSPMSM). The four questions mentioned in Ch. 1

1) how to decouple or combine stronger multiple saliencies

2) initial position estimation in the presence of multiple saliencies

3) the comparison of fundamental model based sensorless methods in higher speed range applications

4) the on-line parameter identification

are answered.

The emphasis of this dissertation is on the saliency tracking based sensorless method due to the fact that the sensorless control problem in the low speed range arising from multiple saliencies of the cwSPMSM is more challenging. In Ch. 5, firstly, the experimental results are obtained to build the special saliency model of the cwSPMSM. The explanation of causing strong multiple saliencies is also given. Then, three kinds of saliency tracking based sensorless methods are proposed from different perspectives.

The first one is the Multi-Signal Injection method, which makes use of the dependency of the saliency signal on the frequency of injected HF signal. It combines the results of two HF signals and synthesizes a new signal that has the same behavior as the primary saliency signal. And then, the failed traditional demodulation methods become valid again. The MSI method is an effective combination method but it consumes more energy and brings more acoustic noise to the system.

The second one is the Secondary Saliency Tracking method, which belongs to the decoupling group. This method utilizes the rotation difference of the primary saliency signal and secondary saliency signal to separate one from another. In this method, the secondary saliency signal is extracted out from the NSC by means of a specially designed BPF and an ANF. Moreover,

an initial position estimation scheme is proposed accordingly as well to start the cwSPMSM smoothly without heavy load. However, the start at standstill with full load is still challenging for this method and the decoupling performance around zero speed is not satisfactory.

The third one is the Repetitive Control method, whose principle is also decoupling. This method treats the secondary saliency signal as a disturbance and builds an RC model to eliminate it from the NSC. The new concept of an angle domain RC is proposed in the method and shows very good tracking performance. Similar to the previous methods, it has a drawback i.e. the divergence possibility in case of a drastic dynamic change. The proposed three methods have advantages as well as disadvantages as explained. No single method can solve all the problems. In addition, the methods are designed for low speed operation and they all require the injection of HF signals. When the speed of the cwSPMSM goes higher, it is mandatory to change to a fundamental model based method to eliminate the energy consumption and acaustic noise caused by HF signals.

As a necessary supplementary to Ch. 5, three popular fundamental model based methods are comparatively introduced and experimentally compared in Ch. 6 for the higher speed sensorless control of the cwSPMSM. They are the Model Reference Adaptive System, Sliding Mode Observer and Extended Kalman Filter. Any one of them can be combined with one of the methods proposed in Ch. 5 to formulate a hybrid scheme for the whole speed range operation. A simple transition region design is used to smooth the switch between the two methods. Aiming to improve the parameter adaptation of the fundamental model based sensorless method, the multi-parameter identification based on MRAS and EKF is investigated in Ch. 7. Due to the rank-deficiency of the state equations of a PMSM model, a maximum of two parameters are simultaneously identifiable and several prerequisites must be respected in advance. In order to evaluate the performance of both estimators, the estimated parameters resulting from either MRAS or EKF are then applied equally to an Active Flux Observer that has the simplest structure but still works well for sensorless control at higher speeds. At last, the comparison of the estimation performance is summarized and shows that the selection of the appropriate estimator highly depends on the needed parameters and special application.

All the above proposed methods are carried out on an experimental testbench, which is introduced in Ch. 4. Three improvements are made to further enhance the performance of the existing controller. Firstly, an SVPWM algorithm is designed in the FPGA to increase the utilization of the DC link voltage and meanwhile release the calculation burden of the CPU. Secondly, a resolver demodulation circuit and relevant decode-software are developed as well to make the controller adaptive to different interfaces. Thirdly, the C code and the VHDL code generation through Matlab/Simulink are achieved, which enables the designers get rid of the programming burden and accelerate the development progress. They will become more and more popular in various applications in the future.

In this dissertation, a complete solution for the sensorless control of a cwSPMSM is provided and some key questions are discussed. The comparative studies of saliency tracking based method, fundamental model based method and parameter identification are given throughout in the dissertation. It can be found that the same problem can always be solved by different methods created from different perspectives. Therefore, to balance the benefits and drawbacks is the key criteria for selecting the proper method, which is fit for other occasions as well.

APPENDIX A

List of publications

A.1 Journal papers

- **Z. Chen**, F. Wang, G. Luo, Z. Zhang and R. Kennel, “Secondary Saliency Tracking Based Sensorless Control for Concentrated Winding SPMSM", *Industrial Informatics, IEEE Transactions on*, vol.12, no.1, pp.201,210, Feb.2016.
- **Z. Chen**, J. Gao, F. Wang, Z. Ma, Z. Zhang and R. Kennel, “Sensorless Control for SPMSM With Concentrated Windings Using Multisignal Injection Method", *Industrial Electronics, IEEE Transactions on*, vol.61, no.12, pp.6624,6634, Dec. 2014.
- F. Wang, **Z. Chen**, P. Stolze, J. -F. Stumper, J. Rodriguez and R. Kennel, “Encoderless Finite-State Predictive Torque Control for Induction Machine with a Compensated MRAS", *Industrial Informatics, IEEE Transactions on*, vol.10, no.2, pp.1097,1106, May 2014.
- F. Wang, **Z. Chen**, M. Trincado, P. Stolze, J. Rodriguez and R. Kennel, “ High Performance Control Strategies of Electrical Drives: an Evaluation of DTC and FCS-PTC", *EPE Journal*, accepted, 2015.
- Z. Zhang, H. Xu, M. Xue, **Z. Chen**; T. Sun; R. Kennel and C.M.Hackl, “Predictive Control With Novel Virtual-Flux Estimation for Back-to-Back Power Converters", *Industrial Electronics, IEEE Transactions on*, vol.62, no.5, pp.2823,2834, May 2015.

A.2 Conference papers

- **Z. Chen**, Z. Zhang, G. Luo and R. Kennel, “Hybrid Sensorless Control for SPMSM With Multiple Saliencies", *41st Annual Conference of the IEEE Industrial Electronics Society*, 2015.

- **Z. Chen**, C. Wu, R. Qi, G. Luo and R. Kennel, “Decoupling of Secondary Saliencies in Sensorless AC Drives Using Repetitive Control", *Power Eletronics and Applications (EPE), 17th*, 2015.

- **Z. Chen**, F. Wang, P. Stolze and R. Kennel, “Using Compensated MRAS for Model Predictive Control of Induction Machine", *Power Eletronics and Applications (EPE), 15th*, 2013.

- Z. Zhang, **Z. Chen**, C. Wu and R. Kennel, “Fully FPGA Based Performance-Enhanced DMPC for Grid-Tied AFEs with Multiple Predictions", *41st Annual Conference of the IEEE Industrial Electronics Society*, 2015.

- Z. Zhang, C. Hackl, F. Wang, **Z. Chen** and R. Kennel, “Encoderless Model Predictive Control of Back-to-Back Converter Direct-Drive Permanent magnet Synchronous Generator Wind Turbine Systems", *Power Eletronics and Applications (EPE), 15th*, 2013.

APPENDIX B

Abbreviations

AC	Alternating Current
A/D	Analog to Digital (converter)
AFO	Active Flux Observer
IM	Induction Machine
ANF	Adaptive Notch Filter
BLDCM	Brushless Direct Current Machine
BPF	Band Pass Filter
CPLD	Complex Programmable Logic Device
CPU	Central Processing Unit
cwSPMSM	Concentrated winding SPMSM
D/A	Digital to Analog (converter)
DB	Dead-beat
DC	Direct Current
DSC	Direct Switch Control
DSP	Digital Signal Processor
DTC	Direct Torque Control
EKF	Extended Kalman Filter
EMI	Electromagnetic Interference
EMF	back Electromagnetic Force
FEA	Finite Element Analysis

FFT	Fast Fourier Transformation
FOC	Field Oriented Control
FPWMI	Fundamental PWM-Integrated
FPGA	Field Programmable Gate Array
HDL	Hardware Description Language
HF(SI)	High Frequency (Signal Injection)
HIL	Hardware In the Loop
IGBT	Insulated Gate Bipolar Transistor
INFORM	Indirect Flux detection by On-line Reactance Measurement
IPMSM	Interior PMSM
ISA	Industry Standard Architecture (bus)
LCD	Liquid Crystal Display
(E)LO	(Extended) Luenberger Observer
LPF	Low Pass Filter
LUT	Look-up Table
LVDS	Low Voltage Differential Signaling
MRAS	Model Reference Adaptive System
MSI	Multi-Signal Injection
MTPA	Maximum Torque Per Ampere
NSC	Negative-Sequence Current
PCB	Printed Circuit Board
PI	Proportional Integral
PLL	Phase Locked Loop
PTC	Predictive Torque Control
PMSM	Permanent Magnet Sychronous Machine
PWM	Pulse Width Modulation
RC	Repetitive Control
RLS	Recursive Least Square
RMS	Root Mean Square
RPM	Revolutions Per Minute
RTAI	Real-Time Application Interface
SOS	Second Order Sections filter
SPMSM	Surface-mounted PMSM
SRF	Stationary Reference Frame
SST	Secondary Saliency Tracking
SM	Synchronous Machine
SMO	Sliding Mode Observer
SNR	Signal to Noise Ratio
SRM	Switched Reluctance Machine
SPWM	Sinusoidal Pulse Width Modulation
SVPWM	Space Vector Pulse Width Modulation
SyRM	Synchronous Reluctance Machine
VHDL	Very High Speed Integrated Circuit Hardware Description Language
VSI	Voltage Source Inverter
ZSV	Zero-Sequence Voltage
ZSC	Zero-Sequence Current

APPENDIX C

Testbench data

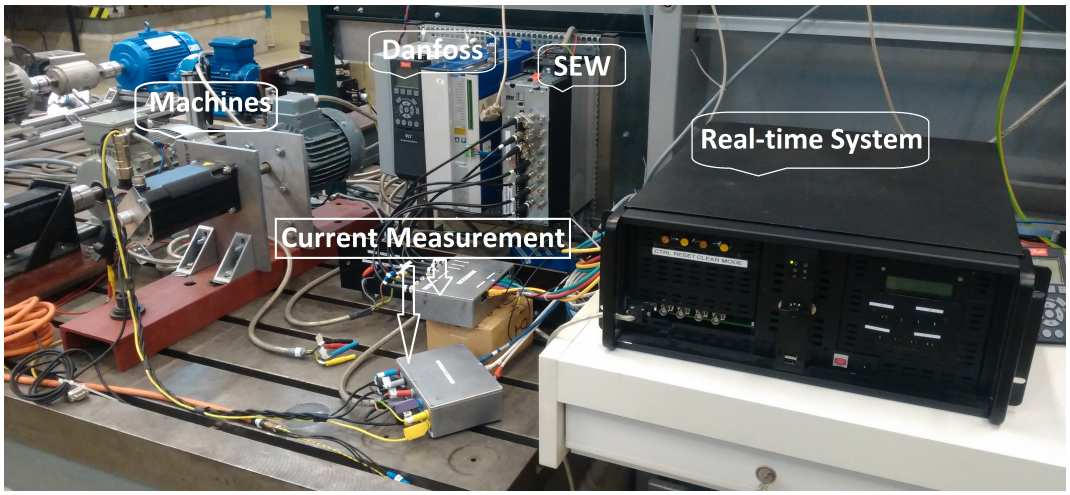

Figure C.1: The whole testbench

A overview of the whole test bench has already been given in Ch. 4. The complete test bench is composed of a real-time computer system, four machines, two two-level inverters and measurement devices. A picture of the test bench can be seen in Fig. C.1. The corresponding machines' parameters are listed in Table C.1 to C.4.

The control-side 5kW inverter is manufactured and modified by the company SEW® and it provides full control of the upper side 3 IGBT gates and the other 3 PWM signals for the lower side 3 IGBTs are generated by the SEW® inverter itself. The dead-time is 0.8 μs. Consequently, only 3 channel PWM signals are produced by the real time system are fed to the control-side SEW® inverter to implement any control algorithm. The load-side 5kW inverter is made by the company Danfoss® and it is equipped with a micro-controller and can be configured manually through a front-panel and an LCD display. It drives a load-side induction machine. The power

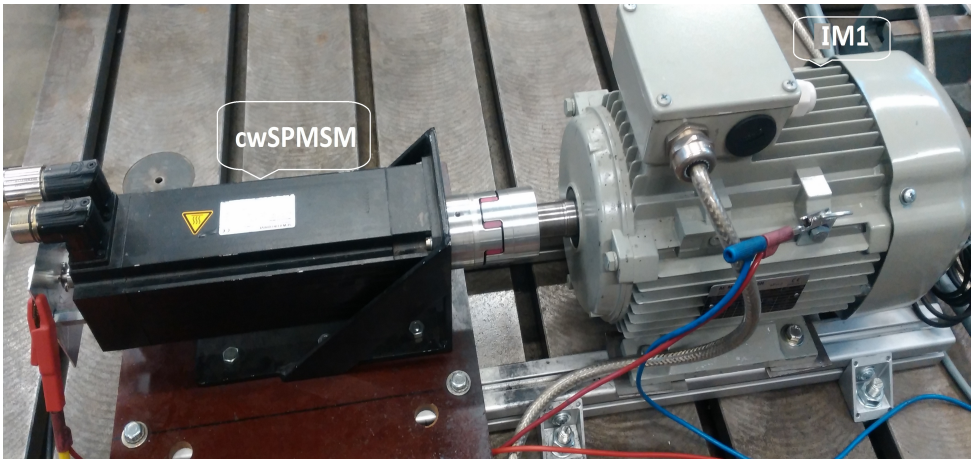

Figure C.2: cwSPMSM

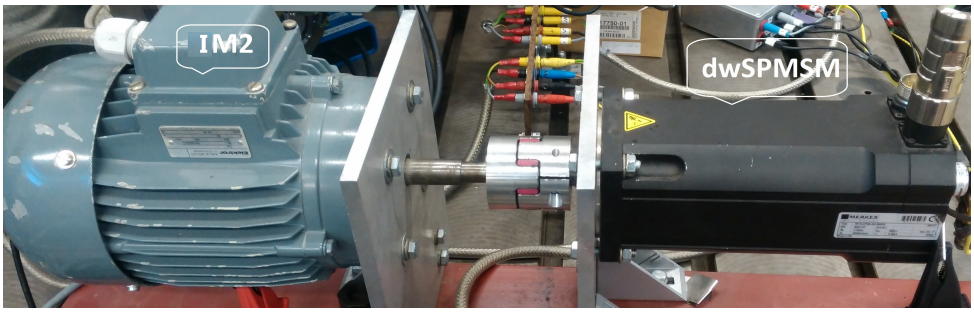

Figure C.3: dwSPMSM

connectors and encoder/resolver connectors of both inverters are standardized, and therefore, it is easy to switch to any machine within the power range.

Table C.1: Parameters for the IM1

Parameter	Value
Nominal power P_{nom}	2.2 kW
Synchronous frequency f_{syn}	50 Hz
Nominal current $\lvert \boldsymbol{i}_{\text{s, nom}} \rvert$	6.44 A
Power factor $\cos(\varphi)$	0.82
Nominal speed ω_{nom}	1420 rpm
Number of pole pairs p	1
Stator resistance R_{s}	2.6827 Ω
Rotor resistance R_{r}	2.1290 Ω
Stator inductance L_{s}	283.4 mH
Rotor inductance L_{r}	283.4 mH
Mutual inductance L_{m}	275.1 mH

Table C.2: Parameters for the IM2

Parameter	Value
Nominal power P_{nom}	$1.8\,\text{kW}$
Synchronous frequency f_{syn}	$50\,\text{Hz}$
Nominal current $\lvert\boldsymbol{i}_{\text{s, nom}}\rvert$	$4.3\,\text{A}$
Power factor $\cos(\varphi)$	0.86
Nominal speed ω_{nom}	$2830\,\text{rpm}$
Number of pole pairs p	1
Stator resistance R_{s}	$3.8094\,\Omega$
Rotor resistance R_{r}	$3.2402\,\Omega$
Stator inductance L_{s}	$285.4\,\text{mH}$
Rotor inductance L_{r}	$285.4\,\text{mH}$
Mutual inductance L_{m}	$278.2\,\text{mH}$

Table C.3: Parameters for the cwSPMSM

Parameter	Value
Nominal power P_{nom}	$2.2\,\text{kW}$
Synchronous frequency f_{syn}	$150\,\text{Hz}$
Nominal current $\lvert\boldsymbol{i}_{\text{s, nom}}\rvert$	$4.95\,\text{A}$
Nominal speed ω_{nom}	$3000\,\text{rpm}$
Number of pole pairs p	3
Stator resistance R_{s}	$2.07\,\Omega$
Stator inductance L_{s}	$14.2\,\text{mH}$

Table C.4: Parameters for the dwSPMSM

Parameter	Value
Nominal power P_{nom}	$2.0\,\text{kW}$
Synchronous frequency f_{syn}	$150\,\text{Hz}$
Nominal current $\lvert\boldsymbol{i}_{\text{s, nom}}\rvert$	$4.76\,\text{A}$
Nominal speed ω_{nom}	$3000\,\text{rpm}$
Number of pole pairs p	3
Stator resistance R_{s}	$0.9\,\Omega$
Stator inductance L_{s}	$9.3\,\text{mH}$

APPENDIX D

Derivation of the MSI method and filter design

D.1 Mathematical derivation

In order to get a combination result of all HF responses, it is necessary to use matrix analysis. According to (5.9), the following matrix equation (a) can be introduced by considering all M responses. Each row of this matrix represents a response resulted for one frequency injection condition.

$$\underbrace{\begin{bmatrix} i^{cn}_{dqcn1}e^{-\delta_1} \\ i^{cn}_{dqcn2}e^{-\delta_2} \\ \vdots \\ i^{cn}_{dqcnM}e^{-\delta_M} \end{bmatrix}}_{A} = \underbrace{\begin{bmatrix} I_{11} & I_{12} & \dots & I_{1N} \\ I_{21} & I_{22} & \dots & I_{2N} \\ \vdots & \vdots & \ddots & \vdots \\ I_{M1} & I_{M2} & \dots & I_{MN} \end{bmatrix}}_{B} \underbrace{\begin{bmatrix} e^{j(h_1\theta_e+\varphi_1-\pi/2)} \\ e^{j(h_2\theta_e+\varphi_2-\pi/2)} \\ \vdots \\ e^{j(h_N\theta_e+\varphi_N-\pi/2)} \end{bmatrix}}_{X} \tag{a}$$

where I_{mi} in B represents I_{cnmi} for simplification. A represents a set of combinations of rotor-position-dependent multiple-saliency signals. B denotes a set of all magnitudes of multiple saliencies acquired through an FFT analysis.

$A = BX$ is a linear system. A linear transformation can be applied to matrices A and B. Finally, matrix B can be transformed to an upper triangular matrix $\tilde{B}$ according to the matrix theory. $\tilde{I}_{mi}$ are the new magnitudes of multiple saliencies after the transformation.

$$\underbrace{\begin{bmatrix} i^{cn}_{dqcn1}e^{-\delta_1} \\ i_2 \\ \vdots \\ i_M \end{bmatrix}}_{\tilde{A}} = \underbrace{\begin{bmatrix} I_{11} & I_{12} & \dots & I_{1N} \\ 0 & \tilde{I}_{22} & \dots & \tilde{I}_{2N} \\ \vdots & 0 & \ddots & \vdots \\ 0 & \dots & 0 & \tilde{I}_{MN} \end{bmatrix}}_{\tilde{B}} \begin{bmatrix} e^{j(h_1\theta_e+\varphi_1-\pi/2)} \\ e^{j(h_2\theta_e+\varphi_2-\pi/2)} \\ \vdots \\ e^{j(h_N\theta_e+\varphi_N-\pi/2)} \end{bmatrix} \tag{b}$$

$$\tilde{I}_{mi} = \sum_{m=1}^{M} \alpha_m I_{mi} \quad \alpha_m \in \mathbb{R} \tag{c}$$

$$i_m = \sum_{m=1}^{M} \alpha_m i_{dqcnm}^{cn} e^{-\delta_m} \quad \alpha_m \in \mathbb{R} \tag{d}$$

If the last equation of this matrix is chosen for an estimation purpose, it is (5.10)

$$i_M = \sum_{m=1}^{M} \alpha_m i_{dqcnm}^{cn} e^{-\delta_m} = \tilde{I}_{MN} e^{j(h_N \theta_e + \varphi_N - \pi/2)} \tag{5.10}$$

D.2 Filter Design

The issues regarding the parameters of the designed filters are introduced in Table. II. The types of filters, the orders of the filter and their cut-off frequencies are presented, respectively. For higher speeds, the switchover to a model-based sensorless method is mandatory. Then the filters introduced by the HF method will be eliminated or changed according to a model-based method.

Parameters	Fundamental Signals	HF Signals (1kHz/455Hz)		Estimated and Measured Speeds
Filter Type	LPF(Elliptic)	BPF(Elliptic)	LPF(Elliptic)	LPF(Digital RC)
Filter Order	2	4/6	6/6	1
Cut-Off Frequency(Hz)	300	[950 1050]/[405 505]	355/355	100

Table D.1: Filter Parameters of Control System

List of Figures

2.1 Rotating HF signal injection method in $\alpha - \beta$ frame. 9
2.2 Pulsating HF signal injection method in $\hat{d} - \hat{q}$ frame. 10
2.3 Pulsating HF signal injection method in $\alpha - \beta$ frame. 11
2.4 Inverter and voltage vectors. 11
2.5 Active flux observer with PLL. 14
2.6 Model reference adaptive system. 15
2.7 Luenberger observer. 16
2.8 Extended Kalman filter. 17
2.9 Sliding mode observer. 17

3.1 Orientation of reference frames. 26
3.2 Space vector definition. 27
3.3 Vector transformation from $\alpha - \beta$ to $d - q$ frame. 28
3.4 Demodulation and PLL. 33

4.1 Hardware setup. 40
4.2 SVPWM implementation. 42
4.3 PWM module and SVPWM sub-module in FPGA. 42
4.4 Resolver decode schematic diagram. 44
4.5 Resolver decode circuit PCB. 44
4.6 C code generation procedures. 45
4.7 Generation report. 45
4.8 Generated file list. 46
4.9 VHDL code generation procedures. 47
4.10 Optimization through *Fixed Point Tool*. 48
4.11 VHDL generation report. 48
4.12 Matlab-ModelSim co-simulation. 49
4.13 FPGA in the loop co-simulation. 49

5.1 Sensorless control system using the HF signal injection method. 52
5.2 Waveforms of NSC and their FFT Analysis (1kHz 35V), left: (normal BPF), right: (proposed BPF). 52
5.3 Stator background comparison. 55

5.4 Flux distribution. 56
5.5 Multi-signal injection method. 60
5.6 NSC trajectory and FFT Analysis, left: (455Hz 15V), right: (1kHz 20V). . . . 61
5.7 Flux angle estimation results of the multi-signal injection method. 64
5.8 Block diagram of the decoupling method. 64
5.9 Position estimation performance at 100 rpm speed using the traditional decoupling method. 65
5.10 Sensorless performance at 100 rpm speed without load using the multi-signal injection method. 65
5.11 Sensorless performance at 100 rpm speed with a rated load torque using the multi-signal injection method without compensation. 66
5.12 Load dependent angle compensation. 66
5.13 Sensorless performance at 100 rpm speed with a rated load torque using the multi-signal injection method with a compensation. 67
5.14 Sensorless performance of ± 100 rpm speed reverse using the multi-signal injection method. 68
5.15 General decoupling of one saliency signal within PLL. 70
5.16 Decoupling of the primary saliency signal with ANF. 70
5.17 Specially designed BPF (Sampling frequency is 16kHz). 72
5.18 Initial position estimation flow chart. 73
5.19 Primary saliency tracking results (rotating HF signal injection 1kHz,35V). . . . 73
5.20 Load dependent angle compensation. 74
5.21 Initial position estimation (a) $-\pi/2$ difference (b) π difference. 75
5.22 Sensorless closed-loop performance of without(0-3.5s) and with (3.5s-) ANF at 20 rpm with 50% rated load. 76
5.23 Sensorless closed-loop performance from 0 to 200 rpm without load. 76
5.24 Sensorless closed-loop performance at 100 rpm speed with a rated load using the SST method. 77
5.25 Sensorless closed-loop performance from -100 to 100 rpm with a rated load. . . 78
5.26 The structure of a Plug-in repetitive control. 79
5.27 The proposed Plug-in repetitive control in an angle domain. 79
5.28 Realization of RC in the angle domain. 80
5.29 Flow chart of calculation of the proposed RC. 81
5.30 Comparison of PLL without and with RC at 40 rpm. 81
5.31 Comparison of PLL without and with proposed RC at 100 rpm. 82
5.32 Comparison of dynamic performance under step half rated torque at 100 rpm. . 82
5.33 Comparison of dynamic performance under step speed change with half rated torque. 83

6.1 Speed step performance comparison (200 rpm-500 rpm-200 rpm). 91
6.2 Torque step performance comparison (0 N.m-7 N.m-0 N.m). 92
6.3 Hybrid sensorless control performance SST+MRAS, transition region 200 rpm-250 rpm. 94

7.1 Observer structures of MRAS and EKF. 96

7.2 Overview of a sensorless PMSM control system. 97
7.3 Sensorless performance with $\hat{R}_s$ and $\hat{\psi}_{PM}$ estimation based on EKF. No load, 100 rpm, without (0-1s) and with (1s-) compensation of inverter non-linearity. . 102
7.4 Sensorless performance with $\hat{R}_s$ and $\hat{\psi}_{PM}$ estimation based on MRAS. No load, 100 rpm, without (0-1s) and with (1s-) compensation of inverter non-linearity. . 103
7.5 Sensorless performance with $\hat{R}_s$ and $\hat{\psi}_{PM}$ estimation based on EKF. No load, with compensation, speed changes from 150rpm to 500rpm. 104
7.6 Sensorless performance with $\hat{R}_s$ and $\hat{\psi}_{PM}$ estimation based on MRAS. No load, with compensation, speed changes from 150rpm to 500rpm. 105
7.7 Sensorless performance with $\hat{R}_s$ and $\hat{\psi}_{PM}$ estimation based on EKF. Half rated load added at 1s, with compensation, 500rpm constant speed. 106
7.8 Sensorless performance with $\hat{R}_s$ and $\hat{\psi}_{PM}$ estimation based on MRAS. Half rated load added at 1s, with compensation, 500rpm constant speed. 107
7.9 Sensorless performance with $\hat{L}_s$ and $\hat{\psi}_{PM}$ estimation based on EKF. 500rpm constant speed, step load:0.5Nm, 1.5Nm and 2.5Nm. 108
7.10 Sensorless performance with $\hat{L}_s$ and $\hat{\psi}_{PM}$ estimation based on MRAS. 500rpm constant speed, step load:0.5Nm, 1.5Nm and 2.5Nm. 109

C.1 The whole testbench 117
C.2 cwSPMSM 118
C.3 dwSPMSM 118

List of Tables

3.1 List of symbol representations 24
3.2 List of subscripts 24
3.3 List of superscripts 25
3.4 List of top-scripts 25

4.1 Functions of the modules inside the FPGA. 41

6.1 Theoretical comparison of MRAS, SMO and EKF. 90
6.2 Minimal Speed. 93
6.3 Observers' parameter dependence range. 93
6.4 Overview of experimental comparison. 93

7.1 Comparative issues of sensorless performance between EKF and MRAS. . . . 106

C.1 Parameters for the IM1 118
C.2 Parameters for the IM2 119
C.3 Parameters for the cwSPMSM 119
C.4 Parameters for the dwSPMSM 119

D.1 Filter Parameters of Control System 122

Bibliography

[1] M. W. Degner and R. D. Lorenz, "Using multiple saliencies for the estimation of flux, position, and velocity in ac machines," *IEEE Trans. Ind. Appl.*, vol. 34, no. 5, pp. 1097–1104, 1998.

[2] F. Briz, M. W. Degner, A. Diez, and R. D. Lorenz, "Static and dynamic behavior of saturation-induced saliencies and their effect on carrier-signal-based sensorless ac drives," *IEEE Trans. Ind. Appl.*, vol. 38, no. 3, pp. 670–678, 2002.

[3] D. D. Reigosa, P. Garcia, D. Raca, F. Briz, and R. D. Lorenz, "Measurement and adaptive decoupling of cross-saturation effects and secondary saliencies in sensorless controlled ipm synchronous machines," *IEEE Trans. Ind. Appl.*, vol. 44, no. 6, pp. 1758–1767, 2008.

[4] D. Raca, P. Garcia, D. D. Reigosa, F. Briz, and R. D. Lorenz, "Carrier-signal selection for sensorless control of pm synchronous machines at zero and very low speeds," *IEEE Trans. Ind. Appl.*, vol. 46, no. 1, pp. 167–178, 2010.

[5] Y. Shih-Chin, T. Suzuki, R. D. Lorenz, and T. M. Jahns, "Surface-permanent-magnet synchronous machine design for saliency-tracking self-sensing position estimation at zero and low speeds," *IEEE Trans. Ind. Appl.*, vol. 47, no. 5, pp. 2103–2116, 2011.

[6] Y. Shih-Chin and R. D. Lorenz, "Comparison of resistance-based and inductance-based self-sensing controls for surface permanent-magnet machines using high-frequency signal injection," *IEEE Trans. Ind. Appl.*, vol. 48, no. 3, pp. 977–986, 2012.

[7] R. Raute, C. Caruana, C. S. Staines, J. Cilia, N. Teske, M. Sumner, and G. M. Asher, "A review of sensorless control in induction machines using hf injection, test vectors and pwm harmonics," in *Proc. IEEE SLED Sympos.*, 2011, pp. 47–55.

[8] J. Holtz and J. Quan, "Sensorless vector control of induction motors at very low speed using a nonlinear inverter model and parameter identification," *IEEE Trans. Ind. Appl.*, vol. 38, no. 4, pp. 1087–1095, Jul 2002.

[9] N. Teske, G. M. Asher, M. Sumner, and K. J. Bradley, "Suppression of saturation saliency effects for the sensorless position control of induction motor drives under loaded conditions," *IEEE Trans. Ind. Electron.*, vol. 47, no. 5, pp. 1142–1150, 2000.

[10] P. L. Dirk Paulus and R. Kennel, "Arbitrary injection for permanent magnet synchronous machine with multiple saliencies," in *Proc. IEEE ECCE Conf.*, 2013, pp. 511–517.

[11] A. Eilenberger, M. Schroedl, and J. Heissenberger, "Comparison of outer rotor pmsm with single- and double-layer windings at same machine geometry with respect to the sensorless control capability," in *Power Electronics and Applications, 2009. EPE '09. 13th European Conference on*, Sept 2009, pp. 1–7.

[12] P. Sergeant, F. De Belie, and J. Melkebeek, "Rotor geometry design of interior pmsms with and without flux barriers for more accurate sensorless control," *IEEE Trans. Ind. Electron.*, vol. 59, no. 6, pp. 2457–2465, June 2012.

[13] N. Imai, S. Morimoto, M. Sanada, and Y. Takeda, "Influence of magnetic saturation on sensorless control for interior permanent-magnet synchronous motors with concentrated windings," *IEEE Trans. Ind. Appl.*, vol. 42, no. 5, pp. 1193–1200, 2006.

[14] P. Sergeant, F. De Belie, and J. Melkebeek, "Rotor geometry design of interior pmsms with and without flux barriers for more accurate sensorless control," *IEEE Trans. Ind. Electron.*, vol. 59, no. 6, pp. 2457–2465, June 2012.

[15] L. Alberti, N. Bianchi, and S. Bolognani, "High frequency d-q model of synchronous machines for sensorless control," in *Energy Conversion Congress and Exposition (ECCE), 2014 IEEE*, Sept 2014, pp. 4147–4153.

[16] P. Jansen and R. Lorenz, "Transducerless position and velocity estimation in induction and salient ac machines," *IEEE Trans. Ind. Appl.*, vol. 31, no. 2, pp. 240–247, 1995.

[17] F. Briz, M. Degner, P. Garcia, and J. Guerrero, "Rotor position estimation of ac machines using the zero-sequence carrier-signal voltage," *IEEE Trans. Ind. Appl.*, vol. 41, no. 6, pp. 1637–1646, Nov 2005.

[18] F. Briz, M. Degner, P. Fernandez, and A. Diez, "Rotor and flux position estimation in delta-connected ac machines using the zero-sequence carrier-signal current," *IEEE Trans. Ind. Appl.*, vol. 42, no. 2, pp. 495–503, March 2006.

[19] C. Staines, C. Caruana, G. Asher, and M. Sumner, "Sensorless control of induction machines at zero and low frequency using zero sequence currents," *IEEE Trans. Ind. Electron.*, vol. 53, no. 1, pp. 195–206, Feb 2005.

[20] F. Briz, M. Degner, P. Garcia, and R. Lorenz, "Comparison of saliency-based sensorless control techniques for ac machines," *IEEE Trans. Ind. Appl.*, vol. 40, no. 4, pp. 1107–1115, July 2004.

[21] M. Corley and R. Lorenz, "Rotor position and velocity estimation for a salient-pole permanent magnet synchronous machine at standstill and high speeds," *IEEE Trans. Ind. Appl.*, vol. 34, no. 4, pp. 784–789, Jul 1998.

[22] J. I. Ha and S. K. Sul, "Sensorless field-orientation control of an induction machine by high-frequency signal injection," *IEEE Transactions on Industry Applications*, vol. 35, no. 1, pp. 45–51, 1999.

[23] J. Ji-Hoon, S. Seung-Ki, H. Jung-Ik, K. Ide, and M. Sawamura, "Sensorless drive of surface-mounted permanent-magnet motor by high-frequency signal injection based on magnetic saliency," *IEEE Trans. Ind. Appl.*, vol. 39, no. 4, pp. 1031–1039, 2003.

[24] M. Linke, R. Kennel, and J. Holtz, "Sensorless speed and position control of synchronous machines using alternating carrier injection," in *Proc. IEEE IEMDC Conf.*, vol. 2, 2003, pp. 1211–1217.

[25] Y.-D. Yoon, S.-K. Sul, S. Morimoto, and K. Ide, "High-bandwidth sensorless algorithm for ac machines based on square-wave-type voltage injection," *IEEE Trans. Ind. Appl.*, vol. 47, no. 3, pp. 1361–1370, May 2011.

[26] J. Liu and Z. Zhu, "Novel sensorless control strategy with injection of high-frequency pulsating carrier signal into stationary reference frame," *IEEE Trans. Ind. Appl.*, vol. 50, no. 4, pp. 2574–2583, July 2014.

[27] A. Yamazaki and K. Ide, "Application trend of saliency-based sensorless drives," in *Power Electronics Conference (IPEC-Hiroshima 2014 - ECCE-ASIA), 2014 International*, May 2014, pp. 933–936.

[28] J. Holtz, "Acquisition of position error and magnet polarity for sensorless control of pm synchronous machines," *IEEE Trans. Ind. Appl.*, vol. 44, no. 4, pp. 1172–1180, 2008.

[29] Y.-D. Yoon and S.-K. Sul, "Sensorless control for induction machines using square-wave voltage injection," in *Energy Conversion Congress and Exposition (ECCE), 2010 IEEE*, Sept 2010, pp. 3147–3152.

[30] J. Liu and Z. Zhu, "Sensorless control strategy by square-waveform high-frequency pulsating signal injection into stationary reference frame," *Emerging and Selected Topics in Power Electronics, IEEE Journal of*, vol. 2, no. 2, pp. 171–180, June 2014.

[31] M. Schroedl, "Sensorless control of ac machines at low speed and standstill based on the ldquo;inform rdquo; method," in *Industry Applications Conference, 1996. Thirty-First IAS Annual Meeting, IAS '96., Conference Record of the 1996 IEEE*, vol. 1, Oct 1996, pp. 270–277 vol.1.

[32] E. Robeischl and M. Schroedl, "Optimized inform measurement sequence for sensorless pm synchronous motor drives with respect to minimum current distortion," *IEEE Trans. Ind. Appl.*, vol. 40, no. 2, pp. 591–598, March 2004.

[33] J. Holtz, "Sensorless control of induction machines with or without signal injection?" *IEEE Trans. Ind. Electron.*, vol. 53, no. 1, pp. 7–30, Feb 2005.

[34] Y. Hua, M. Sumner, G. Asher, Q. Gao, and K. Saleh, "Improved sensorless control of a permanent magnet machine using fundamental pulse width modulation excitation," *Electric Power Applications, IET*, vol. 5, no. 4, pp. 359–370, April 2011.

[35] D. Paulus, P. Landsmann, and R. Kennel, "Sensorless field- oriented control for permanent magnet synchronous machines with an arbitrary injection scheme and direct angle calculation," in *Proc. IEEE SLED Sympos.*, 2011, pp. 41–46.

[36] ——, "General arbitrary injection approach for synchronous machines," in *Sensorless Control for Electrical Drives and Predictive Control of Electrical Drives and Power Electronics (SLED/PRECEDE), 2013 IEEE International Symposium on*, Oct 2013, pp. 1–6.

[37] Z. Ma, J. Gao, and R. Kennel, "Fpga implementation of a hybrid sensorless control of smpmsm in the whole speed range," *IEEE Trans. Ind. Inf.*, vol. 9, no. 3, pp. 1253–1261, Aug 2013.

[38] O. Benjak and D. Gerling, "Review of position estimation methods for ipmsm drives without a position sensor part ii: Adaptive methods," in *Electrical Machines (ICEM), 2010 XIX International Conference on*, Sept 2010, pp. 1–6.

[39] I. Boldea, M. Paicu, and G. Andreescu, "Active flux concept for motion-sensorless unified ac drives," *IEEE Trans. Power Electron.*, vol. 23, no. 5, pp. 2612–2618, Sept 2008.

[40] L. Yongdong and Z. Hao, "Sensorless control of permanent magnet synchronous motor a survey," in *Vehicle Power and Propulsion Conference, 2008. VPPC '08. IEEE*, Sept 2008, pp. 1–8.

[41] F. Genduso, R. Miceli, C. Rando, and G. Galluzzo, "Back emf sensorless-control algorithm for high-dynamic performance pmsm," *IEEE Trans. Ind. Electron.*, vol. 57, no. 6, pp. 2092–2100, June 2010.

[42] Y. Shi, K. Sun, L. Huang, and Y. Li, "Online identification of permanent magnet flux based on extended kalman filter for ipmsm drive with position sensorless control," *Industrial Electronics, IEEE Transactions on*, vol. 59, no. 11, pp. 4169–4178, Nov 2012.

[43] A. Piippo, M. Hinkkanen, and J. Luomi, "Analysis of an adaptive observer for sensorless control of interior permanent magnet synchronous motors," *Industrial Electronics, IEEE Transactions on*, vol. 55, no. 2, pp. 570–576, Feb 2008.

[44] K. Wiedmann and A. Mertens, "Self-sensing control of pm synchronous machines including online system identification based on a novel mras approach," in *Sensorless Control for Electrical Drives (SLED), 2012 IEEE Symposium on*, Sept 2012, pp. 1–8.

[45] J. Kumar, P. Kumar, and M. Rambabu, "Model reference adaptive controller-based speed and q-axis inductance estimation for permanent magnet synchronous motor drive by utilizing reactive power," in *Energy, Automation, and Signal (ICEAS), 2011 International Conference on*, Dec 2011, pp. 1–6.

[46] D. Paulus, P. Landsmann, and R. Kennel, "Saliency based sensorless field- oriented control for permanent magnet synchronous machines in the whole speed range," in *Proc. IEEE SLED Sympos.*, 2012, pp. 1–6.

[47] W. Xu and R. D. Lorenz, "High frequency injection-based stator flux linkage and torque estimation for DB-DTFC implementation on IPMSMs considering cross-saturation effects," *2013 IEEE Energy Convers. Congr. Expo. ECCE 2013*, vol. 50, no. 6, pp. 844–851, 2013.

[48] S. Kuehl and R. M. Kennel, "Measuring Magnetic Characteristics of Synchronous Machines by Applying Position Estimation Techniques," *IEEE Trans. Ind. Appl.*, vol. 50, no. 6, pp. 3816–3824, 2014.

[49] R. K. M. and H. Silva, "Identification of Machine Parameters of a Synchronous Motor," *IEEE Trans. Ind. Appl.*, vol. 41, no. 2, pp. 557–565, 2005.

[50] K. Liu and Z. Q. Zhu, "Position Offset-Based Parameter Estimation for Permanent Magnet Synchronous Machines Under Variable Speed Control," *IEEE Trans. Ind. Electron.*, vol. 30, no. 6, pp. 3438–3446, 2015.

[51] S. Underwood and I. Husain, "Online parameter estimation and adaptive control of permanent-magnet synchronous machines," *IEEE Trans. Ind. Electron.*, vol. 57, no. 7, pp. 2435–2443, July 2010.

[52] T. Boileau, N. Leboeuf, B. Nahid-Mobarakeh, and F. Meibody-Tabar, "Online identification of pmsm parameters: Parameter identifiability and estimator comparative study," *IEEE Trans. Ind. Appl.*, vol. 47, no. 4, pp. 1944–1957, July 2011.

[53] M. Hamida, J. De Leon, A. Glumineau, and R. Boisliveau, "An adaptive interconnected observer for sensorless control of pm synchronous motors with online parameter identification," *IEEE Trans. Ind. Electron.*, vol. 60, no. 2, pp. 739–748, Feb 2013.

[54] T. Vyncke, R. Boel, and J. Melkebeek, "On extended kalman filters with augmented state vectors for the stator flux estimation in spmsms," in *Applied Power Electronics Conference and Exposition (APEC), 2010 Twenty-Fifth Annual IEEE*, Feb 2010, pp. 1711–1718.

[55] A. Piippo, M. Hinkkanen, and J. Luomi, "Adaptation of motor parameters in sensorless pmsm drives," *Industry Applications, IEEE Transactions on*, vol. 45, no. 1, pp. 203–212, Jan 2009.

[56] M. Rashed, P. F. a. MacConnell, a. F. Stronach, and P. Acarnley, "Sensorless indirect-rotor-field-orientation speed control of a permanent-magnet synchronous motor with stator-resistance estimation," *IEEE Trans. Ind. Electron.*, vol. 54, no. 3, pp. 1664–1675, 2007.

[57] H. W. de Kock, M. J. Kamper, and R. M. Kennel, "Anisotropy comparison of reluctance and pm synchronous machines for position sensorless control using hf carrier injection," *IEEE Trans. Power Electron.*, vol. 24, no. 8, pp. 1905–1913, 2009.

[58] F. Briz, M. W. Degner, A. Diez, and R. D. Lorenz, "Measuring, modeling, and decoupling of saturation-induced saliencies in carrier-signal injection-based sensorless ac drives," *IEEE Trans. Ind. Appl.*, vol. 37, no. 5, pp. 1356–1364, 2001.

[59] Z. Chen, J. Gao, F. Wang, Z. Ma, Z. Zhang, and R. Kennel, "Sensorless control for spmsm with concentrated windings using multi-signal injection method," *IEEE Trans. Ind. Electron.*, vol. 61, no. 12, pp. 6624–6634, 2014.

[60] N. Teske, G. M. Asher, M. Sumner, and K. J. Bradley, "Encoderless position estimation for symmetric cage induction machines under loaded conditions," *IEEE Trans. Ind. Appl.*, vol. 37, no. 6, pp. 1793–1800, 2001.

[61] Y. Chen-Yen, J. Tamura, D. D. Reigosa, and R. D. Lorenz, "Position self-sensing evaluation of a fi-ipmsm based on high-frequency signal injection methods," *IEEE Trans. Ind. Appl.*, vol. 49, no. 2, pp. 880–888, 2013.

[62] T. Szalai, G. Berger, and J. Petzoldt, "Stabilizing sensorless control down to zero speed by using the high-frequency current amplitude," *IEEE Trans. Power Electron.*, vol. 29, no. 7, pp. 3646–3656, July 2014.

[63] R. Qu and T. Lipo, "Analysis and modeling of air-gap and zigzag leakage fluxes in a surface-mounted permanent-magnet machine," *IEEE Trans. Ind. Appl.*, vol. 40, no. 1, pp. 121–127, 2004.

[64] J. Ji-Hoon, H. Jung-Ik, M. Ohto, K. Ide, and S. Seung-Ki, "Analysis of permanent-magnet machine for sensorless control based on high-frequency signal injection," *IEEE Trans. Ind. Appl.*, vol. 40, no. 6, pp. 1595–1604, 2004.

[65] R. Ni, G. Wang, X. Gui, and D. Xu, "Investigation of d - and q -axis inductances influenced by slot-pole combinations based on axial flux permanent-magnet machines," *IEEE Trans. Ind. Electron.*, vol. 61, no. 9, pp. 4539–4551, Sept 2014.

[66] H. Jiangang, L. Jingbo, and X. Longya, "Eddy current effects on rotor position estimation and magnetic pole identification of pmsm at zero and low speeds," *IEEE Trans. Power Electron.*, vol. 23, no. 5, pp. 2565–2575, 2008.

[67] J. Persson, M. Markovic, and Y. Perriard, "A new standstill position detection technique for nonsalient permanent-magnet synchronous motors using the magnetic anisotropy method," *IEEE Trans. Magn.*, vol. 43, no. 2, pp. 554–560, 2007.

[68] D. D. Reigosa, F. Briz, M. W. Degner, P. Garcia, and J. M. Guerrero, "Temperature issues in saliency-tracking-based sensorless methods for pm synchronous machines," *IEEE Trans. Ind. Appl.*, vol. 47, no. 3, pp. 1352–1360, 2011.

[69] Y. Shih-Chin and R. D. Lorenz, "Analysis of iron and magnet losses in surface-permanent-magnet machines resulting from injection-based self-sensing position estimation," *IEEE Trans. Ind. Appl.*, vol. 48, no. 6, pp. 1901–1910, 2012.

[70] ——, "Surface permanent magnet synchronous machine position estimation at low speed using eddy-current-reflected asymmetric resistance," *IEEE Trans. Power Electron.*, vol. 27, no. 5, pp. 2595–2604, 2012.

[71] J. M. Guerrero, M. Leetmaa, F. Briz, A. Zamarron, and R. D. Lorenz, "Inverter nonlinearity effects in high-frequency signal-injection-based sensorless control methods," *IEEE Trans. Ind. Appl.*, vol. 41, no. 2, pp. 618–626, 2005.

[72] N. Teske, G. M. Asher, M. Sumner, and K. J. Bradley, "Analysis and suppression of high-frequency inverter modulation in sensorless position-controlled induction machine drives," *IEEE Trans. Ind. Appl.*, vol. 39, no. 1, pp. 10–18, 2003.

[73] R. Kennel, "Encoderless control of synchronous machines with permanent magnets - impact of magnetic design," in *Proc. OPTIM Conf.*, 2010, pp. 19–24.

[74] P. Landsmann, D. Paulus, and R. Kennel, "Online identification of load angle compensation for anisotropy based sensorless control," in *Proc. IEEE SLED Sympos.*, 2011, pp. 80–84.

[75] G. Wang, H. Zhan, G. Zhang, X. Gui, and D. Xu, "Adaptive compensation method of position estimation harmonic error for emf-based observer in sensorless ipmsm drives," *IEEE Trans. Power Electron.*, vol. 29, no. 6, pp. 3055–3064, June 2014.

[76] L. Ben-Brahim, "On the compensation of dead time and zero-current crossing for a pwm-inverter-controlled ac servo drive," *Industrial Electronics, IEEE Transactions on*, vol. 51, no. 5, pp. 1113–1118, Oct 2004.

[77] P. Mattavelli, L. Tubiana, and M. Zigliotto, "Torque-ripple reduction in PM synchronous motor drives using repetitive current control," *IEEE Trans. Power Electron.*, vol. 20, no. 6, pp. 1423–1431, 2005.

[78] D. Chen, J. Zhang, and Z. Qian, "Research on fast transient and 6n±1 harmonics suppressing repetitive control scheme for three-phase grid-connected inverters," *IET Power Electron.*, vol. 6, no. 3, pp. 601–610, 2013.

[79] B. Li, H. Lin, and H. Xing, "Adaptive adjustment of iterative learning control gain matrix in harsh noise environment," *Systems Engineering and Electronics, Journal of*, vol. 24, no. 1, pp. 128–134, Feb 2013.

[80] Z. Qiao, T. Shi, Y. Wang, Y. Yan, C. Xia, and X. He, "New sliding-mode observer for position sensorless control of permanent-magnet synchronous motor," *Industrial Electronics, IEEE Transactions on*, vol. 60, no. 2, pp. 710–719, Feb 2013.

[81] S. Bolognani, R. Oboe, and M. Zigliotto, "Sensorless full-digital pmsm drive with ekf estimation of speed and rotor position," *Industrial Electronics, IEEE Transactions on*, vol. 46, no. 1, pp. 184–191, Feb 1999.

[82] K. Liu, Z. Zhu, and D. Stone, "Parameter estimation for condition monitoring of pmsm stator winding and rotor permanent magnets," *Industrial Electronics, IEEE Transactions on*, vol. 60, no. 12, pp. 5902–5913, Dec 2013.

[83] Y. Zhang, Z. Yin, X. Sun, and Y. Zhong, "On-line identification methods of parameters for permanent magnet synchronous motors based on cascade mras," in *Power Electronics and ECCE Asia (ICPE-ECCE Asia), 2015 9th International Conference on*, June 2015, pp. 345–350.

[84] K. Liu, Q. Zhang, J. Chen, Z. Zhu, and J. Zhang, "Online multiparameter estimation of nonsalient-pole pm synchronous machines with temperature variation tracking," *Industrial Electronics, IEEE Transactions on*, vol. 58, no. 5, pp. 1776–1788, May 2011.

[85] K. Liu, Z. Zhu, and D. Stone, "Parameter estimation for condition monitoring of pmsm stator winding and rotor permanent magnets," *Industrial Electronics, IEEE Transactions on*, vol. 60, no. 12, pp. 5902–5913, Dec 2013.

[86] S. Underwood and I. Husain, "Online parameter estimation and adaptive control of permanent-magnet synchronous machines," *Industrial Electronics, IEEE Transactions on*, vol. 57, no. 7, pp. 2435–2443, July 2010.

[87] Q. An and L. Sun, "On-line parameter identification for vector controlled pmsm drives using adaptive algorithm," in *Vehicle Power and Propulsion Conference, 2008. VPPC '08. IEEE*, Sept 2008, pp. 1–6.

[88] J. Xu, F. Wang, S. Xie, J. Xu, and J. Feng, "A new control method for permanent magnet synchronous machines with observer," in *Power Electronics Specialists Conference, 2004. PESC 04. 2004 IEEE 35th Annual*, vol. 2, June 2004, pp. 1404–1408 Vol.2.

[89] G. Wang, H. Zhan, G. Zhang, X. Gui, and D. Xu, "Adaptive compensation method of position estimation harmonic error for emf-based observer in sensorless ipmsm drives," *Power Electronics, IEEE Transactions on*, vol. 29, no. 6, pp. 3055–3064, June 2014.

[90] Y. Park and S.-K. Sul, "A novel method utilizing trapezoidal voltage to compensate for inverter nonlinearity," *Power Electronics, IEEE Transactions on*, vol. 27, no. 12, pp. 4837–4846, Dec 2012.

[91] R. Hejny and R. Lorenz, "Evaluating the practical low-speed limits for back-emf tracking-based sensorless speed control using drive stiffness as a key metric," *Industry Applications, IEEE Transactions on*, vol. 47, no. 3, pp. 1337–1343, May 2011.

[92] K. Liu, Z. Zhu, Q. Zhang, and J. Zhang, "Influence of nonideal voltage measurement on parameter estimation in permanent-magnet synchronous machines," *Industrial Electronics, IEEE Transactions on*, vol. 59, no. 6, pp. 2438–2447, June 2012.